

Morphology of and Solvent Diffusion in Hollow Nanoparticle Systems



Zhihong CHEN

Supervised by Prof. Goran Ungar

Dr. Xiangbing Zeng

**A thesis submitted for the degree of Doctor of Philosophy in Department of
Materials Science and Engineering, the University of Sheffield**

December 2013

Summary

In this project, we studied the morphology of SiO₂/TiO₂ hollow nanoparticles (HNPs), the morphology of polymer-embedded HNPs and diffusion of solvents into polymer-embedded HNPs, mainly based on small angle scattering methods.

The average outer diameter, average inner diameter and polydispersity of HNPs were characterized by a combination of experimental methods, including light, X-ray and neutron scattering, electron microscopy and N₂ adsorption-desorption isotherms. Furthermore, the porosity of the shells of HNPs and the size of intrawall pores were determined by a new method proposed with the combination of the above techniques.

Three kinds of polymer-embedded HNP systems were prepared by freeze drying technique, i.e. poly(ethylene oxide) (PEO)-embedded HNPs, poly(methyl methacrylate) (PMMA)-embedded HNPs and polyethylene (PE)-embedded HNPs. The morphology of polymer-embedded HNP systems was investigated by SAXS and electron microscopy. A multi-shell sphere model was proposed to analyze the experimental SAXS data. For PEO-embedded HNPs, HNPs were observed to be supported on porous PEO scaffold. Moreover, it was found that nearly 96% of HNPs were buried uniformly in the PEO matrix, with a thin porous PEO layer deposited on the inner surface of HNP. However, the analysis for the morphology of PMMA-embedded HNPs and PE-embedded HNPs with current SAXS model was hindered due to the aggregation of HNPs.

Diffusion of solvents into polymer-embedded HNP systems was monitored by *in-situ* SAXS. Complex SAXS models were further proposed to obtain the diffusion kinetics. Diffusion of liquid low molecular PEO in PEO-embedded HNPs was found to consist of three stages, i.e. induction stage, steady state stage and depletion stage. It was further found that the filling rate of HNPs by solvent in the steady state stage was about 3 times faster than that in the induction stage and about 90 times faster than that in the depletion stage. Diffusion of water in PMMA-embedded HNPs and diffusion of oleyl alcohol and tetrafluorobenzene in PE-embedded HNPs were found to consist of a fast process and a slow process, which correspond to the relatively fast wetting of the polymer surface and the slow diffusion of solvents in the polymer matrix, respectively.

Acknowledgements

I am most grateful to Prof. Goran Ungar and Dr. Xiangbing Zeng for giving me the chance to carry out this challenging research work with financial support in their research group. Their passion for science, their strict attitude toward science, their efficient way to solve scientific problems, and their careful guidance for me has led me to the door of science. What I learnt and experienced in their group will surely help me to achieve more in my future adventure in the field of science. I am also much grateful for the help from previous and current members of our group, especially Prof. Feng Liu and Dr. Xiaobing Mang.

My special thanks go to Prof. Jyongsik Jang and the members of his group in Seoul National University. I obtained strong support from them. I would like to specially thank Miss Sun Hye Hwang for her contribution for the collaboration project. Without her hard work, it would be impossible for me to finish the project in time.

I also would like to thank Diamond Light Source (U.K.) and ISIS Rutherford Laboratory (U.K.) for providing the beamtime at different beamlines in the last three years.

My thanks also go to the Department of Materials Science and Engineering, University of Sheffield for the financial support of this work. I also thank staff and friends I met here for their help. I am much grateful for the advice on my Ph.D. study from my internal assessors, Prof. Derek C Sinclair and Dr. Günter Möbus. I also want to thank Mrs. Karen Burton and Mrs. Ann Newbould in the general office for their help during my application for a Ph.D. position and my Ph.D. study, respectively.

I would like to thank China Scholarship Council (CSC) for their financial support in the last three years.

Finally, I would like to thank my parents and members of my family for their support and understanding during my PhD study. I also want to give my special thanks to my dear girl friend, Changwei Cai, for her understanding and encouragement during my PhD study.

Contents

Abbreviations.....	i
CHAPTER 1 Introduction	1
1.1 Project Objective and Thesis Outline	1
1.2 Synthesis and Application of Hollow Nanoparticles.....	2
1.2.1 Synthesis of Hollow Nanoparticles	2
1.2.1.1 The Nanoscale-Kirkendall Effect Method.....	2
1.2.1.2 Galvanic Replacement Method	4
1.2.1.3 Inside-Out Ostwald Ripening Method.....	5
1.2.2 Application of Hollow Nanoparticles.....	6
1.2.2.1 Biomedical Application.....	6
1.2.2.2 Catalysts and Sensors	8
1.2.2.3 Rechargeable Batteries	9
1.3 Small Angle Scattering Applied to Nanoparticle Systems.....	10
1.3.1 Theoretical Framework	10
1.3.1.1 Decoupling Approximation.....	11
1.3.1.2 Local Monodisperse Approximation.....	12
1.3.1.3 Size – Spacing Correlation Approximation.....	13
1.3.2 Form Factor	13
1.3.2.1 Form Factor Models	13
1.3.2.2 Size Distribution of Nanoparticles	16
1.3.3 Structure Factor	17
1.3.3.1 Hard Sphere Interaction with Simple Pair Correlation Function	17
1.3.3.2 Hard Sphere Interaction within Percus-Yevick Approximation.....	18
1.3.3.3 Sticky Hard Sphere Interaction within Percus-Yevick Approximation	19
CHAPTER 2 Experimental Methods and Analysis	21
2.1 Sample Preparations	21
2.1.1 Hollow Nanoparticles	21

2.1.2 Polymer-Embedded Hollow Nanoparticles	21
2.2 Small Angle Scattering.....	22
2.2.1 Small Angle X-ray Scattering.....	23
2.2.1.1 Theoretical Basis of Small Angle X-ray Scattering	23
2.2.1.2 Experiments of Small Angle X-ray Scattering.....	27
2.2.2 Small Angle Neutron Scattering.....	29
2.2.2.1 Theoretical Basis of Small Angle Neutron Scattering.....	29
2.2.2.2 Experiments of Small Angle Neutron Scattering	29
2.2.3 Grazing Incidence Small Angle X-ray Scattering	30
2.2.3.1 Theoretical Basis of Grazing Incidence Small Angle X-ray Scattering.....	30
2.2.3.2 Experiments of Grazing Incidence Small Angle X-ray Scattering.....	31
2.3 Analysis Procedure for Small Angle Scattering Data	31
2.3.1 Reduction of Raw Data	31
2.3.2 Correction for Instrumental Broadening	32
2.3.3 The Fit Routine.....	33
2.4 Gas Adsorption Methods.....	34
2.5 Dynamic Light Scattering.....	37
CHAPTER 3 Size and Shell Porosity of Hollow Nanoparticles.....	39
Abstract.....	39
3.1 Introduction	40
3.2 Experimental Section.....	41
3.2.1 Materials	41
3.2.2 Methods	41
3.3 Theoretical Basis	42
3.3.1 SAXS and SANS.....	42
3.3.2 Gas Adsorption Methods.....	48
3.3.3 Dynamic Light Scattering.....	48
3.4 Results and Discussion	48
3.4.1 Size and Distribution of Hollow Nanoparticles.....	49

3.4.2 Shell Porosity and Size of Intrawall Pores	56
3.5 Conclusions	62
CHAPTER 4 Morphology of Polymer-Embedded Hollow Nanoparticles ..	64
Abstract.....	64
4.1 Introduction	65
4.2 Experimental Section.....	66
4.2.1 Materials	66
4.2.2 Methods	66
4.3 Theoretical Model for Small Angle X-ray Scattering	67
4.4 Results and Discussion	71
4.4.1 Sizes of Hollow Nanoparticles	71
4.4.2 Morphology of Poly(ethylene oxide)-Embedded Hollow Nanoparticles.....	75
4.5 Conclusions	82
CHAPTER 5 Diffusion of Solvent in Poly(ethylene oxide)-Embedded Hollow Nanoparticles.....	83
Abstract.....	83
5.1 Introduction	84
5.2 Experimental Section.....	85
5.2.1 Materials	85
5.2.2 Methods	85
5.3 Theoretical Model for Small Angle X-ray Scattering	86
5.4 Results and Discussion	87
5.4.1 Morphology of Poly(ethylene oxide)-Embedded Hollow Nanoparticles.....	88
5.4.2 Diffusion of Solvent in Poly(ethylene oxide)-Embedded Hollow Nanoparticles ...	90
5.4.3 Analysis of Diffusion Kinetics	99
5.5 Conclusions	102

CHAPTER 6 Diffusion of Solvents in Poly(methyl methacrylate)- and Polyethylene-embedded Hollow Nanoparticles	103
Abstract.....	103
6.1 Introduction	104
6.2 Experimental Section.....	104
6.2.1 Materials	104
6.2.2 Methods	105
6.3 Theoretical Model for Small Angle X-ray Scattering	106
6.4 Results and Discussion	106
6.4.1 Solvent Diffusion in Poly(methyl methacrylate)-Embedded Hollow Nanoparticles	106
6.4.1.1 Morphology of Poly(methyl methacrylate)-Embedded Hollow Nanoparticles	106
6.4.1.2 Diffusion of Water in Poly(methyl methacrylate)-Embedded Hollow Nanoparticles	109
6.4.2 Solvents Diffusion in Polyethylene-Embedded Hollow Nanoparticles.....	111
6.4.2.1 Morphology of Polyethylene-Embedded Hollow Nanoparticles	111
6.4.2.2 Diffusion of Water in Polyethylene-Embedded Hollow Nanoparticles	113
6.4.2.3 Diffusion of Oleyl Alcohol in Polyethylene-Embedded Hollow Nanoparticles	114
6.4.2.4 Diffusion of Tetrafluorobenzene in Polyethylene-Embedded Hollow Nanoparticles	116
6.5 Conclusions	117
Future Work	118
Publications and Conferences	119
Appendix	121
References	129

Abbreviations

Note, “specific” in all cases means “per unit weight of hollow nanoparticles”

A_{BET} : Specific surface area from BET method

A_{HNP} : Surface area of a hollow nanoparticle including all pores

A_{IWP} : Specific surface area of intrawall pores

A_{shell} : Specific surface area of the shell without any intrawall pores, i.e. internal and external surfaces

A_{total} : Total specific surface area of hollow nanoparticles

$A_{t\text{-plot}}$: Specific external surface area by t -plot method

α : Parameter of the direct correlation function in Percus-Yevick approximation

BET: Brunauer-Emmett-Teller method

BJH: Barrett-Joyner-Halenda method

ζ : Parameter of the direct correlation function in Percus-Yevick approximation

$C(q)$: Direct structure factor

$C(r)$: Direct pair correlation function

c : Constant in BET equation

DA: Decoupling approximation

DLS: Dynamic light scattering

D_{IWP} : Average diameter of the cylindrical intrawall pores

D_T : Translational diffusion coefficient

δ : Parameter in the direct correlation function in Percus-Yevick approximation

η : Volume fraction of the particles

η_S : Viscosity of the solvent

$F(q)$: Scattering amplitude associated with the form factor

$|F(q)|^2$: Form factor for single particle

$\langle |F(q)|^2 \rangle$: Form factor for polydisperse particles

GISAXS: Grazing incidence small angle X-ray scattering

$G(q, \tau)$: Time correlation function in dynamic light scattering

$g(q, \tau)$: Autocorrelation function in dynamic light scattering

γ : Surface tension of liquid nitrogen

Γ_i : Rate of correlation decay

HJ: Harkins-Jura equation

HNP: Hollow nanoparticle

$h(R)$: Size distribution function

$I(q)$: Scattering intensity of X-rays or neutrons

$I(q, t)$: Intensity of dynamic light scattering

k_B : Boltzmann constant

λ : Wavelength of X-rays or neutrons

N : Total number of experimental points in adsorption isotherm

n : n^{th} experimental points in adsorption isotherm

PY: Percus-Yevick approximation

p_0 : Saturation pressure of nitrogen

p : Actual pressure during experiments

q : Scattering vector

R_0 : Outer radius of hollow nanoparticle

R_g : Ideal gas constant

R_H : Hydrodynamic radius

r_0 : Inner radius of hollow nanoparticles

r_K : Radius of condensation in Kelvin equation

r_p : Radius of the pore

$r_{p,n}$: Pore radius in n^{th} step calculation

$\rho_{\text{SiO}_2/\text{TiO}_2}$: Density of the SiO_2 - TiO_2 mixture

$\rho(r)$: Electron density or scattering length density of a particle

$\Delta\rho$: Electron density (scattering length density) difference between the shell and the surrounding medium

SANS: Small angle neutron scattering

SAXS: Small angle X-ray scattering

$S(q)$: Structure factor

σ : Relative standard deviation of outer radius in particle size distribution

TEM: Transmission electron microscope

T : Temperature in Kelvin

t : Statistical average thickness of adsorbed layers

t_{shell} : Thickness of HNP shell

2θ : Scattering angle

V_0 : Molar volume of liquid nitrogen

V : Experimental adsorbed volume of nitrogen

V_{inner} : Specific volume of the inner cavities of HNPs

V_{IWP} : Specific surface area of intrawall pores

V_m : Volume of a unimolecular layer of nitrogen on all surfaces

$V_{\text{SiO}_2/\text{TiO}_2}$: Specific volume of amorphous $\text{TiO}_2/\text{SiO}_2$

V_{total} : Total specific volume of particles, including inner cavities, intrawall pores and shell material

$\Delta V_{p,n}$: Volume condensed in the pores at n^{th} step calculation for pore volume distribution

ΔV_n : Variation of measured volume at n^{th} step of the calculation of pore volume distribution

x : Porosity of the shell $x = V_{\text{IWP}} / (V_{\text{IWP}} + V_{\text{SiO}_2/\text{TiO}_2})$

z : Integer parameter in Schulz distribution function related to by $\sigma = 1 / \sqrt{z+1}$

CHAPTER 1 Introduction

1.1 Project Objective and Thesis Outline

Hollow nanoparticles (HNPs) have attracted wide attention in recent decades because of their application as drug delivery vehicles since they have high surface-to-volume ratio and large interior cavities. The porous structure of HNPs can greatly enhance the drug loading and release efficiency while decreasing degradation of drug during delivery and thus reducing the side effect to human body. The overall objective of this project is to develop a new *in-situ* method of monitoring material flow in and out of the HNPs and thus help understand the diffusion kinetics of solvent or drug molecules.

A number of experimental methods have been used in this project, including transmission and grazing incidence small angle X-ray scattering (SAXS and GISAXS), small angle neutron scattering (SANS), transmission electron microscopy (TEM), dynamic light scattering (DLS), and N₂ adsorption-desorption isotherms. In particular, SAXS was used as the real-time method to monitor the diffusion of solvent into HNPs. The principles of the experimental methods and the setup specially designed for this project are presented in Chapter 2.

Chapter 3 describes characterization for the morphology of SiO₂/TiO₂ HNPs, since the morphology has been reported to have a significant effect on the toxicity and delivery efficiency of HNPs. We also proposed a new method for determining the porosity of HNPs and the size of intrawall pores.

In Chapter 4, we report the SAXS characterization of poly(ethylene oxide) (PEO)-embedded HNP, a model system which enabled us to distinguish the timescale for the diffusion of solvent to the HNPs and into the inner cavities of HNPs, respectively. SAXS models were proposed to determine the complex structure of polymer-embedded HNPs.

The first experiment for determination of diffusion of solvent into HNPs is presented in Chapter 5. The diffusion of low molecular PEO into PEO-embedded HNPs was monitored by *in-situ* SAXS. Experimental SAXS data are presented and analyzed by newly proposed SAXS

models. The diffusion kinetics of low molecular PEO was discussed based on the reduced results from SAXS data.

Further, we carried out more investigation on diffusion kinetics of solvent in polymer-embedded HNPs in Chapter 6. Several cases were investigated in Chapter 6, including the diffusion of water into poly(methyl methacrylate)-embedded HNPs and diffusion of water, oleyl alcohol and tetrafluorobenzene in polyethylene-embedded HNPs, respectively.

1.2 Synthesis and Application of Hollow Nanoparticles

1.2.1 Synthesis of Hollow Nanoparticles

A number of reviews have focused on classifying the synthesis methods of HNPs. Lou and co-workers classified the synthesis methods into four groups according to the type of core template used during the synthesis, i.e. hard template method, soft template method, sacrificial template method and template free method.^[1] An and Hyeon categorized the synthesis methods into four themes according to the formation mechanism of HNPs, i.e. the nanoscale-Kirkendall effect method, chemical etching method, galvanic replacement method, and template-mediated method.^[2] Very recently, Fu and co-workers classified the synthesis methods of HNPs into four themes according to the precursors and building blocks used, i.e. core-shell precursor method, self-assembly of copolymers, self-assembly of polymer conjugates, and self-assembly of dendrimers.^[3] In this section, we describe three widely used synthesis methods for HNPs: the nanoscale-Kirkendall effect method, galvanic replacement method and the inside-out Ostwald ripening method.

1.2.1.1 The Nanoscale-Kirkendall Effect Method

The Kirkendall phenomenon was first found in metal, and it refers to the difference in the diffusion speed of two components in a metal diffusion couple.^[4] In the original Kirkendall phenomenon, vacancies were observed in the component which had faster diffusion speed.

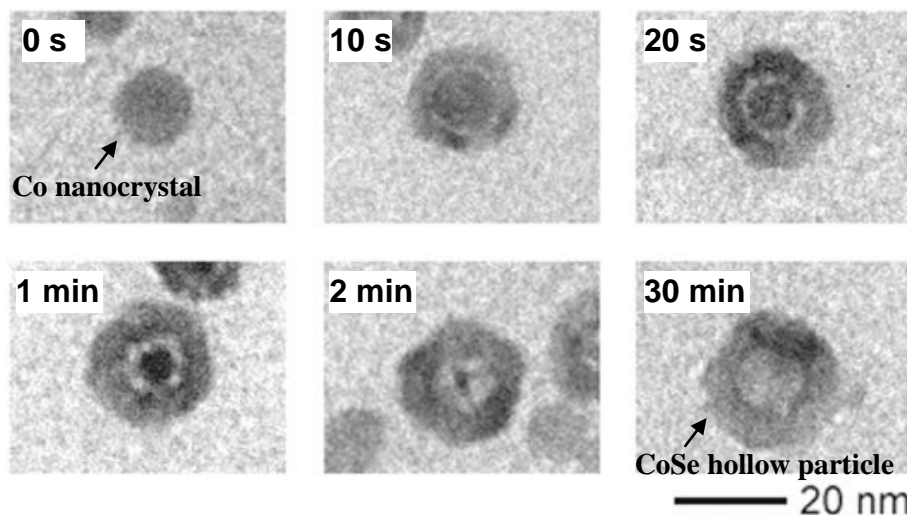


Figure 1.1 Synthesis of HNPs by nanoscale-Kirkendall effect method with formation of CoSe HNPs as an example.^[5]

The nanoscale-Kirkendall effect was first used to synthesize the CoSe HNPs by Yin and co-workers.^[5] The formation of HNPs reported by Yin and co-workers is presented in Figure 1.1. The mechanism of nanoscale-Kirkendall effect for HNP formation was also proposed by them and can be divided into four steps. Firstly, the cobalt nanoparticles were used as the template and reacted with the surrounding materials, e.g. sulphur, oxygen or selenium. Secondly, a thin layer of reaction product formed on the outer surface of original cobalt nanoparticle, and further reaction of cobalt with the surrounding materials was controlled by the outward diffusion of cobalt and inward diffusion of the surrounding material. Thirdly, vacancies were generated in the cobalt nanoparticle as a result of faster diffusion rate of cobalt compared to that of surrounding materials. Finally, the inner cavity formed due to the aggregation and collapse of vacancies. A hollow structure was finally formed with a central cavity surrounded by the reaction product in the shell.

After the first work of synthesizing HNPs by the nanoscale-Kirkendall effect method, much work has been done to synthesize different type of HNPs by this method. The method was also successfully applied to the synthesis of Fe_3O_4 HNPs by Peng and Sun.^[6] Cabot and co-workers reported the synthesis of a series of monodisperse iron oxide HNPs.^[7] Cabot also obtained asymmetric CdS hollow structures by the same method.^[8] Liang and co-workers fabricated $\text{CeO}_2\text{-ZrO}_2$ nanocages in a glycol medium.^[9] Shevchenko and co-workers fabricated iron oxide HNPs with small gold nanoparticle encapsulated within them.^[10]

Even though the nanoscale-Kirkendall effect method has been widely used to prepare HNPs, the physical mechanism on the details of mutual diffusion are not yet clear. Taking the synthesis of CoSe HNPs by Yin and co-workers^[5] as an example, since the cavity was first formed at the core-to-shell interface, it is difficult to explain how the cobalt atoms “jump” through the cavity to carry out further reaction.

1.2.1.2 Galvanic Replacement Method

The galvanic replacement method has been employed as an efficient way to prepare metal HNPs of sizes ranging from 10 nm to 1000 nm. The principle of this method can be explained as follows. Firstly, nanoparticles of a metal with low reduction potential are selected as the core templates, while the ion of another metal with high reduction potential is used as the surrounding material. In this step, appropriate core templates should be selected for the galvanic reaction according to the reduction potential of the metal ion. For example, the standard reduction potentials of AgCl/Ag, PdCl₄²⁻/Pd, PtCl₄²⁻/Pt and AuCl₄⁻/Au are 0.22 V, 0.59 V, 0.76 V and 0.99 V, respectively.^[2] When the metal nanoparticles are in contact with the ion, the galvanic reaction occurs due to the difference in the reduction potential between the two metal elements. In the galvanic reaction, the ions of the metal with higher reduction potential will receive electrons from the metal nanoparticles with lower reduction potential, resulting in precipitation of the reduced metal on the surface of the core template. Finally, as the reaction carries on, the core part will be dissolved totally and become a cavity, while the reduced metal forms the shell. An illustration of the galvanic reaction is shown in Figure 1.2 by taking the reduction of gold as an example.



with

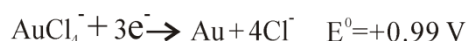


Figure 1.2 Illustration of the reaction mechanism of galvanic replacement method for preparing HNPs by taking the synthesis of Au HNPs as an example.

Xia's group succeeded in preparing Au, Pt and Pd HNPs by using Ag nanocrystals as the template in the galvanic replacement reaction.^[11] In the reaction of Au salt and Ag template, they found that during the reaction the electrons moved from the inside Ag core to the outside Au shell which resulted in the reduction of Au from its ion.^[12] Cobalt nanocrystals were also used as the core templates by Liang and co-workers to synthesis Pt,^[13] Au,^[14] and bimetallic AuPt^[15] HNPs.

The advantage of the galvanic replacement method is that it is simple to carry out. However, this method is costly since it usually uses rare metal nanoparticle as the sacrificial template.

1.2.1.3 Inside-Out Ostwald Ripening Method

The Ostwald ripening method is a spontaneous process which was first proposed by Ostwald in 1897 to describe the growth of large precipitates with the depletion of small precipitates.^[16] Recently, an inside-out Ostwald ripening method was proposed to synthesize hollow nanostructure.^[1] Lou et al. proposed a mechanism for the inside-out Ostwald ripening method^[17] which is described as follows. Initially, hydrolysis occurs in the mixture of the precursor and the solvent, e.g. mixture of potassium stannate and ethanol-water solvent for preparation of SnO₂ HNPs^[17]. Precipitates also appear in the solution. Then, the precipitates aggregate and form a loosely packed solid sphere to lower down the surface energy. Next, the surface of the loosely packed solid sphere starts to crystallize, while the core has a tendency to dissolve. Finally, gradual dissolving of the core and the growth of the crystallized shell will enable the formation of HNPs.^[1] An illustration of the inside-out Ostwald ripening method for preparing HNPs is presented in Figure 1.3.

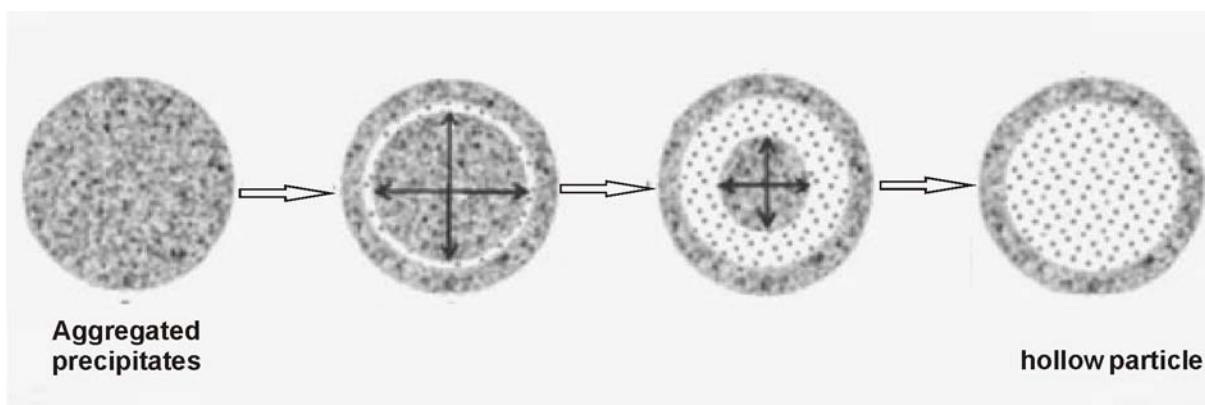


Figure 1.3 Illustration of the principle of inside-out Ostwald ripening method for synthesis of HNPs.^[1]

In the inside-out Ostwald ripening method, the polarity of the solvent and the concentration of the precursor are considered to be significant to control the size of HNPs.^[1] Lou et al. managed to synthesize SnO₂ HNPs via the inside-out Ostwald ripening method with ethanol-water mixture as the solvent and potassium stannate as the precursor.^[17] They finally obtained SnO₂ hollow nanoparticles of diameter ranging from 150 nm to 250 nm and shell thickness of around 30 nm. The inside-out Ostwald ripening method has also been employed to synthesize other HNPs, such as TiO₂ HNPs,^[18] Cu₂O HNPs,^[19] and Sn-doped TiO₂ HNPs.^[20] To investigate the mechanism, several time-dependent studies have been carried out to obtain evidence on the evolution of the reaction.^[21-23]

The advantage of the inside-out Ostwald ripening method is that it enables synthesis of HNPs in one pot or one step, without using any extra core templates. However, the details of the mechanism are still not very clear.

1.2.2 Application of Hollow Nanoparticles

1.2.2.1 Biomedical Application

Two intrinsic features of HNPs make them attractive in the field of biomedical application. Firstly, the large void space in the inner cavities of HNPs can be used to encapsulate various biomedical substances. Secondly, the surface of the HNPs can be functionalized for targeting

or bio-labeling. Therefore, HNPs are promising candidates in biomedical application such as drug delivery, specific targeting and imaging.

Silica HNPs have been popular drug delivery vehicles over the years, because they are biocompatible, chemically stable and easy for bio-conjugation.^[24-28] Li, Wen and co-workers prepared silica HNPs by using CaCO_3 as the core templates and tested the release rate of Brilliant Blue F which was used as a model drug.^[27] They showed that the release of Brilliant Blue F could last as long as 19 hrs, which was much longer than that of normal silica nanoparticles releasing all the model drugs within 10 mins. More work was done to increase the drug release time. Yang and co-workers fabricated silica HNPs by using Fe_3O_4 as templates.^[28] In their work, in order to control the release of drug, they modified the surface of silica HNPs with poly(ethylene glycol) (PEG). They found that the intra-shell pores in the surface modified HNPs were narrowed, i.e. the average diameter of the intra-shell pores decreased from 2.30 nm to 1.64 nm. To test the drug loading and release behaviour of the surface modified silica HNPs, doxorubicin (DOX), a chemotherapeutic drug, was selected as the model drug. In the case of PEG modified silica HNPs, only 20% of DOX was released in the first 30 hrs and 40% more was released in the next 14 days, while in the case of unmodified HNPs nearly 90% of DOX was released in the first 30 hrs.^[28] Yang and co-workers argued that the slow release rate of surface modified HNPs was due to the narrowed pores in the shell possibly by the deposition of PEG molecules.^[28] Piao et al.^[24] and Kim et al.^[25] also observed the sustainable release of DOX from silica HNPs by modifying the surface of nanoparticles and then covering them with PEG. Besides silica HNPs, the magnetic iron HNPs also have been used as drug delivery vehicles. These nanoparticles usually have high magnetic moment and can be used as contrast agency in magnetic resonance imaging (MRI).^[29] The shell of magnetic iron HNPs can collapse under alternating magnetic field, which enables the release of drugs.^[30]

In most of the drug delivery experiments, the drug is loaded into HNPs after the preparation of HNPs. Recently, Zhao et al. proposed a new drug loading method which loaded the drug during the preparation of HNPs.^[31] The main idea of their experiment was preloading DOX into the porous CaCO_3 core template. Then, silica was coated on the template as the shell. After that, the CaCO_3 template was removed by acid and a cavity was formed with only DOX

left inside. This new method is more efficient than conventional strategy since the synthesis process and drug loading process are finished in one step.

HNPs can also be used as bio-imaging materials. For example, gold nanocages can enhance the contrast in optical imaging and achieve the photothermal effect, due to high scattering and absorption to the light.^[32, 33]

1.2.2.2 Catalysts and Sensors

HNPs are promising catalysts for electrocatalytic and photocatalytic reactions. Compared with solid nanoparticles, HNPs have higher catalysis efficiency, because the porous structure of HNPs can increase the contact area during the reaction. An early attempt for the catalysis purpose was carried out by Kim and co-workers for the Suzuki coupling reactions, i.e. the reaction between aryl halides and arylboronic acids.^[34] They proposed that palladium HNPs had high catalytic activity, i.e. the yield of the reaction kept at 96% after 7 cycles of reaction. They also found that there was no leaching of Pd after the reaction, which is important for the reaction to produce pharmaceutical products. Similar study was carried out by Li, Zhou and co-workers.^[35] They used PdCo bimetallic HNPs to catalyze Sonogashira reaction, i.e. the reaction used to synthesize aryl alkynes by the coupling of terminal alkynes and aryl halides. The yield of the reaction catalyzed by PdCo HNPs reached 80% - 90%. Bai et al. prepared Pd-Rh HNPs via the galvanic replacement method by using copper as the core templates.^[36] They found that the Pd-Rh HNPs had much higher electrocatalytic activity for the oxidation of formic acid compared to Pd solid nanoparticle. Li, Bian and co-workers investigated the photocatalysis activity of TiO₂ HNPs for the degradation of phenol.^[18] They found that the catalytic activity of HNPs was much higher than that of solid nanoparticles. However, even though the use of HNPs can give high yield of the reaction, increasing the cycle times while keeping high catalytic property is still a challenge.

Owing to the porous structure and high surface area of HNPs, they are also promising candidates as efficient gas sensors with high sensitivity, quick response, rapid recovery, and selective detection. Usually, gas sensors with HNPs work based on the change of conductance during the absorption of gas molecules to the surface of sensor.^[1] At present, metal oxide HNPs are mainly used in the application of HNPs as gas sensors, such as SnO₂, In₂O₃ and

Fe_2O_3 .^[37-41] Kim, Choi and co-workers fabricated NiO functionalized SnO_2 HNPs by using Ni nanoparticles as the core templates.^[42] In their work, the gas sensor was prepared by screen printing the SnO_2 HNPs on aluminium substrate which was connected by two Au electrodes. The prepared sensor was placed in a quartz tube in a furnace with heat treatment at 450 °C. The ethanol vapour was given by a flow through method and the concentration of ethanol vapour was controlled by the mixing ratio of ethanol and dry air. Based on the resistance change of the sensor, the sensing properties of the sensor to ethanol vapour were investigated. The ethanol sensing properties of the sensor based on NiO –functionalized SnO_2 HNPs exhibited rapid response and recovery properties, i.e. with responding time of around 2 s and recovering time of around 4 s, which was much quicker than both SnO_2 powder giving response time of 8 s and recovery time of more than 100 s and NiO-doped SnO_2 powder giving responding time of 6 s and recovery time of around 20 s. They attributed the fast responding and recovery properties of the NiO functionalized SnO_2 HNP sensor to the rapid diffusion of gas through the porous shell and the improvement of the surface reaction by NiO. The sensing properties of Rh-loaded In_2O_3 HNP sensor was investigated by Kim and Hwang et al..^[41] They concluded that the Rh-loaded In_2O_3 HNPs had much shorter responding time than that of pure In_2O_3 HNPs.

1.2.2.3 Rechargeable Batteries

HNPs have been proposed as promising candidates for electrode materials of next generation lithium ion batteries. Application of HNPs as electrode materials can offer low capacity loss in the first charge-discharge cycle and keep high capacity in the later cycles. The porous structure of HNPs is considered to be the key reason for improving the performance of the lithium battery, since the inner cavity can largely increase the storage of lithium ions. Also, the robust structure of HNPs can avoid the breakdown of the electrode material during lithium ion insertion-deinsertion cycles.

Lou et al. prepared and tested the electrochemical activity of SnO_2 HNPs when used as anode material.^[17] They made a working electrode consisting of 80 wt% of SnO_2 HNPs, 10 wt% of carbon black as the conductivity agent, and 10 wt% of poly(vinylidene fluoride) as the binder. They used LiPF_6 in a mixture of ethylene carbonate and diethyl carbonate as the electrolyte.

The lithium ion cell prepared with SnO₂ HNPs exhibited an initial discharge capacity of 1140 mA h g⁻¹, a value much higher than that of pristine SnO₂ nanoparticles of 645 mA h g⁻¹. Moreover, the cyclic performance of the lithium battery prepared with SnO₂ HNPs was largely improved. To improve the cycling performance of the lithium battery, the same group led by Lou synthesized SnO₂-carbon double shell HNPs and tested the activity of the anode made from the above double shell HNPs.^[43] Their results showed that the capacity loss of the lithium battery was very low even after 75 charge-discharge cycles. The improved performance of the lithium battery was thought to be attributed to the improved stability of the SnO₂ HNPs by carbon since the carbon layer could act as a buffer layer to decrease the volume change of HNPs during lithium ion insertion and deinsertion. The performance activity of the lithium batteries made by other HNPs was also studied, such as Si HNPs,^[44] Sb HNPs^[45] and α-MnO₂ HNPs^[46]. However, obtaining lithium batteries with high capacity, low capacity loss and stable cycle performance is still a challenge.

1.3 Small Angle Scattering Applied to Nanoparticle Systems

Since the sizes of nanoparticles are generally within the range from 10 nm to 1000 nm, small angle scattering is an appropriate technique to probe the structure of nanoparticles. In the first part of this section, theories which have been used to simplify the calculation of scattering intensity from nanoparticles are introduced. Then, form factor models which are related to the shape, size and size distribution of nanoparticles are discussed. Finally, structure factor models which are related to the arrangement of nanoparticles in space are reviewed.

1.3.1 Theoretical Framework

The scattering intensity can be defined as the number of photons scattered into a unit solid angle in a given direction per second.^[47] As the numerical calculation of the intensity can be very complicated,^[48-50] this section discusses the ways to approximate the intensity for quick calculation and practical application, i.e. simplifying the relationship between form factor and structure factor. From literatures, there are mainly three kinds of theory frameworks to

calculate the scattering intensity for practical application, namely the decoupling approximation, the local monodisperse approximation and the size-spacing correlation approximation.

1.3.1.1 Decoupling Approximation

Decoupling approximation (DA) was first introduced by Kotlarchyk and Chen in 1983.^[51] In this approximation, it is assumed that there is no correlation between the size and the arrangement of particles. In DA, the scattering intensity can be written as

$$I(q) = N_{\rho} [\langle |F(q)|^2 \rangle + \langle F(q) \rangle^2 (S(q) - 1)] \quad (1.1)$$

where N_{ρ} is the number density of the particles in the sample, $F(q)$ is the scattering amplitude of a single particle, $S(q)$ is the structure factor, and $q = 4\pi \sin\theta / \lambda$ is the scattering vector with 2θ the scattering angle and λ the wavelength of the incident beam. In the above equation, the triangular bracket $\langle \dots \rangle$ denotes the average over the size distribution of particle. $\langle |F(q)|^2 \rangle$ is called form factor which is related to the Fourier transform of the electron density distribution (for X-ray scattering) or scattering length density (for neutron scattering) within the nanoparticle. The structure factor $S(q)$ is the Fourier transform of the arrangement of particles in space.

The advantage of DA is that it is possible to calculate the scattering intensity by calculating the form factor and the structure factor separately. However, it can be seen from equation 1.1 that the size distribution of particles is only taken into account in the form factor. Therefore, the drawback of DA is that the effect of size distribution of particles on the structure factor is neglected. In a study by Pedersen,^[52] the theoretical scattering intensity of hard spheres with polydispersity ranging from 4% to 42% was calculated within DA. The calculated scattering intensity was then compared with those by other simulation methods. It was found by Pedersen that when the polydispersity of nanoparticle reached 10%, DA started to give unreasonable results in the scattering intensity in the low q range. Revenant et al. used the DA to analyze the grazing incidence small angle X-ray scattering pattern of Pd nanoparticles on MgO(001) single crystal.^[53] They found that DA failed to describe the diffuse scattering observed by experiments. They attributed the failure of DA to the strong correlation between

the size and the position of Pd nanoparticles on the substrate. Therefore, extra care should be taken when applying DA to nanoparticle systems with large polydispersity in size.

1.3.1.2 Local Monodisperse Approximation

As has been mentioned above, DA is not suitable for particle system with large polydispersity. Therefore, a new approximation named local monodisperse approximation (LMA) was introduced by Pedersen to solve this problem.^[52]

In LMA, the size and position of the particles are correlated. The particle system is considered to consist of many monodisperse subsystems with different sizes and the particles from the same subsystem are assumed to locate in the same region of the sample. The total scattering intensity is then calculated by summing up the scattering intensity from each subsystem weighted by its frequency in the size distribution of particles. The scattering intensity in LMA can be written as

$$I(q) = \Delta\rho^2 \int_0^{\infty} F^2(q) \cdot S(q) \cdot h(R) dR \quad (1.2)$$

where $\Delta\rho$ is the difference in the electron density or scattering length between the particle and the surrounding media, $F^2(q)$ is the form factor of a monodisperse subsystem, $S(q)$ is the structure factor of the same subsystem and $h(R)$ is the particle size distribution function.

The advantage of LMA is that it takes into account the effect of size distribution on the structure factor, which may be more appropriate to some real systems compared to DA. It has been reported that reasonable results were obtained by LMA for a system with polydispersity of nanoparticles up to 0.4.^[52] LMA has been successfully applied to analyze metallic precipitates in metal.^[54, 55] However, the application of LMA is restricted due to its assumption of the subsystem which may be not true in many real particle systems.

1.3.1.3 Size – Spacing Correlation Approximation

Size-spacing correlation approximation (SSCA) was first applied to grazing incidence small angle X-ray scattering by Leroy very recently.^[56] Within this approximation, the size-size correlation and the size-spacing correlation are considered using the paracrystal model in which the lattice only has short range order due to the distortion of the lattice. Size-size correlation means the size of the particle is linked to its neighbors. Size-spacing correlation refers to the dependence of the mean interparticle distance on the size of the particles. Usually, the paracrystal model is used in SSCA to describe the arrangement of nanoparticles with different sizes.

The SSCA model was successfully applied to the growth of metallic particles on inorganic film by building a one dimensional paracrystalline model.^[57, 58] However, the application of SSCA is limited since the calculation involving 2D or 3D paracrystal models could be very complicated.

1.3.2 Form Factor

1.3.2.1 Form Factor Models

Many reviews have been written to summarize the form factor functions of nanoparticles with basic geometries.^[59-62] Therefore, we are not going to repeat the content in those reviews. Instead, we focus on nanoparticles which are usually investigated but have more complex geometry, i.e. nanoparticles with a core-shell structure.

Generally, form factor is the product of the scattering amplitude and its conjugate. The scattering amplitude of a particle is the Fourier transform of the electron density distribution or scattering length density distribution within the particle and can be expressed by^[47]

$$F(\vec{q}) = \int_v \rho(\vec{r}) \exp(i\vec{q}\vec{r}) dv \quad (1.3)$$

where $\rho(\vec{r})$ is the electron density distribution or the scattering length density distribution within the particle, \vec{r} is a vector in space representing the distance and direction of a point in

the space to the centre of the nanoparticle. Note that the scattering amplitude is the integral over the volume of the sample. For an isotropic system consisting of spherical core-shell particles, the above scattering amplitude can be expanded from 3D to 1D and given by^[63]

$$F(q) = \int_0^{R_c} \Delta\rho_1 \frac{4\pi r^2 \sin(qr)}{qr} dr + \int_{R_c}^{R_s} \Delta\rho_2 \frac{4\pi r^2 \sin(qr)}{qr} dr \quad (1.4)$$

where R_C and R_S are the radius of the core and the outer radius of the shell, respectively, $\Delta\rho_1$ is the difference in the electron density or scattering length density between the core and the outside medium while $\Delta\rho_2$ is the difference in the electron density or scattering length density between the shell and the outside surrounding medium, respectively. Core-shell particles with other shapes such as disk^[64], cylinder^[65] and oriented spindle^[66] are out of the scope of this review.

(1) Core-shell sphere models with constant electron density in each region

A core-single shell sphere model with constant electron density both in the core and the shell has been widely used to determine the morphology of nanoparticles. Bryant and co-workers used a core-single shell sphere model to analyze the change of polymer spheres with the change of temperature and particle composition.^[67] Pedersen also used the core-single shell sphere model to study the scattering behaviour of block copolymer micelles.^[68] The same form factor model was employed by Kohlbrecher and co-workers to investigate the stability of silica nanoparticles coated with octadecane in toluene.^[69] The core-single shell sphere model was also used by Zeng and co-workers to study the self assembly behaviour of surfactant micelles in water.^[70] In Chapter 3 of this thesis, we derived the analytical expression for the form factor of a hollow single shell sphere model to investigate the shape, size and size distribution of SiO₂/TiO₂ HNPs.^[71] The morphological information of SiO₂/TiO₂ HNPs obtained by us agrees well with the results obtained by other methods, i.e. dynamic light scattering, transmission electron microscopy and nitrogen adsorption-desorption isotherms.

The core-multishell sphere models have also been studied. He and co-workers used a core-double shell sphere model to study the shape change of PMMA core-rubber middle layer-PMMA outer shell nanoparticle during deformation of the sample.^[72] Hayter derived the

expression for the scattering function of core-multishell spherical particle.^[73] The core-multishell model derived by Hayter was subsequently used by Nayeri and co-workers to investigate the theoretical scattering behaviour of core-multishell spheres with up to 10 layers of shells.^[74] In a review of Pedersen,^[60] the analytical expression of form factor for spherical concentric shells was given. Forster and co-workers derived the form factor of core-multishell spheres by making use of hypergeometric functions.^[75] In this thesis, based on Forster and co-workers' study, we proposed a hollow triple shell sphere model to extract the morphological information of SiO₂/TiO₂ HNPs embedded in polymer matrix, see Chapter 4.^[76] Our study successfully revealed that the original hollow single shell nanoparticles changed to hollow-triple shell nanoparticles with a thin layer of polymer covered both on the wall of the inner cavity and outer surface of the original nanoparticle.

The above studies are all focused on strictly centro-symmetric core-shell spheres with constant electron density in each region. Very recently, Li, Liu and co-workers proposed the form factor function for yolk-shell particles, a new type of core-shell nanoparticle emerged in recent years possessing a mobile core within the hosting shell.^[77] Their study is of interest since yolk-shell particle can be used as catalysts with high catalytic activity.

(2) Core-shell sphere models with variable electron density in each region

Interest has also been drawn to the core-shell particles with electron density following mathematical functions such as algebraic and exponential functions. In this kind of core-shell nanoparticles, the density profile varies from the centre to the outer surface of nanoparticles. This kind of density profile is common in polymer, e.g. star polymer, comb polymer, polymer with corona, and polymer grafted to other particles. Halperin used an exponential function to describe the electron density decay in the shell for a star-like diblock copolymer.^[78] Pedersen and co-workers calculated the form factor of core-shell block polymer nanoparticles with parabolic density profile.^[79, 80] Further, by using a form factor model in which the core and the shell both have parabolic density profile, Pedersen and co-workers succeeded in studying the temperature sensitive behaviour of a cross-linked polymer.^[81-84] Forster also studied the form factor of core-shell particle with different algebraic density profile in the core and the shell.^[75]

1.3.2.2 Size Distribution of Nanoparticles

For a polydisperse system with nanoparticles of different sizes, the size distribution of nanoparticles has to be taken into account when calculating the form factor function. The expression of form factor for polydisperse system can be written by

$$\langle |F(q)|^2 \rangle = \int_0^\infty |F(q)|^2 h(R) dR \quad (1.5)$$

where $\langle |F(q)|^2 \rangle$ is the averaged form factor of nanoparticles, $|F(q)|^2$ is the form factor of a single nanoparticle, and $h(R)$ is the size distribution function as already defined in equation 1.2.

The size distribution function is usually a probability function. Gaussian distribution function, Schulz distribution function^[85] and log-normal distribution function are three kinds of size distribution function commonly used. Among them, Gaussian distribution function can generally give acceptable approximation to most of nanoparticle systems since it is symmetric. As opposed to the Gaussian distribution function, Schulz distribution function is asymmetric and it skews to large sizes.^[85] The skewing feature of Schulz distribution enables its application in biomolecular, microemulsion or other systems that tend to aggregate. Calculations of scattering intensity involving Schulz distribution appeared several decades ago.^[86, 87] Recently, Wagner succeeded in applying the Schulz size distribution function to fit the SAXS experimental data of cobalt ferrite/silica core-shell particles and polymer/iron oxide core-shell particles.^[88] Nayeri and co-workers used Schulz distribution function to describe the size distribution of core-single shell spheres and core-multi shell spheres.^[74] There are also calculations using log-normal distribution function,^[89, 90] but no further discussion is shown here since the only difference between the shape of log-normal and Schulz distribution function is that the former skews to small particle size while the latter skews to large particle size.

Even though the calculation over size distribution of nanoparticles can be done analytically or numerically, extra care has to be taken when calculating the scattering function of core-shell nanoparticles since the calculation may be time consuming. For core-shell nanoparticles, especially those with multiple shells, the calculation can be largely simplified if assuming the

size distribution of the inner core and that of the shell is coupled, i.e. the radii of the core and the shell are proportional in each nanoparticle.

1.3.3 Structure Factor

The structure factor $S(q)$ mainly deals with the interference among the X-ray or neutron beams scattered from different particles. In a dilute system, since the distance between two nanoparticles is much larger than their sizes, the interaction among nanoparticles is negligible and therefore the structure factor is negligible. However, for a concentrated nanoparticle system, the structure factor has to be taken into account.

1.3.3.1 Hard Sphere Interaction with Simple Pair Correlation Function

In a randomly disordered hard sphere system, the arrangement of particles is usually treated as isotropic and homogenous. The structure factor can be interpreted by pair correlation function which denotes the probability of finding another particle in the volume element at distance r from the given origin. The structure factor expressed through the pair correlation function can be written as^[91]

$$S(q) = 1 + \rho_N \int_0^{\infty} 4\pi r^2 \{g(r) - 1\} \frac{\sin qr}{qr} dr \quad (1.6)$$

where $S(q)$ is the structure factor, ρ_N represents the packing density of particles in space, and $g(r)$ is the pair correlation function. It should be noted that the above equation has been reduced to a 1-D integral for an isotropic system. From the above equation, it is obvious that the structure factor can be calculated when the pair correlation function is known.

In 1927, Debye reported a simple form of pair correlation function which can be expressed by^[92]

$$g(r) = \begin{cases} 0, & r \leq 2R \\ 1, & r > 2R \end{cases} \quad (1.7)$$

where r refers to the distance to the centre of the nanoparticle and R is the radius of nanoparticle. With the Debye pair correlation function, the structure factor can be easily calculated. However, it was pointed out by Fournet^[93] that the Debye hard sphere model is not suitable for the system with high concentration of nanoparticles, since the calculated structure factor gives large error.

Besides the Debye hard sphere model mentioned above, there are also other pair correlation functions, e.g. the Zhu pair correlation function^[94] and the Venables pair correlation function^[95]. However, these functions are not commonly used and hence they are not discussed here.

1.3.3.2 Hard Sphere Interaction within Percus-Yevick Approximation

The structure factor of hard spheres with weak interaction can be determined according to thermodynamics of hard spheres in liquid. The Percus-Yevick (PY) approximation for hard sphere interaction is an excellent method to calculate the structure factor.^[96] By solving the Ornstein-Zernike integral equation,^[97] which shows the relationship between the direct correlation between two neighbouring nanoparticles and the indirect correlation between all other nanoparticles, the PY approximation has been proven to be a successful approximation to calculate the structure factor.^[48, 98-100] The PY approximation has been used to investigate the structure factor in many systems such as spherical blocks in polymer^[101, 102], gas bubbles in liquid-like structures,^[103] colloidal hard spheres in aqueous solution,^[104] and inorganic nanoparticles in a polymer matrix.^[76]

The advantage of PY hard sphere model is that it is valid for very high packing density of nanoparticles. Additionally, the analytical expression of the structure factor for nanoparticles packing in 3D has been derived and is easy to calculate. However, it should be mentioned that it is not an easy task to calculate the structure factor based on PY approximation for nanoparticles packing in 2D, as there is no analytical expression for the 2D structure factor.^[105-107]

1.3.3.3 Sticky Hard Sphere Interaction within Percus-Yevick Approximation

When nanoparticles are attractive to each other in some cases, e.g. micelles, charged nanoparticles or polymer-coated inorganic nanoparticles, the attraction among nanoparticles has to be taken into account for the structure factor. The structure factor for sticky hard spheres was first proposed by Baxter in 1968 based on the Ornstein-Zernike equation and the Percus-Yevick closure approximation.^[108] The Baxter's sticky hard sphere potential, which was improved by the square well potential later,^[109, 110] consists of a hard core and a thin attractive layer on the particle surface. The sticky hard sphere potential can be defined by

$$U(r) = \begin{cases} +\infty, & 0 < r' < 2R \\ -U_0, & 2R < r' < (2R + \delta) \\ 0, & r' > 2R + \delta \end{cases} \quad (1.8)$$

where r' is the distance starting from one side of a particle toward the other particle, R is the radius of the hard core, and δ is the thickness of the attractive layer on the surface of particle. In the sticky hard sphere potential, a sticky parameter is used to characterize the degree of "adhesion" among the hard spheres.

The stickiness and the packing density of nanoparticles are two important parameters which can determine the state of nanoparticles in the system. It is possible to derive the value of stickiness and packing density by fitting the theoretical structure factor to the experimental structure factor. However, Baxter pointed out^[108] that two criteria should be considered when selecting the derived value for stickiness and packing density: reasonable thermodynamic state of the system and convergence of the integral for the indirect correlation function in Ornstein-Zernike equation. Baxter also derived the critical packing density and stickiness of hard spheres for phase transitions of nanoparticle system, e.g. from separated hard spheres to aggregated or networked nanoparticles. Similar calculations were also performed by Regnaut^[109] and Menon^[110].

The sticky hard sphere structure factor has been widely used to investigate the interaction among attractive nanoparticles. Dekruif et al. used the sticky hard sphere structure factor to investigate the change of stickiness of silica nanoparticles in benzene as a function of temperature and nanoparticle concentration.^[111] Duits et al. studied the temperature and concentration dependence of stickiness of octadecyl chain-coated silica nanoparticles in

benzene.^[112] They found that the stickiness of octadecyl-coated silica nanoparticles varied when the experimental condition changed. Wen et al. investigated the absorption behaviour of PEG on concentrated silica nanoparticles and the interaction among the polymer-coated silica nanoparticles by the sticky hard sphere structure factor.^[113] In a study by Wen and co-workers, the general hard sphere potential, the Hayter-Penfold-Yukawa potential and the sticky hard sphere potential were used to investigate both the attractive and repulsive behaviour of silica nanoparticles caused by the adsorbed polymer layer. They found that absorbing a small amount of PEG reduced the repulsion among nanoparticles, and a network consisting of polymer-coated silica nanoparticles and bridging polymer molecules was finally formed with the increase of the polymer concentration. Chinchalikar et al. investigated the aggregation and clustering behaviour of silica nanoparticles in electrolyte solution by stick hard sphere structure factor.^[114] They concluded that silica nanoparticles gradually aggregated with the increase of the concentration of electrolyte and permanent clusters was formed when the concentration of electrolyte was above the critical salt concentration. Very recently, Joksimovic et al. studied the stability of silica nanoparticle in polymer solutions.^[115] They reported the effect of polymers molecular weight and concentration on the aggregation of silica nanoparticles.

CHAPTER 2 Experimental Methods and Analysis

2.1 Sample Preparations

The preparation of samples, including hollow nanoparticles (HNPs) and polymer-embedded HNPs, was carried out by Sun Hye Hwang, Chanhoi Kim and Jongmin Roh in the group of Prof. Jyongsik Jang in Seoul National University. Here, only brief description of the sample preparation is presented.

2.1.1 Hollow Nanoparticles

To synthesize HNPs, colloidal solution with silica nanoparticles was first prepared according to the Stöber method.^[116] Then, 3.6 mL of titanium (IV) isopropoxide (TTIP), 18 mL of ethanol, and 6 mL of acetonitrile were added to the above colloidal solution with 0.5 g silica nanoparticles. The mixed solution reacted with the colloidal SiO₂ at 5 °C for 6 h. After the sol-gel reaction, the above-mentioned TTIP-added silica nanoparticles transformed into silica/titania core/shell nanoparticles. The HNPs were synthesized by sonication treatment of core/shell nanoparticles in ammonia solution (0.1 M) for 3 h. The final product of HNPs was then obtained by centrifugation at 5,000 rpm (Mega 17R, Hanil Science and Industrial). The mechanism of particles evolution from core/shell structure to hollow structures was reported elsewhere by our collaborators.^[117] The method of synthesis HNPs in this project belongs to the hard template method, since the silica nanoparticles were used as the core template.

2.1.2 Polymer-Embedded Hollow Nanoparticles

Three kinds of polymer-embedded HNPs were synthesized by freeze drying technique in this project, i.e. poly(ethylene oxide)-embedded HNPs (PEO-HNP), poly(methyl methacrylate)-embedded HNPs (PMMA-HNP), and polyethylene-embedded HNPs (PE-HNP), respectively.

The preparation method for the above three polymer-HNP systems was different due to the compatibility of the polymer and HNPs in solutions.

To prepare PEO-HNP samples, PEO with $M_w = 100,000$ was first dissolved in water to form a solution with concentration around 10 wt%. Next, HNPs were added to the solution with the concentration of about 5 wt%. The suspension was then placed in 1.5 mm X-ray capillaries. The capillaries were then frozen at liquid nitrogen temperature, followed by further drying process taking place over 12 hrs at -52.2 °C under vacuum (15.9 Pa). Freeze drying was carried out using an FD-1000 instrument (EYELA, Japan).

To prepare PMMA-HNP samples, PMMA with $M_w = 350,000$ was first dissolved in acetone to form a solution with concentration about 2 wt%. Next, the above solution was injected into 1.5 mm X-ray capillary and frozen in cold trap bath, followed by drying in vacuum oven. Then, solution of HNPs dispersed in ethanol (~2 wt%) was injected into the frozen-dried PMMA. Finally, the PMMA-HNP sample was obtained by further drying the injected HNP solution in vacuum oven.

To prepare PE-HNP samples, high density PE was first dissolved in para-xylene to form a solution with concentration about 2 wt%. Next, the above solution was injected into 1.5 mm X-ray capillary and frozen at -40 °C for 3 min in cold trap bath, followed by drying at -52.2 °C under vacuum (15.9 Pa) for over 12 hrs. Then, solution of HNPs dispersed in ethanol (~2 wt%) was injected into the frozen-dried PE. Finally, the PE-HNP sample was obtained by further drying the injected HNP solution in vacuum oven.

2.2 Small Angle Scattering

Small angle scattering techniques are mainly used to probe structures with size ranging from 10 to 1000 Angstrom. Small angle scattering have found their wide application in a variety of research fields, such as particulate systems, nonparticulate two-phase systems and periodic systems.^[47] Compared to other conventional structural characterization methods, small angle scattering is non-destructive and gives excellent statistics information. In this section, the theoretical and experimental aspects of small angle scattering is introduced, including small

angle X-ray and neutron scattering (SAXS and SANS) and grazing incidence small angle X-ray scattering (GISAXS).

2.2.1 Small Angle X-ray Scattering

2.2.1.1 Theoretical Basis of Small Angle X-ray Scattering

The introduction to the theoretical basics of small angle X-ray scattering (SAXS) starts with the scattering of X-ray by an electron, then goes to the scattering by a single nanoparticle, and finally leads to a system with a number of nanoparticles.

X-ray is a kind of electromagnetic radiation with its electric field oscillating perpendicular to the direction of propagation. When an electron is exposed to X-ray beam, caused by the oscillation of the electric field of the X-ray, the electron will oscillate and emit X-ray of the same wavelength as the incident beam to all directions of the space. The intensity of the scattered beam observed at an angle 2θ to the direction of the incident beam can be written as

$$I_e = I_0 \frac{e^4}{m^2 c^4 r^2} \cdot P \quad (2.1)$$

where I_0 is the intensity of the incident beam, e is the charge of the electron, m is the mass of the electron, c is the speed of light, r is the distance between the electron and the observing position, and P is the polarization factor. The polarization factor is given by

$$P = \begin{cases} \cos^2(2\theta), & \text{polarized beam} \\ \frac{1 + \cos^2(2\theta)}{2}, & \text{unpolarized beam} \end{cases} \quad (2.2)$$

where 2θ is the scattering angle. In small angle scattering, 2θ is usually small. Therefore, the polarization factor is very close to 1 for both polarized and unpolarized beam.

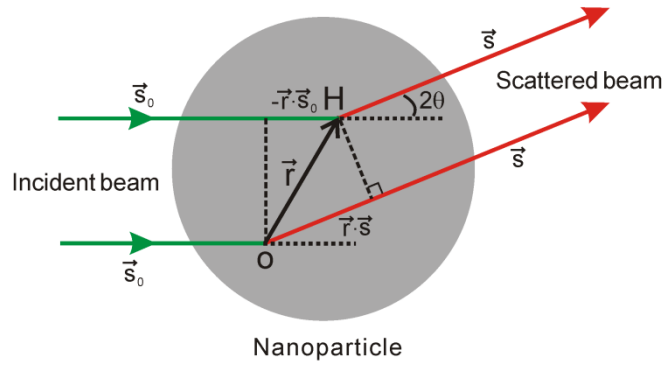


Figure 2.1 Illustration for the scattering of X-ray by electrons in a nanoparticle. O is the arbitrarily selected origin and H represents a volume element with volume δv and electron density $\rho(\vec{r})$. \vec{r} is the distance between O and H. \vec{s}_0 and \vec{s} are the unit vectors representing the incident beam and the scattered beam, respectively.

When considering the scattering of X-ray by a particle with assemblies of many electrons, as is shown in Figure 2.1, the phase difference of the scattered beam from various electrons should be taken into account. In the geometry of Figure 2.1, since the number of electrons in the volume element H is $\delta v \cdot \rho(\vec{r})$ with $\rho(\vec{r})$ the electron density at point H and δv the volume of point H, the amplitude of the scattered beam from H is

$$A_H = A_e \cdot \rho(\vec{r}) \cdot \delta v \quad (2.3)$$

where A_H is the amplitude of the scattered beam from volume element H, A_e is the amplitude of the scattered beam by a single electron. As can be seen from Figure 2.1, the path difference between the X-ray beam passing through O and H is

$$\text{path difference} = \vec{r} \cdot \vec{s} - \vec{r} \cdot \vec{s}_0 \quad (2.4)$$

and hence the phase difference between the scattered beam from O and that from H is

$$\text{phase difference} = \frac{2\pi}{\lambda} \vec{r} \cdot (\vec{s} - \vec{s}_0) \quad (2.5)$$

Now we define

$$\vec{q} = \frac{2\pi}{\lambda} (\vec{s} - \vec{s}_0) \quad (2.6)$$

with the module of $q = 4\pi \sin\theta / \lambda$.

When both the amplitude and phase of the scattered beam from volume element H is taken into account, the scattering amplitude of H is further given by

$$A_H = A_e \cdot \rho(\vec{r}) \cdot \delta v \cdot \exp(i\vec{q} \cdot \vec{r}) \quad (2.7)$$

Therefore, the total scattering amplitude of the particle can be derived by summing up the scattering from all electrons within the particle. The total scattering amplitude can be written by

$$F(\vec{q}) = A_e \cdot \int_v \rho(\vec{r}) \exp(i\vec{q} \cdot \vec{r}) \delta v \quad (2.8)$$

Since the amplitude of an electron A_e is a constant, it is usually treated as a scaling factor in the calculation for the scattering amplitude of the nanoparticle. The scattering intensity of a nanoparticle will be the multiplication of $F(\vec{q})$ and its complex conjugate. The expression of scattering amplitude $F(\vec{q})$ for a nanoparticles can be possibly expanded into simple formulae, e.g. for 3-D spherical nanoparticles.

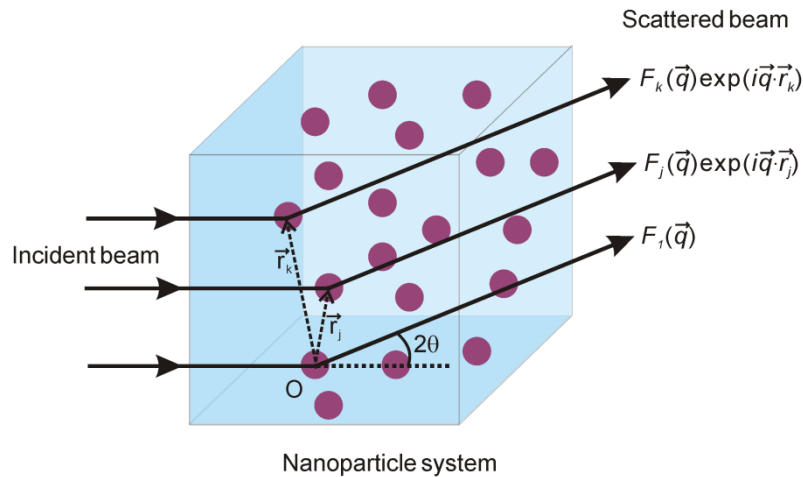


Figure 2.2 Illustration of the scattering of X-ray by a system containing a number of nanoparticles. The dependence of the scattering phase on the position of nanoparticles is indicated.

In a system containing many nanoparticles, the phase of the scattered beam from different nanoparticles varies from each other depending on their distribution in the system. Therefore, the scattering intensity of the system is written by

$$\begin{aligned}
 I(\vec{q}) &= F(\vec{q}) \cdot F^*(\vec{q}) \\
 &= \sum_j F_j(\vec{q}) \exp(i\vec{q} \cdot \vec{r}_j) \sum_k F_k(\vec{q}) \exp(-i\vec{q} \cdot \vec{r}_k) \\
 &= \sum_j \sum_k F_j(\vec{q}) F_k(\vec{q}) \exp[i\vec{q} \cdot (\vec{r}_j - \vec{r}_k)]
 \end{aligned} \tag{2.9}$$

where $F_j(\vec{q}) \exp(i\vec{q} \cdot \vec{r}_j)$ represents the scattering amplitude from j^{th} nanoparticles in the system. By isolating the $j = k$ term, the above equation can be simplified as:

$$I(\vec{q}) = \sum_j \left| F_j(\vec{q}) \right|^2 + \sum_j \sum_{k, k \neq j} F_j(\vec{q}) F_k(\vec{q}) \exp[i\vec{q} \cdot \vec{r}_{jk}] \tag{2.10}$$

The second term at the right hand of equation 2.10 in fact indicates the correlation among all nanoparticles, i.e. interference during the scattering.

As is introduced in Section 1.3.1.1 of Chapter 1, decoupling approximation (DA)^[51] has been widely used to simplify the calculation of equation 2.10. In DA, it is assumed that the distribution of nanoparticles is not correlated to their sizes. Therefore, DA is applicable to nanoparticles systems with narrow size distribution. In a system containing large number of nanoparticles, equation 2.10 can be considered from the point view of statistic quantities, and hence it can be further simplified into

$$I(\vec{q}) = \langle \left| F(\vec{q}) \right|^2 \rangle + \langle \left| F(\vec{q}) \right| \rangle^2 \cdot \rho_v \int_v g(\vec{r}) \exp(i\vec{q} \cdot \vec{r}) dv \tag{2.11}$$

where the triangular bracket $\langle \dots \rangle$ denotes the average over the size distribution of nanoparticles, ρ_v is the number density of nanoparticles and $g(\vec{r})$ is the pair correlation function which describes the possibility to find another nanoparticle at distance \vec{r} around the nanoparticle arbitrarily selected as the origin. The expression of scattering within DA is generally known in the form

$$I(\vec{q}) = \langle \left| F(\vec{q}) \right|^2 \rangle + \langle \left| F(\vec{q}) \right| \rangle^2 \cdot (S(\vec{q}) - 1) \tag{2.12}$$

with

$$S(\vec{q}) = 1 + \rho_v \int_v g(\vec{r}) \exp(i\vec{q}\vec{r}) dv$$

In equation 2.12, $\langle |F(q)|^2 \rangle$ is the form factor which is related to particle size and shape, while $S(q)$ is the structure factor which concerns the distribution of nanoparticles and the interference among them.

Within DA, by calculating the form factor and the structure factor separately using appropriate models, the theoretical scattering intensity can be derived. Details of such calculation will be shown in the following chapters when real nanoparticle systems are investigated.

2.2.1.2 Experiments of Small Angle X-ray Scattering

Synchrotron Radiation Source was used for SAXS experiments since it provides high flux and highly monochromatic X-ray beam which enables us to obtain strong scattering signal from a small amount of sample, and to monitor the dynamic changes in the sample with high time resolution, e.g. with 1 s or even shorter intervals between consecutive frames in our case. SAXS experiments were performed at beamline I22, Diamond Light Source, UK. 2-D scattering pattern was recorded by a PILATUS 2M detector (Dectris), and the sample-to-detector distance was calibrated by a standard sample of long alkane.

In SAXS experiments which did not involve dynamic change of the sample, e.g. to characterize morphology of HNPs, a simple routine was used to obtain the data, i.e. by holding the sample in thin wall capillary and exposing the capillary to X-ray.

In SAXS experiments involving dynamic change of the sample, i.e. diffusion of solvents into polymer-embedded HNPs, a home-made setup was used to obtain the real-time scattering data. The designed setup is shown in Figure 2.3. The capillary was connected to a remotely controlled injection system. The injection system mainly consists of a remotely controlled syringe pump (KD scientific, LEGATO 100, US), a syringe attached to the syringe pump and connected to the capillary, and a controlling computer. A video camera was placed in the

experimental hutch to visualize the propagation of the solvent front. Prior to the solvent diffusion experiments, the syringe was filled with solvent. Then, the solvent was slowly injected into the capillary. To make sure that the initial status of solvent diffusion was recorded, SAXS data acquisition started several seconds before the front of the solvent reaching the sample volume exposed to X-ray beam. This simple setup has many advantages. Firstly, it is easy to install and use. Secondly, it enables us to record the initial status of the dynamic process in the sample. Thirdly, visualization of the diffusion process enable us to select appropriate exposure time e.g. using 1 s per recording at the start of the diffusion, then 3 s per recording at the middle stage and even longer exposure times at the end.

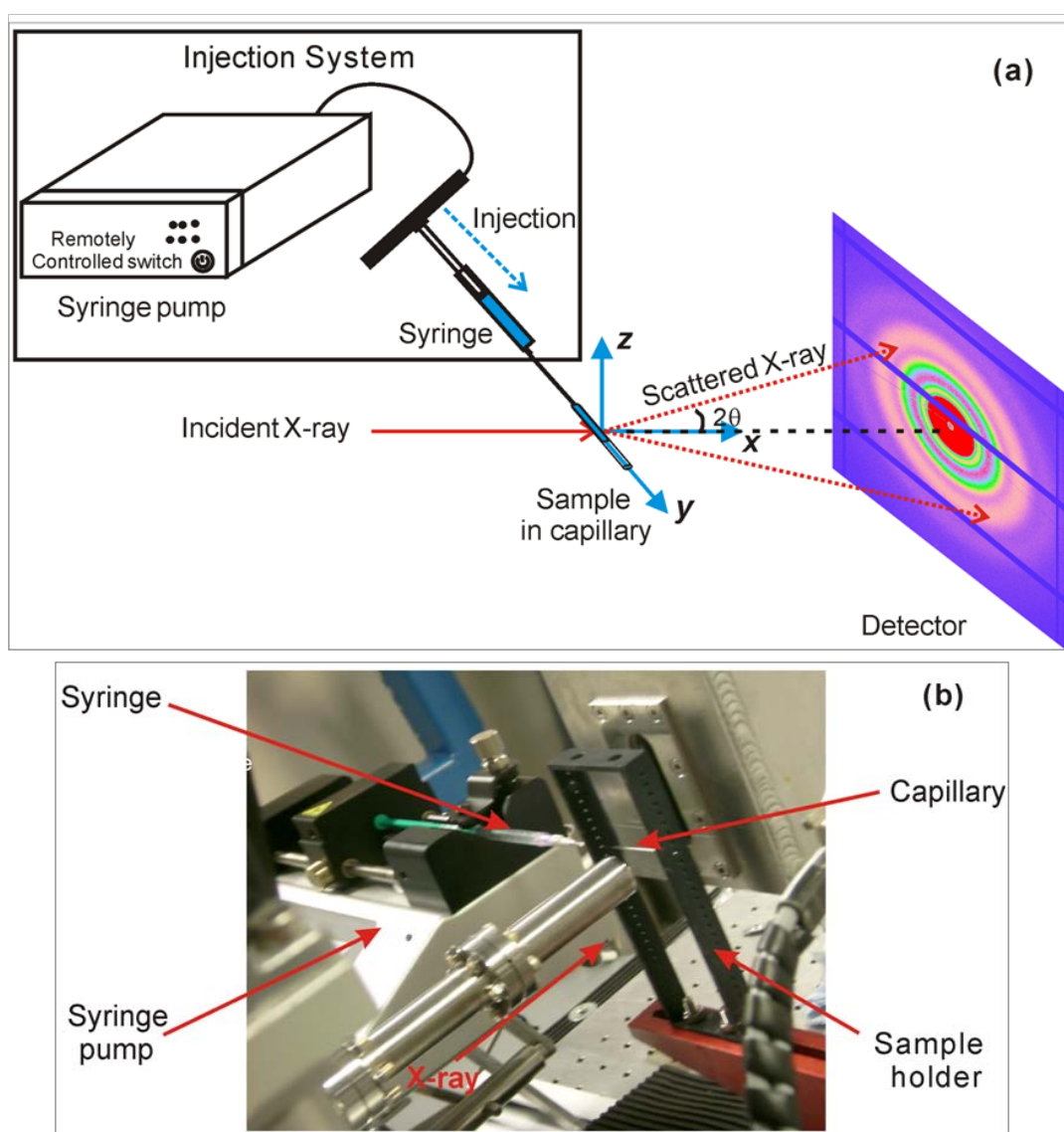


Figure 2.3 (a) Illustration of the SAXS setup for *in-situ* experiments and (b) Photograph of the real experimental setup.

2.2.2 Small Angle Neutron Scattering

2.2.2.1 Theoretical Basis of Small Angle Neutron Scattering

Small angle neutron scattering (SANS) has been widely used in the field of self-assemblies, porous materials, nanoparticles, and precipitates of metals *etc.*^[118] Like SAXS, SANS also adopts a transmission geometry normally. However, SANS is different from SAXS in some aspects. The scattering intensity of SANS arises from the interaction between neutrons and atomic nuclei, rather than X-ray photons and electrons. The contrast of different atoms in neutron scattering is different from that in X-ray, due to the difference in their scattering efficiency. In some of the elements, the difference in the scattering efficiency of isotopes can be very large, e.g. ^1H gives a negative scattering length while ^2H gives a positive scattering length. The incoherent scattering in SANS is due to the random difference in the scattering lengths of nuclei,^[119] while the incoherent scattering in SAXS arises from the energy loss of X-ray during scattering. SANS experiments generally requires larger amount of sample and more exposure time, because the flux of neutron source and the scattering power of atoms for SANS is much lower than those for SAXS.

Similar theoretical basis to that of SAXS can be applied to SANS when considering a nanoparticle system. The form factor and structure factor can be determined within the DA. However, in formulae of SANS, the scattering length density representing the distribution of the scattering efficiency of atoms to neutron should take the place of the electron density.

2.2.2.2 Experiments of Small Angle Neutron Scattering

SANS experiments were carried out at LOQ station at ISIS, Rutherford Appleton Laboratory in UK. A “white” incident beam is used together with a time-of-flight detector. A sample aperture with diameter of 12 mm was used. The colloidal solutions of HNPs in water (~3 wt%) were held in quartz cuvettes of 1 mm path length.

2.2.3 Grazing Incidence Small Angle X-ray Scattering

2.2.3.1 Theoretical Basis of Grazing Incidence Small Angle X-ray Scattering

In grazing incidence small angle X-ray scattering (GISAXS), the grazing incidence geometry enables many advantages when compared to normal SAXS and SANS. Firstly, since the refraction index of matter to X-ray is slightly less than 1, the total external reflection may occur when the incident angle is below the critical angle, which means the user can control the penetration depth of the X-ray beam into the sample by varying the incident angle. Secondly, by making use of a brilliant synchrotron X-ray source, GISAXS is extremely useful to probe the structure and dynamic process of a tiny scattered volume in a thin film deposited on a substrate.^[53, 57, 120-122] Thirdly, GISAXS gives excellent sampling statistics by averaging over macroscopic regions to provide information at nanoscale. However, the analysis of GISAXS data usually involves complex calculation due to the existence of reflection and refraction during the scattering. A simple illustration of the grazing geometry is shown in Figure 2.4. It can be seen that when the incident angle is higher than the critical angle, both refraction and reflection occur; however, when the incident angle is lower than the critical angle, the total external reflection takes place and only evanescent wave is travelling parallel to the surface with a penetration depth of only 5 - 10 nm for a typical organic film.

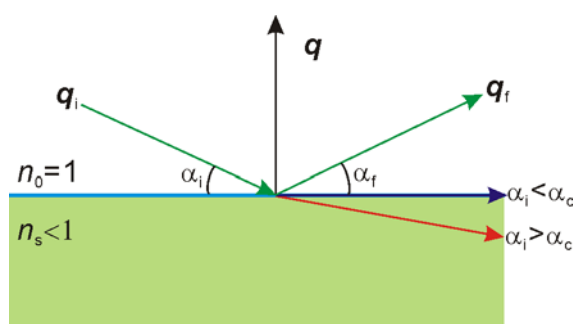


Figure 2.4 The grazing incidence geometry. q_i is the incident wave, α_i the incident angle, q_f the reflected wave, and α_f the reflected angle.

When considering a sample consisting of a flat substrate and many nanoparticles distributing on the substrate, due to the occurrence of refraction and reflection, the propagation of X-ray beam in such a sample mainly consists of four parts. The first part involves direct scattering of the incident X-ray beam by the nanoparticles. In the second part, the directly scattered beam is further reflected by the substrate. In the third part, the incident beam is reflected by the

substrate at first, and then the reflected beam is further scattered when it penetrates into nanoparticles. The fourth part involves one time of reflection both before and after the scattering. More complex situations, even though most of the time not necessary, may be considered for the propagation of the X-ray in GISAXS, e.g. secondary scattering of the scattered or reflected beam.

The distorted wave Born approximation (DWBA) has been developed to analyze the above described phenomenon in the GISAXS of nanoparticles systems.^[123-127] The DA can be also used for the calculation of the form factor and structure factor. However, it is noted that the form factor under DWBA consists of four form factors contributed by the above four parts of the propagation of X-ray, respectively. In some cases, e.g. when the incident angle is far away from the critical angle, the direct scattering of X-ray by the nanoparticles dominants, and hence similar formulae to SAXS can be used to analyze the GISAXS intensity.

2.2.3.2 Experiments of Grazing Incidence Small Angle X-ray Scattering

GISAXS experiments were carried out at beamline I07, Diamond Light Source in UK. Pre-cleaned silicon wafers, hydrophilically modified by plasma treatment, were used as substrates for GISAXS samples. HNPs were deposited from colloidal water solutions by spin coating at 1900 rpm for 30 s. The X-ray wavelength was $\lambda = 1.55 \text{ \AA}$. The incident angle was below the critical angle. A PILATUS 2M detector was used to record the 2-D scattering patterns.

2.3 Analysis Procedure for Small Angle Scattering Data

2.3.1 Reduction of Raw Data

In analysis to SAXS experimental data, 1-D scattering curves were obtained at first by azimuthally averaging the raw 2-D scattering pattern in a C program written by Dr. Xiangbing Zeng. Then, calibration for sample-to-detector distance was carried out by using a standard sample of a long alkane (n-C₂₄₆H₄₉₄) with a first order d-spacing of 258 Å. Prior to further data analysis for morphology of HNPs and polymer-embedded HNPs, scattering background,

arising from the X-ray capillary and the porous polymer (in the case of polymer-embedded HNP samples due to inhomogeneity of polymer matrix) was subtracted.

1-D scattering curves of SANS was obtained by reducing the raw data in the free software Mantidplot. The calibration of the sample-to-detector distance was automatically calibrated in the software. The scattering background from quartz cuvettes was subtracted.

The reduction of GISAXS experimental data was slightly different from that of SAXS and SANS due to the weak ordering of HNPs on the substrate which gave weak Bragg rod on the 2-D GISAXS pattern. Therefore, the azimuthally averaging of the raw 2-D pattern was done by carefully selecting only the circularly symmetrical features arising from form factor of HNPs. In this way, the calculation of the structure factor can be simplified by a disordered nanoparticle model. The other reduction procedure of GISAXS experimental data was the same as that of SAXS.

2.3.2 Correction for Instrumental Broadening

In small angle scattering experiments, the scattering data is usually influenced by the instrument smearing. There are mainly three factors contributing to the instrumental smearing, namely finite collimation, wavelength spread and detector resolution limitation. It is necessary to take them into account when dealing with experimental data, because they will cause systematic errors to the modelling and the derived parameters.^[128] Since the X-ray beam used in synchrotron station is generally monochromatic and the beamline usually has good collimation and detector resolution, the effect of instrumental broadening to SAXS and GISAXS data is negligible. For SANS experimental data, the method used to correct the instrument broadening is described below.

The correction of instrumental broadening for SANS data usually involves much numerical calculation. To simplify the calculation, Pedersen^[129] proposed a correction function which combines the smearing from the above mentioned factors, i.e. wavelength spread, finite collimation and detector resolution limitation. The measured broadened scattering intensity proposed by Pedersen can be expressed by^[129]

$$I(\langle q \rangle) = \int R(\langle q \rangle, q) \cdot I(q) dq \quad (2.13)$$

where $I(\langle q \rangle)$ is the measured intensity, $\langle q \rangle$ the average scattering vector related with the wavelength distribution width by $\langle q \rangle = 4\pi \sin \langle \theta \rangle / \langle \lambda \rangle$, $R(\langle q \rangle, q)$ is the resolution function combining the effect from all smearing factors, and $I(q)$ is the true unsmearred intensity function. A Gaussian function was proposed by Pedersen as the resolution function

$$R(q - \langle q \rangle) = \frac{1}{\sqrt{2\pi}\sigma} \exp\left(-\frac{(q - \langle q \rangle)^2}{2\sigma^2}\right) \quad (2.14)$$

where σ is the standard deviation. For calculation of the broadened intensity, equation 2.13 has to be done numerically by^[130]

$$I(\langle q \rangle_i) = \sum_j^N R(q_j - \langle q \rangle_i, q_j) I(q_j) \Delta q \quad (2.15)$$

Where $I(\langle q \rangle_i)$ is the broadened intensity, $\langle q \rangle_i$ is the experimental q value, q_j is the q value within the interval between $(\langle q \rangle_i - 3\sigma)$ and $(\langle q \rangle_i + 3\sigma)$, and $\Delta q = q_j - q_{j-1}$. Usually $N = 10-20$ gives sufficient accuracy.

In our analysis to SANS data, instead of doing de-convolution to the experimental data to remove the instrumental broadening, the smearing function was added to the theoretical SANS intensity, and the smeared theoretical SANS data was then fitted to the experimental intensity to obtain the best fit. In the SANS data for HNPs, the standard deviation σ was taken as a constant value of 0.02 nm^{-1} , which is more or less the value according to the q resolution of the LOQ instrument at ISIS measured by Richard K Heenan,^[131] in the q value range of interest for our samples from 0.1 nm^{-1} to 1 nm^{-1} .

2.3.3 The Fit Routine

Based on the form factor function and structure factor function in the small angle scattering models, the calculated scattering intensity was then compared to the experimental intensity to extract parameters from the best fit. C programs were written for the fit with the free C

compiler system Lcc-win, which was published online by Jacob Navia via <http://www.cs.virginia.edu/~lcc-win32/>. The best fit was determined by searching the minimum value of the reduced χ^2 , defined by^[60]

$$\chi^2 = \frac{1}{N-M} \sum_{i=1}^N \left(\frac{I^{\text{exp}}(q_i) - I^{\text{cal}}(q_i)}{\mu(q_i)} \right)^2 \quad (2.16)$$

where N is the number of data points, M the number of fit parameters, $N - M$ is the number of degree of freedom, $I^{\text{exp}}(q)$ is the experimental scattering intensity, $I^{\text{cal}}(q)$ the calculated scattering intensity, and $\mu(q)$ the statistical uncertainty of the data point.

The fitting process in the C programs mainly consists of five steps. Firstly, the experimental scattering intensity is loaded into the program. Secondly, the boundary region of each parameter in the form factor and structure factor model is defined, followed by assignment of the initial value of each parameter. Thirdly, the theoretical scattering intensity is calculated with the value-assigned parameters, and the difference between the experimental intensity and calculated intensity is determined by the value of χ^2 which will be used to compare with that from the next group of parameters. Fourthly, the value of χ^2 associated with each group of parameters within the boundary region is compared and the minimum value of χ^2 is found. Finally, the parameters and calculated scattering intensity associated with the minimum χ^2 are output from the program.

2.4 Gas Adsorption Methods

In this section, gas adsorption isotherm methods as applied to porous materials in general is introduced briefly. In the final paragraph of this section HNPs are specifically referred to. In the general part the term “mesopores” is used to describe the large holes, and “micropores” is used to describe the channels or cracks in the walls separating them; the term “pores” is used here to cover all pores. At the initial stage of adsorption, the entire pore space is accessible to the outside gas molecules, and absorbed layers form on the pore walls. As the vapour pressure increases, the micropores fill up with condensate, as the liquid phase is stabilized by the high wall curvature.^[132] Meanwhile the layers adsorbed in the inner cavity continue to increase in

thickness via diffusion through the micropores. Eventually the condensate fills the mesopores. However, during desorption, the reverse process is delayed as the evaporation of liquid in the mesopores is blocked by the condensate in the micropores.^[133-135]

Different methods have been developed to extract morphological information from the nitrogen isotherms, i.e. specific surface area, volume and diameter of micropores, and pore volume distribution. Cylindrical^[136] and spherical^[137] pore models have been used. Three of such methods that are applied in this project, i.e. Brunauer-Emmett-Teller (BET) method,^[138] t -plot method,^[139] and spherical pore model based on Kelvin equation,^[137] are summarized below.

BET method has been widely applied to obtain the surface area of mesoporous materials. In BET, multilayers of N₂ adsorbed on the bare surface are considered. It is assumed that adsorption of new molecules is not influenced by the existing molecules in the same layer. Additionally, it is assumed that, at equilibrium, the surface area covered by a certain layer thickness keeps constant since the rates of condensation and evaporation are balanced. A convenient form of the BET equation is given by^[138]

$$\frac{p}{v(p_0 - p)} = \frac{1}{v_m c} + \frac{c-1}{v_m c} \frac{p}{p_0} \quad (2.17)$$

where p_0 is the saturation pressure, p the actual pressure, v_m is the volume of adsorbed N₂ when all surface is covered by an unimolecular layer, and c is a constant related to the difference in adsorption enthalpy of the first layer and that of subsequent layers. At low relative pressures, by plotting the linear relationship between $p/v(p_0-p)$ and p/p_0 , one can obtain the values of v_m and c from the slope and the intercept. The total surface area is then derived by taking into account the thickness of the monolayer of adsorbing molecules. This method can only be applied at very low relative pressures ($p/p_0 \leq 0.2$), as it does not take into account the filling of pores.

The t -plot method, developed by de Boer and co-workers,^[139] has been used to determine the total volume of micropores and the surface area outside the micropores.^[140, 141] In this method, the volume-pressure relationship in the adsorption isotherm is converted to a relationship between volume and thickness of the adsorbed layers t using different functions, the most common being the semi-empirical equation by Harkins and Jura (HJ)^[142]

$$\log_{10}(p / p_0) = 0.034 - 13.99 / t^2 \quad (2.18)$$

where t is in Å. The curve relating the adsorbed volume and t obtained from Equation 2.18 is referred to as the t -curve. The t -plot method is applicable above the pressure at which all micropores had been filled with condensed liquid, i.e. where the t -curve becomes linear. Above that pressure layer-by-layer adsorption on the walls of mesopores continues, the increase in the adsorbed volume being linearly related to the increase in the layer thickness. Thus a straight line is fitted to the linear range of the t -curve, usually the range $3.5 \text{ \AA} < t < 10 \text{ \AA}$. The volume of micropores is then taken as the value of the straight line extrapolated to $t = 0$. The surface area outside the micropores is obtained from the slope.

The HJ equation applies to both the t -plot and another method, used for calculating volume distribution dV_p/dr_p of all pores in the material. This method, based on a classical work by Kelvin, is described in the following. For the calculation of pore volume distribution it is assumed that, as the vapour pressure increases, the thickness of the adsorbed layer in the pores eventually reaches a critical value beyond which condensation takes place in the remaining capillary or bubble of radius r_K .^[137] The radius of the pore experiencing condensation r_p is thus $r_p = r_K + t$. For spherical pores r_K (in Å) can be given by the Kelvin equation^[143]

$$r_K = -\frac{2\gamma V_0}{R_g T \ln(p / p_0)} \quad (2.19)$$

Here γ is surface tension of liquid nitrogen, V_0 is its molar volume, and R_g is the gas constant. As t and r_K are both dependent on pressure, condensation in pores with different sizes occurs at different pressures. Therefore, by computing r_p through the whole pressure range, the volume distribution of the pores is obtained. For simplicity, calculation of the distribution of inner radii normally starts at the end point of the isotherm (saturation pressure, designated as experimental step $n = N$) and proceeds backward to the beginning of the isotherm, i.e. from $n = N$ to $n = 1$. This reversed sequence is similar to the algorithm in the traditional Barrett-Joyner-Halenda (BJH) method.^[136] Based on equation 2.18 and 2.19, the volumes of spherical pores with different radii can be calculated from experimental data using^[137]

$$\Delta V_{p,n} = \left(\frac{\bar{r}_{p,n}}{r_{p,n} - t_n} \right)^3 \cdot (\Delta V_n - \Delta t_n \sum_{i=n+1}^N \frac{3\Delta V_{p,i}}{r_{p,i}} + \Delta t_n \cdot \bar{t}_n \cdot \sum_{i=n+1}^N \frac{6\Delta V_{p,i}}{(r_{p,i})^2} - \Delta t_n \cdot (\bar{t}_n)^2 \cdot \sum_{i=n+1}^N \frac{3\Delta V_{p,i}}{(r_{p,i})^3}) \quad (2.20)$$

ΔV_n is the change in the measured adsorbed volume at point n . $\Delta V_{p,n}$ is the volume of pores with radius $r_{p,n}$. ΔV_{pN} is easily obtained since, for $n = N$, the last three terms in equation 2.20 vanish. At any step $n < N$, the contribution to ΔV_n comes not only from condensation in the pores of radius $r_{p,n}$, but also from layers adsorbed on the walls of pores with a radius larger than $r_{p,n}$. Hence the volume distribution of pores with different radii is obtained.

For HNPs studied here, the term intrawall pores refers to the pores in the HNP shells. The inner cavities of our HNPs, with diameters of the order $10^1 - 10^2$ nm, span the mesopore and macropore categories as defined by IUPAC.^[144] Equation 2.20 is used by assuming spherical pores. For simplicity we have applied it to HNPs despite the fact that intrawall pores in the shells may be cylindrical or of another shape; this is justified since the adsorption isotherm is dominated by the spherical inner cavities.

Raw data of N_2 adsorption and desorption isotherms was recorded by Chanhoi Kim in Seoul National University by using an ASAP2000 instrument (Micromeritics) at 77.35 K. Before the experiments, the samples were degassed at 110 °C for 20 h. The specific surface area, the pore volume distribution as a function of pore diameter, and in some cases the specific inner cavity volume of HNPs were characterized.

2.5 Dynamic Light Scattering

Dynamic light scattering (DLS) is often used to measure the size and distribution of nanoparticles. Due to Brownian motion of the nanoparticles, the intensity of scattered laser light fluctuates with time. The dynamic information can be retrieved by examining the autocorrelation function $g(q, \tau)$ of the time-dependant intensity $I(q, t)$

$$g(q, \tau) = \frac{\langle I(q, t)I(q, t + \tau) \rangle}{\langle I(q, t) \rangle^2} \quad (2.21)$$

A time correlation function $G(q, \tau)$ can be defined, which is related to $g(q, \tau)$ by

$$g(q, \tau) = 1 + G^2(q, \tau) \quad (2.22)$$

For optically isotropic particles that are sufficiently diluted so that interactions between particles can be neglected,

$$G(q, \tau) = \sum_i G_i \exp(-\Gamma_i \tau) \quad (2.23)$$

Here Γ_i is the rate of correlation decay, determined by the translational diffusion coefficient D_T of nanoparticles. D_T is related to the hydrodynamic radius R_H by the Einstein-Stokes law

$$R_H = \frac{k_B T}{6\pi\eta_s D_T} \quad (2.24)$$

where k_B is the Boltzmann constant, η_s is the viscosity of the solvent. Therefore, by determining the decay rate Γ_i and the corresponding scattering power G_i , the size distribution of HNPs can be determined.^[145]

The DLS data was measured by Chanhoi Kim in Seoul National University. An ELS-8000 instrument (Otsuka Electronics, Japan) was used to obtain the DLS data.

CHAPTER 3 Size and Shell Porosity of Hollow Nanoparticles

Abstract

A combination of experimental methods, including transmission and grazing incidence small angle X-ray scattering (SAXS and GISAXS), small angle neutron scattering (SANS), transmission electron microscopy (TEM), dynamic light scattering (DLS), and N₂ adsorption-desorption isotherms, were used to characterize SiO₂/TiO₂ hollow nanoparticles (HNPs) of sizes between 25 and 100 nm. In the analysis of SAXS, SANS and GISAXS data the decoupling approximation and the Percus-Yevick structure factor approximation were used. Brunauer-Emmett-Teller, t-plot and a spherical pore model based on Kelvin equation were applied in the treatment of N₂ isotherms. Extracted parameters from the scattering and TEM methods are the average outer and inner diameters, and polydispersity. Good agreement was achieved between different methods for these extracted parameters. Merits, advantages and disadvantages of the different methods are discussed. Furthermore, the combination of these methods provided us with information on the porosity of the shells of HNPs and the size of intrawall pores, which are critical to the applications of HNPs as drug delivery vehicles and catalyst supports.

KEYWORDS: Hollow nanoparticles, Small-angle X-ray scattering, Small-angle neutron scattering, Nitrogen adsorption isotherms, Intrawall pore, Porosity.

*Chen, Z. H., Kim, C., Zeng, X., Hwang, S. H., Jang, J. & Ungar, G. *Langmuir*, 2012, 28, 15350-15361.

3.1 Introduction

HNPs are important candidates for a range of applications, primarily as drug delivery vehicles and catalyst supports. There has been substantial progress in their synthesis.^[2, 3, 25, 28, 31, 146] Compared with traditional delivery vehicles, HNPs allow large and controlled drug loading levels, retain their stability in human bodily fluid, and are able to overcome cell and tissue barriers and release the drug at predetermined locations.^[147] HNPs also exhibit high catalytic activities since their inner and outer surfaces are accessible to reactants.^[148]

The drug release behavior and catalytic activity of HNPs are strongly influenced by their morphology. HNP size will affect the level of cellular uptake of the drug, cytotoxicity and immune response.^[149, 150] The shell thickness and porosity will affect the drug transport efficiency, drug loading concentration and the release rate.^[27, 151, 152] The drug release rate directly influences the efficiency of drug action.^[153] There have been various studies of particle size and polydispersity by TEM, DLS and nitrogen adsorption analysis.^[150, 152-155] Also SAXS and SANS have been used.^[156, 157] Some recent studies have correlated SANS/SAXS data and gas adsorption isotherms in mesoporous ceramics in order to understand the adsorption/desorption process and help interpret the isotherms. For instance, Pikus and co-workers characterized the size of intrawall pores ranging from 1.4 nm and 5.2 nm by analyzing the changes in the scattering background in SAXS, and good agreement was achieved for pores smaller than 2.6 nm. However, for pores bigger than 2.6 nm large discrepancies remained.^[158] Mascotto and co-workers analyzed the intrawall pore size and the porosity value of the silica matrix by comparing the *in-situ* SANS/SAXS results based on scattering contrast matching and nitrogen adsorption analysis.^[159] The characterized size of intrawall pores was around 1.3 nm while the porosity of the matrix was around 0.25. Jähnert and co-workers applied a gradient density model for analyzing SAXS data obtained during fluid adsorbing, and the volume fraction of micropores to the whole material was calculated.^[160] However, no such studies have been performed on hollow nanoparticles. Also, since all these techniques have their limitations, and a multi-technique approach is desirable for obtaining the full picture.

Here we describe the use of SAXS, including grazing incidence SAXS (GISAXS), as well as SANS, to characterize HNPs. These scattering methods are then compared with the results of

TEM, DLS, and nitrogen adsorption isotherm methods on three SiO₂/TiO₂ HNP model systems to obtain a detailed picture of the HNP hierarchical morphology. Specifically, by combining SAXS results with nitrogen adsorption analysis results, we derived a series of equations to obtain the intrawall pore size and the porosity of the shell. After experimental methods in Section 3.2, Section 3.3 outlines the working principles of the different methods used. The experimental results of characterization of SiO₂/TiO₂ HNPs are described in Section 3.4, where the results are also discussed and the methods compared. The chapter ends with general conclusions (Section 3.5).

3.2 Experimental Section

3.2.1 Materials

The synthesis of HNPs has been described in Section 2.1.1 of Chapter 2, and no more details are explained here.

In this chapter, SiO₂/TiO₂ hollow nanoparticles labeled HNP25, HNP50 and HNP100, with nominal outer diameter of 25 nm, 50 nm, and 100 nm, were investigated.

3.2.2 Methods

Details of SAXS experiments have been presented in Section 2.2.1.2 of Chapter 2. The method to reduce raw SAXS data can be found in Section 2.3.1 of Chapter 2.

Details of SANS experiments have been presented in Section 2.2.2.2 of Chapter 2. The principle to correct the instrumental smearing to the experimental data has been explained in Section 2.3.2 of Chapter 2. The method to reduce raw SANS data can be found in Section 2.3.1 of Chapter 2.

Details of GISAXS experiments have been presented in Section 2.2.3.2 of Chapter 2. The method to reduce raw GISAXS data can be found in Section 2.3.1 of Chapter 2.

An energy-filtering TEM (Carl Zeiss, LIBRA 120), working at 120 kV, was used. For these observations, the HNPs were diluted in ethanol and the diluted solution was deposited on a copper grid coated with carbon film.

The principle and experimental details of N₂ adsorption and desorption isotherm method have been presented in Section 2.4 of Chapter 2.

DLS data were acquired using an ELS-8000 instrument (Otsuka Electronics, Japan). HNPs were well dispersed in deionized water by sonication before the experiments.

The raw data of TEM, DLS, and N₂ adsorption-desorption isotherm was recorded by Chanhoi Kim and Sun Hye Hwang.

3.3 Theoretical Basis

3.3.1 SAXS and SANS

SAXS and SANS intensities are the Fourier transforms of the correlation function, which in turn is a product of the form factor and the structure (interference) factor.^[161, 162] The form factor is related to particle size and shape, while the structure factor concerns particle arrangement. When the size distribution of a particle system is narrow, the decoupling approximation (DA)^[51] is usually used, where the form factor and the structure factor can be determined separately.

Within the DA, the scattering intensity can be expressed by^[51]

$$I(q) = \langle |F(q)|^2 \rangle + |\langle F(q) \rangle|^2 \cdot [S(q) - 1] \quad (3.1)$$

where q is the scattering vector related to the scattering angle 2θ and the X-ray wavelength λ by $q = 4\pi \sin\theta / \lambda$. $\langle |F(q)|^2 \rangle$ is the form factor and $S(q)$ the structure factor. For SAXS, $F(q)$ is the Fourier transform of the electron density of a particle ($\rho(r)$ for a spherical particle) and can be written as

$$F(q) = \int_0^{\infty} 4\pi r^2 \cdot \rho(r) \cdot \frac{\sin qr}{qr} dr \quad (3.2)$$

For SANS the electron density distribution $\rho(r)$ is replaced by the scattering length distribution. Form factors have been proposed for hollow^[86, 87] and core-shell^[80, 84, 163] particles. In this study the HNP is modeled as a hollow sphere with a shell of constant electron density. When the electron densities inside and outside a HNP are equal, the Fourier transform is given as

$$F(q) = \frac{4\pi\Delta\rho}{q^3} [(\sin qR_0 - qR_0 \cos qR_0) - (\sin qr_0 - qr_0 \cos qr_0)] \quad (3.3)$$

Here R_0 and r_0 are the outer and inner radii of the HNP, and $\Delta\rho$ the electron density (scattering length) difference between the shell and the surrounding medium.^[74, 87, 164]

According to Equation 3.1, the form factor needs to be averaged over the size distribution of particles if they are of different sizes. The expression for the form factor involving a distribution of sizes is^[165]

$$\langle |F(q)|^2 \rangle = \int_0^{\infty} |F(q)|^2 \cdot h(R) dR \quad (3.4)$$

$$|\langle F(q) \rangle|^2 = \left| \int_0^{\infty} F(q) \cdot h(R) dR \right|^2 \quad (3.5)$$

where $h(R)$ is the size distribution function. In the above equations the inner-to-outer radius ratio for a particle is assumed constant, so that only the distribution of outer radii is considered. The two-parameter unimodal Schulz distribution function is used, as defined by^[85]

$$h(R) = \frac{1}{z!} \cdot \left(\frac{z+1}{R_0}\right)^{z+1} \cdot R^z \exp\left[-\frac{(z+1)R}{R_0}\right] \quad (3.6)$$

where R_0 is the averaged outer radius, and z is a parameter related to the relative standard deviation of the outer radius by $\sigma = 1/\sqrt{(1+z)}$ ($z=0,1,2,\dots$). Schulz distribution function

almost coincides with Gaussian function if the polydispersity is small, but is asymmetric and skewed to larger sizes if the polydispersity is large. Schulz distribution has been widely used for bio-molecular and other systems that tend to aggregate.^[74, 75, 88]

The structure factor $S(q)$ is determined by the arrangement of HNPs in space. In a randomly disordered hard sphere system, as there are only short range interactions, the total correlation within the system can be described by direct correlation between two neighboring particles and by indirect correlation among all the other neighboring particles via a convolution.^[97] This will include all correlations of the particles in the system. A successful approximation for the direct correlation function was given by Percus and Yevick (PY approximation).^[96] PY approximation has been widely used for particle systems.^[96, 98-100, 166] The structure factor in PY approximation is given by^[96]

$$S(q) = \frac{4\pi R_0^3}{4\pi R_0^3 - 3\eta \cdot C(q)} \quad (3.7)$$

where η is the volume fraction of the particles, and $C(q)$ is the direct structure factor, i.e. the Fourier transform of the direct pair correlation function $C(r)$. For an isotropic system, $C(q)$ can be expressed as

$$C(q) = \int_0^{2R_0} 4\pi r^2 \cdot C(r) \cdot \frac{\sin qr}{qr} dr \quad (3.8)$$

$C(r)$ is given by

$$C(r) = \begin{cases} \alpha + \xi \cdot \frac{r}{2R_0} + \delta \cdot \left(\frac{r}{2R_0}\right)^3, & r < 2R_0 \\ 0 & , \quad r \geq 2R_0 \end{cases} \quad (3.9)$$

where $\alpha = -(1+2\eta)^2/(1-\eta)^4$, $\xi = 6\eta(1+0.5\eta)^2/(1-\eta)^4$, and $\delta = -0.5\eta(1+2\eta)^2/(1-\eta)^4$.

To illustrate the sensitivity of SAXS to HNP parameters, simulated diffraction patterns are shown in Figure 3.1a, 1b, 2a and 2b. Figure 3.1a shows the compression of the curves along the q -axis as the sphere radius increases. In Figure 3.1b, as the ratio of the shell thickness to the outer radius increases, i.e. as the wall thickens while the median radius $(R_0+r_0)/2$ is kept constant, the position of the first minimum and maximum in the scattering curves moves to somewhat lower q ; and the overall slope of the curve changes. In Figure 3.2a, as the polydispersity increase, the peaks and troughs tend to iron out. In Figure 3.2b, one can see how the increasing interparticle correlation with increasing volume fraction affects the shape of the first intensity peak around $q = 0.15 \text{ nm}^{-1}$. Specifically, two shoulders gradually appear on each side of the first maximum. It can also be seen how sensitive the low- q region ($q < 0.1 \text{ nm}^{-1}$) is to the increasing volume fraction and interparticle correlation. Figure 3.2b also illustrates the desirability of working with a dilute system when the aim is to characterize particle shape by SAXS or SANS.

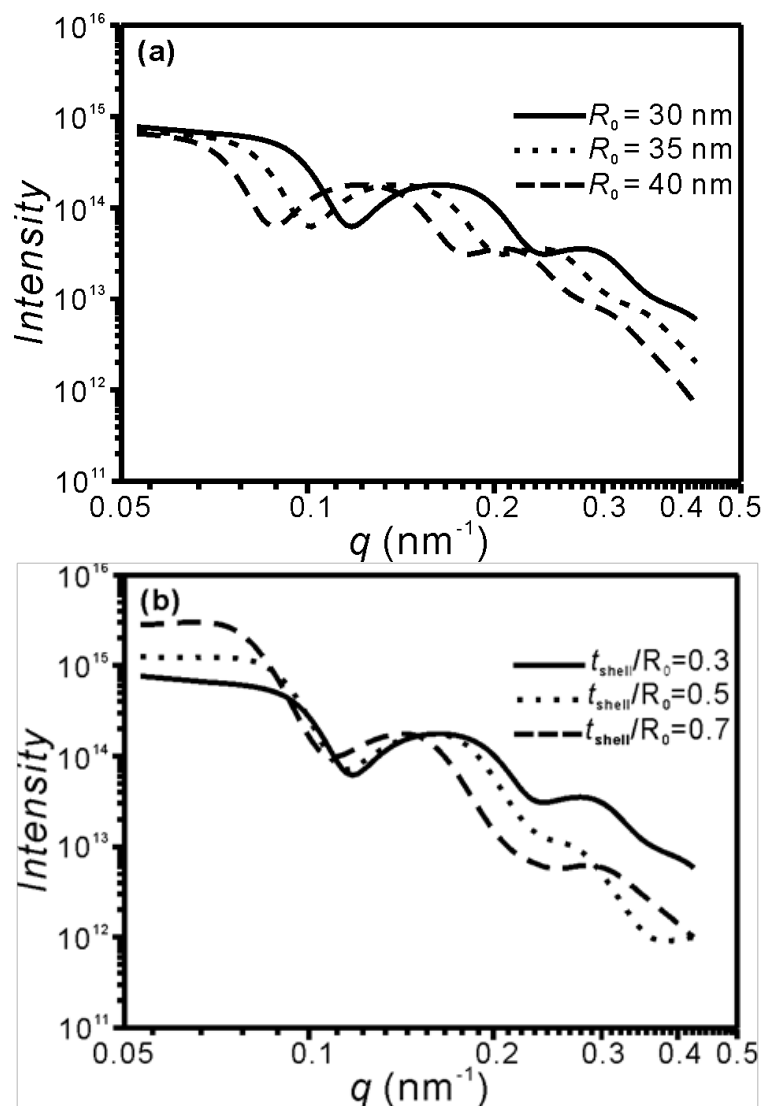


Figure 3.1 (a) Calculated scattering curves for HNPs with different outer radii R_0 . Solid line: $R_0=30$ nm, dotted line: $R_0=35$ nm, dashed line: $R_0=40$ nm. The ratio of shell thickness ($t_{shell} = R_0 - r_0$) to outer radius is $t_{shell}/R_0 = 0.3$, size distribution parameter $\sigma=0.11$ ($z = 80$), volume fraction $\eta = 0.3$. The relative standard deviation of the outer radius σ is related to z by $\sigma = 1/\sqrt{(1+z)}$ ($z = 0, 1, 2, \dots$). (b) Calculated scattering curves for HNPs with $(R_0+r_0)/2 = 25.5$ nm and different t_{shell}/R_0 ratios. Solid line: $t_{shell}/R_0 = 0.3$, dotted line: $t_{shell}/R_0 = 0.5$ nm, dashed line: $t_{shell}/R_0 = 0.7$ nm. Other fixed parameters are $\sigma = 0.11$ ($z = 80$), and $\eta = 0.3$. Note that the solid curve in (a) and (b) is the same.

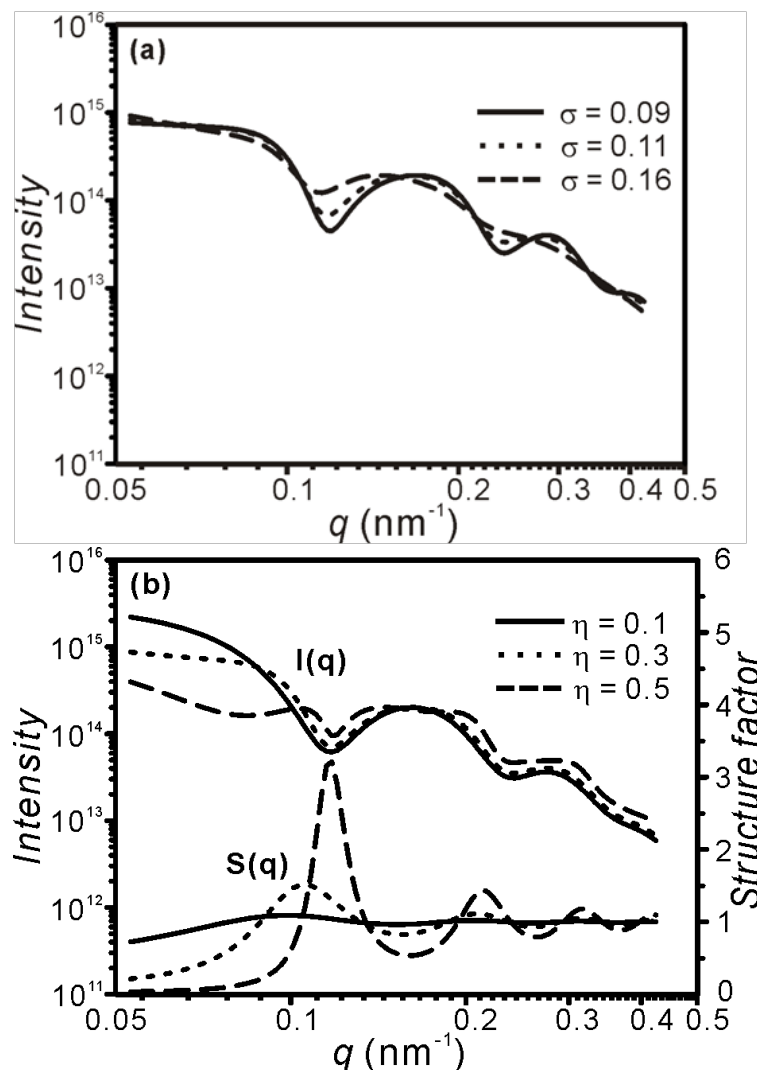


Figure 3.2 (a) Calculated scattering curves for HNPs with different polydispersities. solid line $\sigma = 0.09$ (corresponding to $z = 120$), dotted line $\sigma = 0.11$ ($z = 80$), and dashed line $\sigma = 0.16$ ($z = 40$). Fixed parameters are $R_0 = 30 \text{ nm}$, $r_0 = 21 \text{ nm}$, $\eta = 0.3$. (b) Calculated intensity curves $I(q)$ and structure factor curves $S(q)$ for HNP with varying particle volume fraction η : solid line for $\eta = 0.1$, dotted line for $\eta = 0.3$, and dashed line for $\eta = 0.5$. Fixed parameters are $R_0 = 30 \text{ nm}$, $r_0 = 21 \text{ nm}$ and $\sigma = 0.11$ ($z = 80$). In both (a) and (b), the curves are scaled to equal height of the first maximum ($q \sim 0.15 \text{ nm}^{-1}$). Note that the dotted line in (a) and (b) for scattering intensity is the same.

On the basis of the DA and PY approximations, the scattering intensity from HNPs can thus be calculated, and the parameters of HNPs can be retrieved by fitting the experimental data. In this study the analytical expression for scattered intensity was derived – see Section A.1 in the Appendix of the thesis. C programs were written for the fitting. The best fit was determined by searching for the smallest χ^2 .

3.3.2 Gas Adsorption Methods

Details about the theoretical basis of gas adsorption-desorption method can be found in Section 2.4 of Chapter 2.

3.3.3 Dynamic Light Scattering

Details on the theoretical basis of dynamic light scattering can be found in Section 2.5 of Chapter 2.

3.4 Results and Discussion

In section 3.4.1 we present and compare the results of measurements of outer and inner radii and size distributions of these HNPs as obtained by different experimental methods. This is followed by a discussion on the porosity of the shell and the size of intrawall pores, combining the data from N₂ adsorption-desorption isotherms and SAXS (or GISAXS).

3.4.1 Size and Distribution of Hollow Nanoparticles

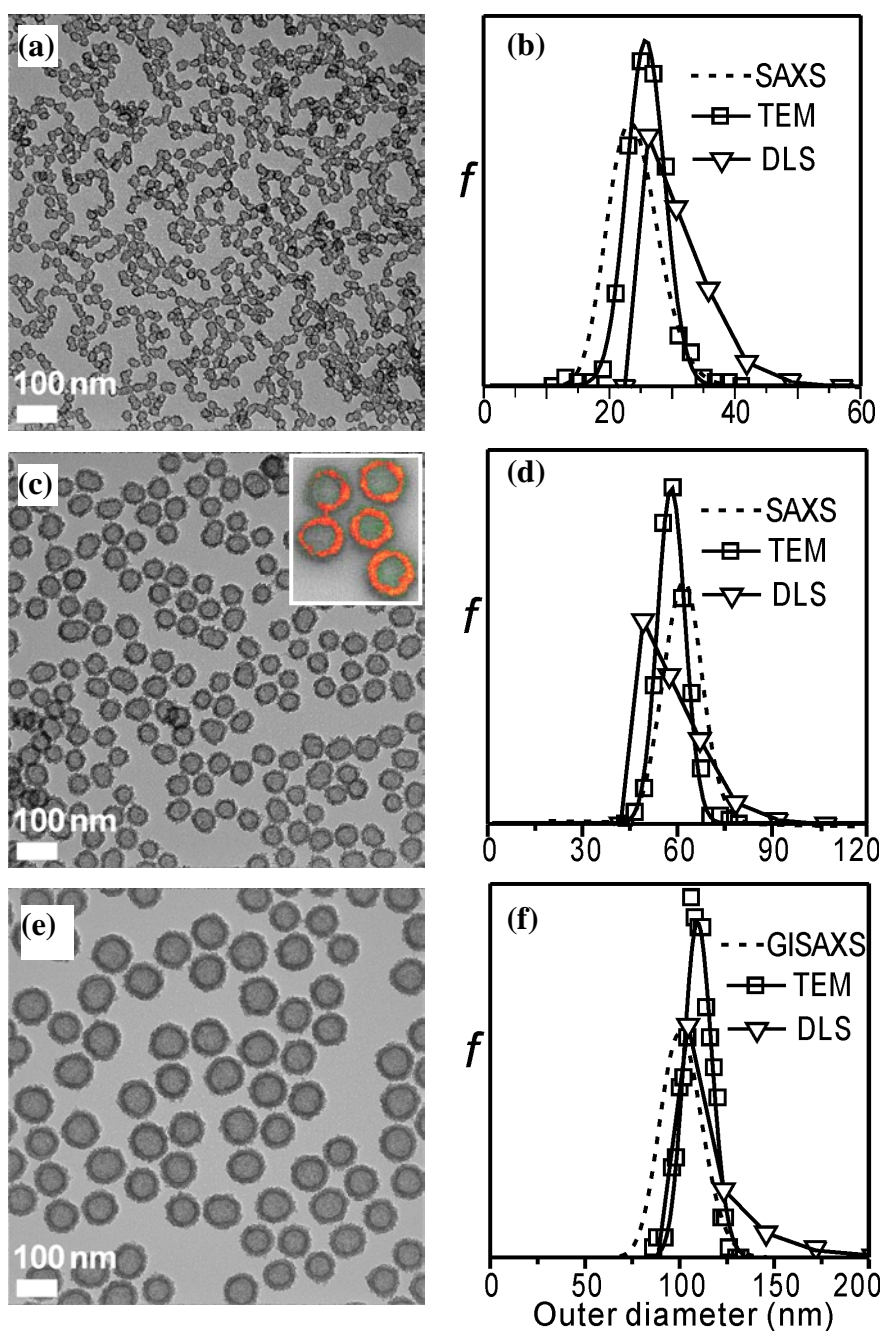


Figure 3.3 TEM images of (a) HNP25, (c) HNP50 and (e) HNP100. Outer diameter distributions from TEM images, DLS measurements and SAXS (or GISAXS) fitting are shown in (b) for HNP25, (d) for HNP50 and (f) for HNP100. f is the number frequency. All distributions for a given HNP size are normalized to the same area. Inset in (c) is electron energy loss spectroscopy (EELS) dot mapping of five HNPs; false color code: Si = green, Ti = red. The TEM images, DLS raw data and EELS dot mapping image were supplied by Chanhoi Kim and Sun Hye Hwang.

TEM images of HNP25, HNP50 and HNP100 are shown in Figure 3.3a, c and e, respectively. It can be seen that HNPs are mostly spherical and fairly uniform in size. In each HNP the inner cavity can be easily discerned. To confirm the chemical composition of fabricated HNPs, electron energy loss spectroscopy (EELS) dot mapping was performed on core/shell and hollow nanoparticles, i.e. before and after ammonia treatment. A representative EELS image of HNPs after the treatment is displayed in Figure 3.3c (inset). The color-coded image shows that the interior of the particles is empty (black). The orange color of the shell indicates that it combines both silicon (green) and titanium (red) dioxide, with a thin layer of predominant silica on the inner and the outer surface.

To obtain the size from TEM images, radial scans of grayscale distribution in the images were performed for a number of particles (314, 316 and 309 nanoparticles in the case of HNP25, HNP50 and HNP100, respectively). Outer and inner radii were taken as the distance from the centre of the particle to the outer and inner sides of the peak measured at half height from the baseline. The measured size distributions are plotted in Figures 3.3b, d, and f for HNP25, HNP50, and HNP100, respectively. The size distribution curves were normalized to the same peak area. All three samples show relatively small polydispersity and their size distributions can be fitted well by a Schulz function (Equation 3.6). The values are given in Table 3.1, which is presented slightly later.

The data calculated from dynamic light scattering are superimposed in Figure 3.3b, d, f. The DLS data also show small polydispersity, but unlike the distributions from TEM, DLS size distributions are clearly asymmetric.

HNP25 and HNP50 were recorded by SAXS and SANS in water solution, while HNP100 as well as HNP50 were recorded by GISAXS in the form of a thin film on Si. To obtain size parameters from SAXS and GISAXS, a hollow sphere model was used within the DA and PY approximations, as described in Section 3.3.1. Four parameters were used to describe the morphology of HNPs, namely outer radius, inner radius, outer radius distribution and particle volume fraction.

The experimental and fitted curves for HNP25, HNP50, and HNP100 are shown in Figure 3.4. To obtain 1D scattering curves, radial scans were performed on the 2D SAXS or GISAXS

patterns. For GISAXS patterns, the low intensity regions below the Yoneda line and the region of weak ordering (Bragg rods) were excluded.

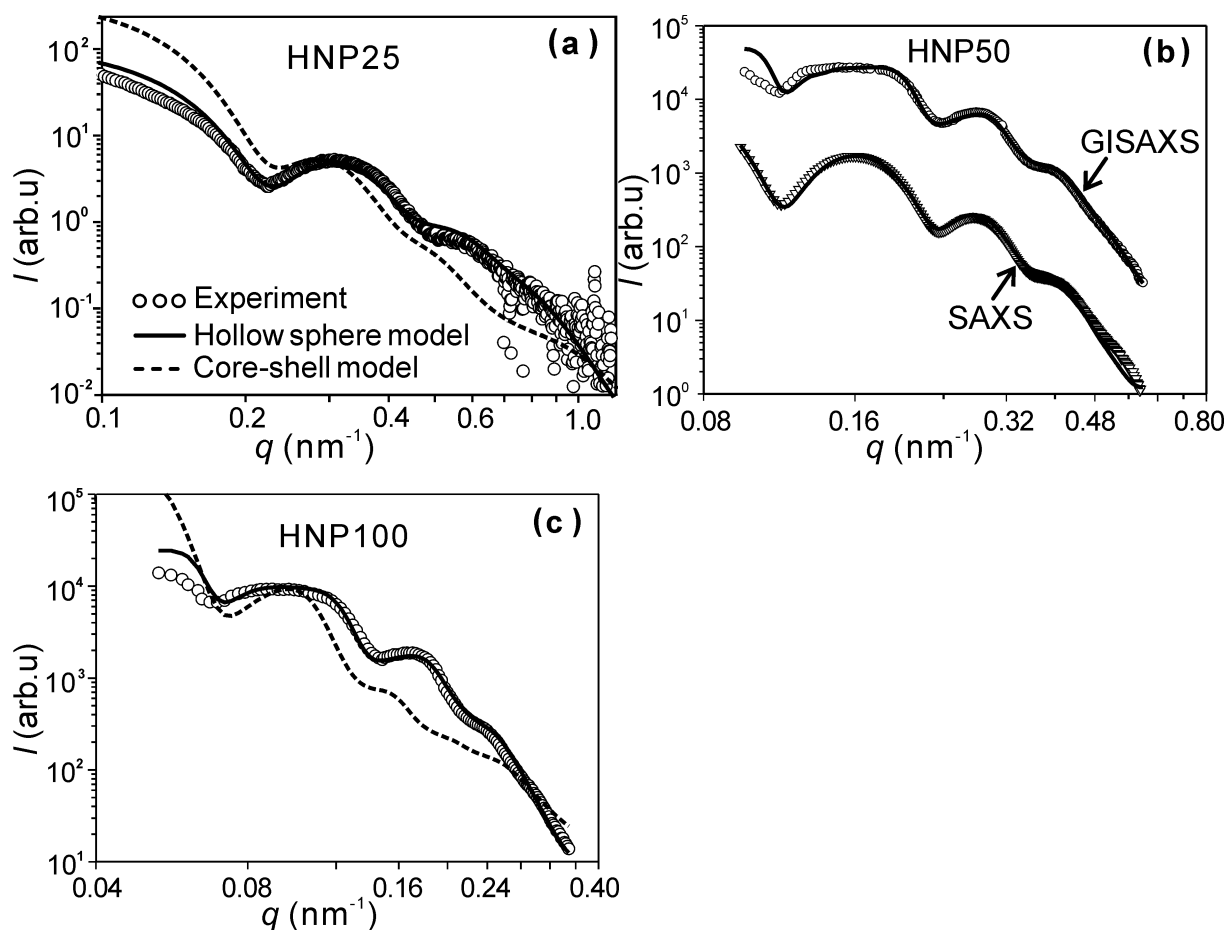


Figure 3.4 Experimental curves (open symbols) and fitted curves (lines) for hollow nanoparticles. (a) HNP25 by SAXS (~ 5 wt%), (b) HNP50 by SAXS (~ 5 wt%) and GISAXS, and (c) HNP100 by GISAXS. The full and dashed lines are best fits to the models of, respectively, hollow particles and core-shell particles with silica core and titania shell.

In all cases the fit to the hollow particle model (full line) is reasonable, showing that our model is applicable to the study of inorganic hollow nanoparticles. The mismatch in the very low q range is evident. This arises from the presence of weak ordering of HNPs, while only the disordered case is considered in our model. Fortunately, the deviation at low q does not affect the accuracy of the main parameters derived, i.e. the outer and inner radii and polydispersity. It should be noted that in DA, the polydispersity is taken into account only for

the form factor, while its effect on the structure factor is neglected. The error due to this approximation will increase with increasing polydispersity.^[52]

It is also worth noting that the parameters for HNP50 obtained by SAXS and GISAXS are very similar (see Table 3.1), the only significant difference being the volume fraction, as expected. This gives us reassurance that our simplified treatment of GISAXS pattern is adequate. Therefore, we are justified in applying the same treatment to the GISAXS pattern of HNP100.

To further demonstrate that the nanoparticles used in our work were indeed hollow, a core-shell model with silica electron density in the core, titania electron density in the shell and 0 outside was used to fit to the experimental SAXS curves. The electron density of silica and titania in the core-shell model were 661 e nm^{-3} and 1088 e nm^{-3} , respectively. The best fits to the experimental curves using the core-shell model are added in Figures 3.4a and c (dashed line). As can be seen, the fits are significantly poorer than those for the hollow particle model. The difference between the shapes of the full and dashed curves in Figures 3.4a, c also illustrate the high sensitivity of the SAXS method to the material difference between the core and shell.

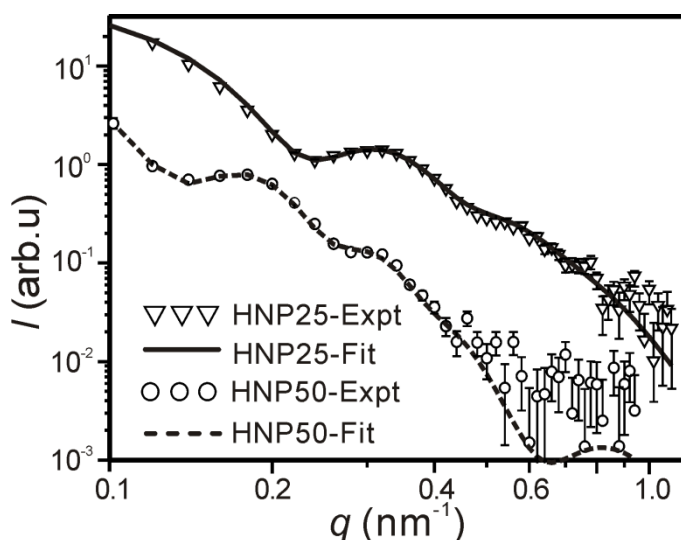


Figure 3.5 Experimental and fitted SANS curves for water dispersions (~ 3 wt%) of HNP25 and HNP50. Convolution with an instrumental broadening function was applied to the fitted curves.

While experimental broadening of scattering curves is negligible in the case of synchrotron SAXS and GISAXS, it is not negligible in SANS. Thus convolution with a Gaussian smearing function was applied before fitting it to the experimental curve. The width of the smearing function was taken from the documented data for the LOQ station at ISIS.^[131] For details see Section 2.3.2 in Chapter 2. Figure 3.5 shows a good fit of the SANS data, except in the high q range where the experimental signal to noise ratio is very low.

Table 3.1 HNP size and distribution characterized by different techniques

Sample	Method	Outer diameter (nm)	Inner diameter (nm)	Shell thickness (nm)	Stand. dev. of outer diameter (σ)	Volume fraction
HNP25	SAXS	30.0 \pm 0.5	20.8 \pm 0.5	4.6	15 \pm 2%	0.05 \pm 0.05
	SANS	29.0 \pm 0.5	20.6 \pm 0.5	4.2	17 \pm 2%	0.02 \pm 0.02
	TEM	26 \pm 5	15 \pm 5	5.5	12 \pm 2%	—
	DLS	28 \pm 2	—	—	20 \pm 2%	—
	N ₂ -ads/des	—	15.9 \pm 0.4	—	—	—
HNP50	SAXS	62.8 \pm 0.5	41.4 \pm 0.5	10.7	9 \pm 2%	0.05 \pm 0.05
	SANS	57.2 \pm 0.5	37.8 \pm 0.5	9.7	11 \pm 2%	0.02 \pm 0.02
	GISAXS	62.0 \pm 0.5	42.0 \pm 0.5	10.0	10 \pm 2%	0.45 \pm 0.05
	TEM	59 \pm 5	37 \pm 5	11	8 \pm 2%	—
	DLS	57 \pm 2	—	—	16 \pm 2%	—
	N ₂ -ads/des	—	34 \pm 1	—	—	—
HNP100	GISAXS	101.4 \pm 0.5	67.0 \pm 0.5	17.2	11 \pm 2%	0.40 \pm 0.05
	TEM	105 \pm 5	64 \pm 5	20.5	7 \pm 2%	—
	DLS	108 \pm 2	—	—	12 \pm 2%	—
	N ₂ -ads/des	—	67 \pm 4	—	—	—

The SAXS, GISAXS and SANS fitting parameters, i.e. the outer diameter, inner diameter, and polydispersity expressed as standard deviation of the Schulz distribution, are listed in Table 3.1. The Schulz size distributions best matching our SAXS/GISAXS data are plotted together with those from TEM and DLS results in Figure 3.3.

Nitrogen adsorption and desorption isotherms were also recorded for HNP25, HNP50 and HNP100 to characterize the pore volume distribution (obtained using Equation 2.20) and, crucially, the porosity of the HNP shell. According to the study by Blas and co-workers^[167], isotherms such as those in Figure 3.6a, can be interpreted by dividing them roughly into four stages: (1) for $p/p_0 < 0.2$ monolayer-multilayer adsorption takes place on all surfaces, i.e. those of inner cavities, outside particle walls and intrashell pore walls; (2) at $0.2 < p/p_0 < 0.5$ intrawall pores are filled with the condensate, followed at $0.5 < p/p_0 < 0.8$ by continuing layer-by-layer adsorption on the walls of the inner cavities and on the outside walls of HNPs; (3) around $0.8 < p/p_0 < 0.9$ the inner cavities, are filled with condensate – see the large increase in adsorbed volume in Figure 3.6a. Finally (4) the interparticle interstices are filled. In HNP50 and HNP100 the filling of the inner cavities appears to happen at a somewhat higher pressures. The desorption process at high and low pressures seems to be the inverse of the adsorption process. However, at intermediate pressures (roughly $0.5 < p/p_0 < 0.8$), desorption of the condensate from the inner cavities appears to be blocked by the condensate within the intrawall pores. This blocking effect is thought to cause hysteresis of the isotherms. As the vapour pressure decreases, once the intrawall cavities are unblocked the delayed evaporation of the condensate in the inner cavities takes place.^[134] A sudden drop of the adsorbed volume occurs at this point, e.g. at $p/p_0 = 0.5$ for HNP100. To obtain the pore volume distribution, Equation 2.18, 2.19 and 2.20 are used. The adsorption isotherms will be analyzed in more detail in the next section.

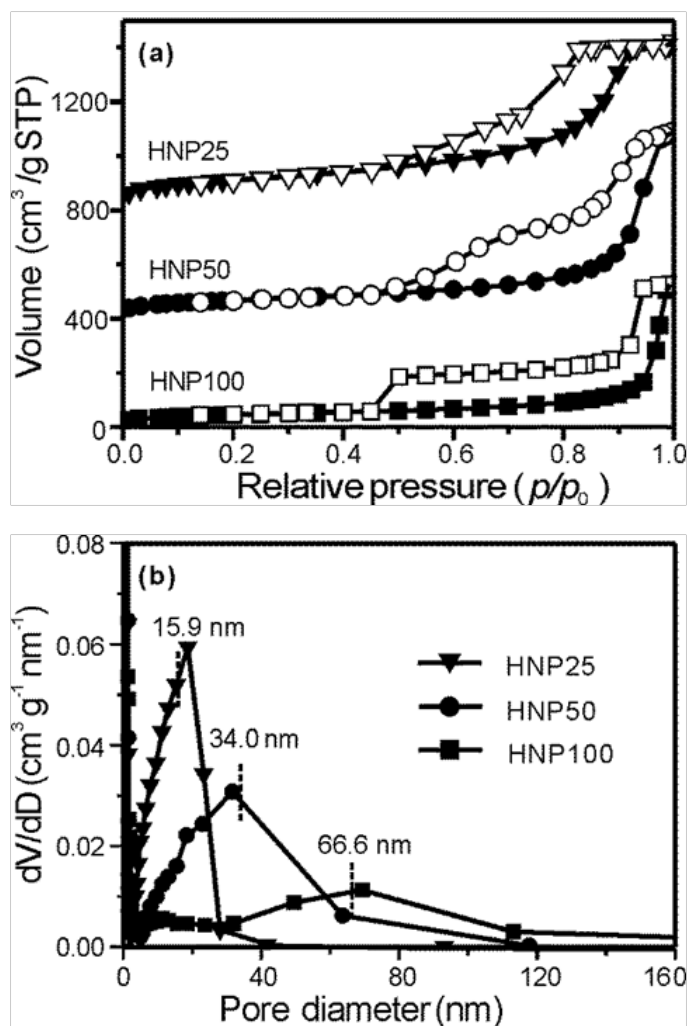


Figure 3.6 (a) Nitrogen adsorption/desorption isotherms of HNP25, HNP50, and HNP100. Solid symbols: adsorption, open symbols: desorption. The curves are displaced vertically by $400 \text{ cm}^3/\text{g STP}$ for clarity. Here, STP means standard temperature and pressure, i.e. 273 K and 1 atm pressure, respectively. (b) Pore volume distribution derived from the adsorption isotherms in (a) using the spherical pore model. The data in (a) was supplied by Chanhui Kim and Sun Hye Hwang.

The results from SAXS, SANS, GISAXS, TEM, DLS and N_2 adsorption-desorption isotherms are summarized in Table 3.1. As can be seen, generally reasonable agreement is achieved between different methods. Comparing the results from X-ray and neutron scattering, good agreement is obtained, which is perhaps not surprising considering that the same theoretical model is used in the analysis of the scattering curves.

A comparison between SAXS-GISAXS and TEM shows again reasonable agreement generally in the parameters obtained. An obvious discrepancy between SAXS and TEM

results is in the degree of polydispersity, with TEM consistently giving somewhat lower values of σ . Because the value of σ is in principle affected by the experimental resolution in scattering methods but not in TEM, one may be tempted to attribute the increased σ in SAXS to poor resolution. However, the instrumental smearing of synchrotron SAXS and GISAXS is negligible compared to the fluctuation wavelength of the form factor. A more likely explanation is that scattering functions are susceptible to possible weak particle clustering that had not been filtered out by deconvolution with the PY structure factor. Another possible contributing factor may be the choice of TEM images for analysis which may be affected by human judgment favoring clean patches, whereas X-rays and neutrons average over the entire sample.

The values for the outer diameter of HNPs obtained from DLS are also in broad agreement with those of SAXS and TEM, but here the discrepancies are somewhat larger. The deviations, of the order of 7%, are both positive and negative. Furthermore, the polydispersity values indicated by DLS are higher than those from other methods. In fact, as seen in Figures 3.3b, d, f, the size distribution from DLS is rather asymmetric with a tail on the large-diameter side. Again, this is likely to be the result of clustering of HNPs. DLS is not able to recognize and remove from counting spatially correlated particle clusters as effectively as the SAXS/SANS method applied here, even less so compared to TEM where clusters are ignored by the experimentalist's choice.

Turning to the gas adsorption results, the inner diameters from N_2 isotherms are consistent with those from X-ray and neutron scattering methods, with less than 25% difference for HNP25 and HNP50, and a nearly perfect match for HNP100. This shows that the spherical pore model used is suitable for HNPs.

3.4.2 Shell Porosity and Size of Intrawall Pores

The main advantage of using gas isotherms in the study of HNPs is that data can be obtained on the size of intrawall pores and the porosity of the particle shell, information that is not available from other methods evaluated in this study.

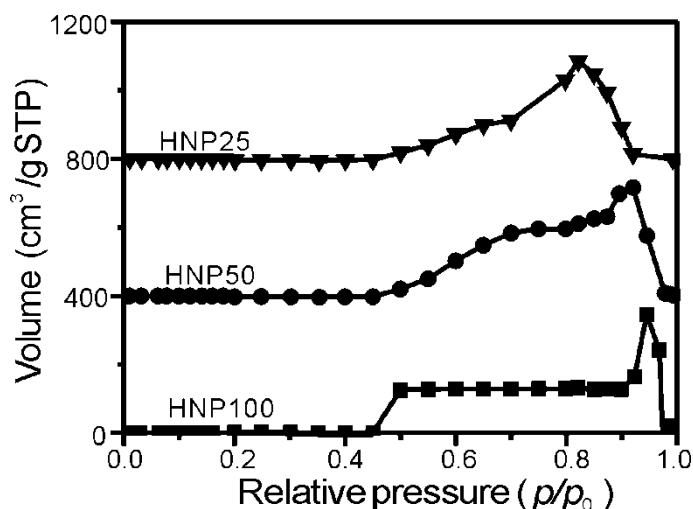


Figure 3.7 The difference in N_2 volumes adsorbed and desorbed as a function of relative pressure. The curves are vertically shifted by $400 \text{ cm}^3/\text{g STP}$ for clarity.

It is interesting to examine the difference in N_2 desorption/adsorption isotherms for the three samples studied, as shown in Figure 3.7. In HNP100, a plateau is clearly seen for relative pressures between 0.5 and 0.9. As mentioned above, this is attributed to the fact that during desorption the evaporation of the liquid in the inner cavities is blocked by the filled intrawall pores. When the condensate in the intrawall pores evaporates, the liquid inside the inner cavity is expelled quickly. Figure 3.7 also shows an additional smaller hysteresis at $p/p_0 > 0.9$ for HNP100, believed to be caused by nonequilibrium adsorption/desorption at the outer surfaces, i.e. interparticle interstices.

For HNP25 and HNP50, the ending of the plateau at its low-pressure side is more gradual, and shifted to somewhat higher pressure. The reason for the shift is probably the thinner shell of these HNPs; the condensate in the shorter intrawall pores are likely to requiring less overpressure from the inner cavity to be expelled in the desorption cycle. It is also evident that as the size of the particle decreases, the peak arising from the adsorption/desorption on interparticle interstices shifts to lower relative pressure; again this is not entirely unexpected in view of the smaller size of the interstices.

The height of the plateau should correspond to the specific volume of the inner cavities. For HNP100, this is found to be $0.197 \text{ cm}^3/\text{g}$ at $p/p_0 = 0.55$. This value, in fact gives us an

opportunity to estimate the porosity x of the shell, i.e. the fraction of shell volume occupied by the micropores. The procedure is described in the following.

The molar ratio of titania and silica in the HNPs is found to be 52:48 from energy-dispersive X-ray spectroscopy. Therefore, the density $\rho_{\text{SiO}_2/\text{TiO}_2}$ of the $\text{SiO}_2/\text{TiO}_2$ is estimated to be 3.0 g/cm^3 (2.2 g/cm^3 for amorphous silica and 3.8 g/cm^3 for amorphous titania). The “bulk” density of the shell, including the micropores, is then $(1-x) \rho_{\text{SiO}_2/\text{TiO}_2}$. Taking the outer and inner diameters from SAXS/GISAXS, and the specific volume of the inner cavities V_{inner} from the step height in the N_2 desorption isotherm, one can obtain the shell porosity x via the relation:

$$V_{\text{inner}} = 1/[(1-x) \cdot \rho_{\text{SiO}_2/\text{TiO}_2}] \cdot r_0^3 / (R_0^3 - r_0^3) \quad (3.10)$$

From the above equation, x of HNP100 is found to be 0.31.

For HNP50 or HNP25, the plateau is less well defined and the result of the above method is less reliable. For HNP50, if we take V_{inner} to be $0.28 \text{ cm}^3/\text{g}$, the value at $p/p_0 = 0.70$, the estimated shell porosity is 0.48 according to Equation 3.10. Here the hysteresis from external interstices may contribute somewhat to the height of the downward step in desorbed volume, leading to an overestimate in V_{inner} . For HNP25 the uncertainty in determining V_{inner} , and thus x , is even larger.

The above data show that clear-cut adsorption/desorption stages, i.e. filling of intrawall pores, then inner cavities, followed by interparticle interstices, can only be observed for HNP100, but are less distinct in HNP50 and HNP25. Generally it is to be expected that the four stages will be less distinct in smaller HNPs where the difference between the inner cavity and interstices on the one hand, and the intrawall pores on the other, is smaller. We note that in the original work of Blas and co-workers^[167] the HNPs are around 100 nm in diameter.

For HNP100, the intrawall pores are found to evaporate together with the inner cavities at relative pressure around 0.48; in fact for HNP25 and HNP50 the onset point seems to be also around this value. This pressure corresponds to a t -thickness of 0.6 nm (Equation 2.18), and a Kelvin radius of 1.3 nm (Equation 2.19). Since $r_p = r_K + t$, this suggests an average diameter of intrawall pores of 3.8 nm.

In addition to this crude estimate, we now use an alternative way of determining the size of intrawall pores from the measured surface area. In this study, BET method was used at low relative pressures ($p/p_0 \leq 0.2$) to probe the total surface area of the HNPs (Figure 3.8a). From the fitting parameters the specific surface area (A_{BET}) was calculated and is listed in Table 3.2. Also listed are values of A_{shell} , the specific surface area of the shell without any intrawall pores, including only the inner and outer surfaces, which is calculated from SAXS data using

$$A_{\text{shell}} = 3 V_{\text{SiO}_2/\text{TiO}_2} \cdot (R_0^2 + r_0^2)/(R_0^3 - r_0^3) \quad (3.11)$$

Here $V_{\text{SiO}_2/\text{TiO}_2} = 1/\rho_{\text{SiO}_2/\text{TiO}_2} = 0.333 \text{ cm}^3/\text{g}$ is the specific volume of amorphous $\text{TiO}_2/\text{SiO}_2$.

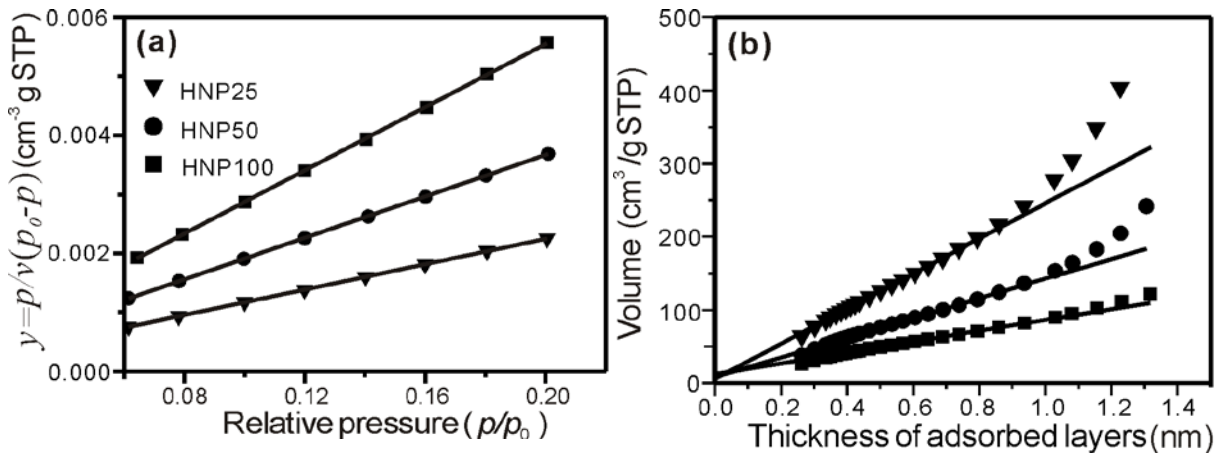


Figure 3.8. (a) BET linear fit for specific surface area, and (b) t -curve and straight line fit in t -plot method.

Table 3.2 Surface area of the HNPs measured by t -plot ($A_{t\text{-plot}}$) and BET methods (A_{BET}), the contribution from the inner and outer shell surface (A_{shell}), and intrawall pores ($A_{\text{IWP}} = A_{\text{BET}} - A_{\text{shell}}$). The estimated diameter of intrawall pores D_{IWP} assuming a shell porosity $x = 0.31$, and the estimated shell porosity x assuming $D_{\text{IWP}} = 3.8 \text{ nm}$.

Sample	$A_{t\text{-plot}}$ (m^2/g)	A_{BET} (m^2/g)	A_{shell} (m^2/g)	A_{IWP} (m^2/g)	D_{IWP} (nm) ($x = 0.31$)	Shell porosity x ($D_{\text{IWP}} = 3.8 \text{ nm}$)
HNP25	360 ± 20	400 ± 20	220 ± 2	180 ± 20	3.5 ± 0.5	0.33 ± 0.03
HNP50	200 ± 20	250 ± 20	70 ± 1	180 ± 20	3.5 ± 0.5	0.33 ± 0.03
HNP100	110 ± 20	160 ± 20	40 ± 1	120 ± 20	5.1 ± 0.8	0.25 ± 0.04

In Table 3.2, the specific surface areas, both A_{BET} and A_{shell} , are seen to decrease as the particles size increases, as expected. However, there is a large discrepancy between A_{shell} and A_{BET} , which we attribute to the small pores in the shells of the HNPs. Now as the porosity of the shell is x , the ratio between the volume of material in the shell and the total volume of HNPs is given by

$$\begin{aligned} V_{\text{SiO}_2/\text{TiO}_2}/V_{\text{total}} &= V_{\text{SiO}_2/\text{TiO}_2}/(V_{\text{SiO}_2/\text{TiO}_2} + V_{\text{IWP}} + V_{\text{inner}}) \\ &= (1-x)(R_0^3 - r_0^3)/R_0^3 \end{aligned} \quad (3.12)$$

For each HNP, the volume of intrawall pores is $x \cdot 4/3 \cdot (R_0^3 - r_0^3)$, and by defining the average diameter of the cylindrical intrawall pores as D_{IWP} , the surface area contribution from intrawall pores is then $[x \cdot 4\pi/3 \cdot (R_0^3 - r_0^3)]/(D_{\text{IWP}}/4) = 16\pi/3 \cdot x(R_0^3 - r_0^3)/D_{\text{IWP}}$. So the total surface area of each HNP

$$\begin{aligned} A_{\text{HNP}} &= (16\pi/3)x(R_0^3 - r_0^3)/D_{\text{IWP}} + 4\pi(1-x)(R_0^2 + r_0^2) \\ &= [(16\pi/3)x(R_0^3 - r_0^3)/D_{\text{IWP}} + 4\pi(1-x)(R_0^2 + r_0^2)] \cdot [V_{\text{HNP}}/(4/3\pi R_0^3)] \end{aligned} \quad (3.13)$$

Here V_{HNP} is the total volume of a single hollow nanoparticle.

Hence the specific total surface area of HNPs, A_{total} , is given by

$$\begin{aligned} A_{\text{total}} &= [(16\pi/3)x(R_0^3 - r_0^3)/D_{\text{IWP}} + 4\pi(1-x)(R_0^2 + r_0^2)] \cdot V_{\text{SiO}_2/\text{TiO}_2}/[(4/3\pi)(1-x)(R_0^3 - r_0^3)] \\ &= [4x/(1-x)/D_{\text{IWP}} + 3(R_0^2 + r_0^2)/(R_0^3 - r_0^3)] \cdot V_{\text{SiO}_2/\text{TiO}_2} \\ &= [V_{\text{SiO}_2/\text{TiO}_2}/(1-x)] \cdot x/(D_{\text{IWP}}/4) + A_{\text{shell}} \end{aligned} \quad (3.14)$$

Therefore, the extra contribution to the surface area from intrawall pores is

$$\begin{aligned} A_{\text{IWP}} &= [V_{\text{SiO}_2/\text{TiO}_2}/(1-x)] \cdot x/(D_{\text{IWP}}/4) \\ &= 1.332 \text{ cm}^3/\text{g} \cdot x/[(1-x) D_{\text{IWP}}] \end{aligned} \quad (3.15)$$

The above equation in fact suggests that if the porosity of the shell x and the size of intrawall pores D_{IWP} for different samples are the same, then the specific (per unit weight) extra surface area contributed by the intrawall pores, A_{IWP} , will also be the same. As is shown in Table 3.2,

A_{IWP} values for the three samples are indeed fairly similar. The estimated diameters of intrawall pores assuming a porosity of 0.31 (as derived for HNP100 above), and estimated porosity x assuming $D_{IWP} = 3.8$ nm, are calculated and listed in Table 3.2. The resulting porosity between 0.25 and 0.33, and intrawall pore diameter between 3.5 nm and 5.1 nm, seems fairly reasonable. Wang and Zeng^[146] give a D_{IWP} range of 3.6 – 3.8 nm.

The t -plot method has also been tested on the present HNP systems and the results are included in Table 3.2. The linear portion of the t -plots was in the relative pressure region from 0.2 to 0.65, corresponding to layer thicknesses t between 0.45 and 0.8 nm. Like BET, the t -plot method shows a decrease in $A_{t\text{-plot}}$ with increasing particle size, as expected.^[168] For the t -plot method to be applicable, the linear range must ideally be in the pressure range where no new surface is becoming covered, i.e. where all small pores had been already filled and are out of the equation. If this was the case in our systems, then $A_{t\text{-plot}}$ would have been similar to A_{shell} . However, the area $A_{t\text{-plot}}$, obtained from the slope of the adsorbed volume versus adsorbed layer thickness t , is significantly larger, and is closer to A_{BET} . This suggests that as pressure was increasing during the gas adsorption experiment, condensation in micropores was contributing to the adsorbed volume. Thus our systems are not suitable for the surface area determination by the t -plot method, since the intrawall pores and the central cavities are not separated in size sufficiently.

Based on the above results on porosity and the size of intrawall pores, a to-scale illustration of a 50 nm HNP with porosity 0.3 and an average diameter of intrawall pores of 3.5 nm is shown in Figure 3.9.

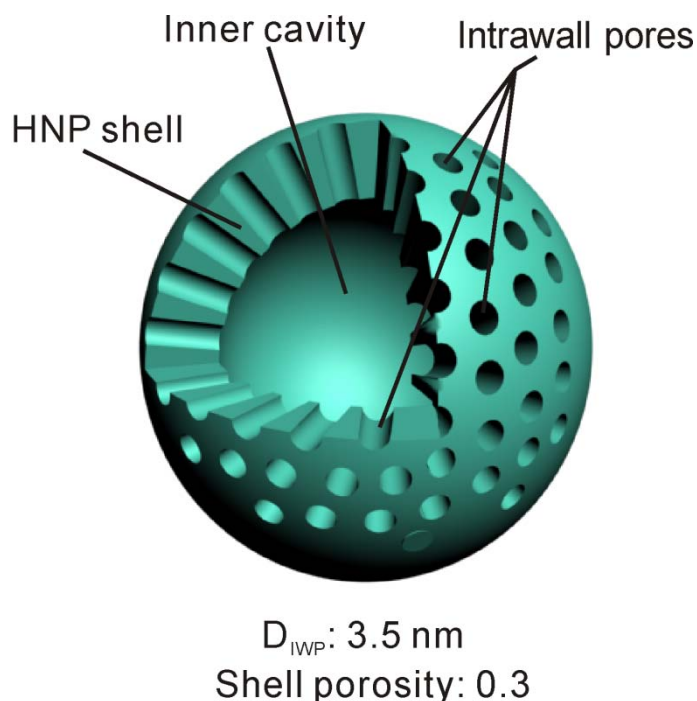


Figure 3.9. A depiction of a hollow nanoparticle of 50 nm outer diameter showing the calculated shell porosity (0.3) and size (3.5 nm) of intrawall pores. The dimension and number of micropores are to scale, assuming uniform cylindrical pores.

3.5 Conclusions

The HNPs used in this study, due to their size and shape uniformity, provide very convenient systems on which different morphology characterization methods can be rigorously tested against theory. The results show that SAXS/GISAXS, using synchrotron radiation, give accurate information on the inner diameter, outer diameter and size distribution. SANS gives essentially the same information after performing correction for instrumental broadening. The results from SAXS and GISAXS justify the use of the hollow sphere model applying the decoupling and Percus-Yevick approximations. The theoretical scattering curves presented can be used directly for qualitative evaluation of experimental data.

TEM itself is likely to overestimate the shell thickness, unless high-resolution (HRTEM) is used, and may underestimate the polydispersity of the particles if sampling is not performed with great care. DLS measurements are quicker and perhaps cheaper than SAXS, but are less

reliable in determining polydispersity, giving higher values than SAXS. Also they give no information on the inner diameter and shell thickness. N₂ adsorption-desorption isotherms can estimate fairly accurately the diameter and specific volume of the inner cavity. In addition, combination of the adsorption methods with scattering techniques, uniquely provide information on intrawall pore size and shell porosity, which are key parameters for application of HNPs in drug delivery and catalysis. The high porosity (30%) of the shell and the relatively large intrawall pores (~4 nm diameter) are to be taken into account when considering the mechanism of solvent and drug diffusion in drug delivery applications of HNPs.

CHAPTER 4 Morphology of Polymer-Embedded Hollow Nanoparticles

Abstract

In the first part of this chapter, new batches of SiO₂/TiO₂ hollow nanoparticles (HNPs) with diameter ranging from 25 nm to 100 nm were prepared. The morphology of newly prepared HNPs was characterized by SAXS, based on the decoupling and the Percus-Yevick approximations, as well as the hollow sphere model used in last chapter. Size information on HNPs was extracted, including average outer diameter, average inner diameter, and polydispersity. Application of an alternative form factor based on hollow ellipsoids, and of a sticky hard sphere structure factor, did not improve the fit significantly. Then, the above HNPs were supported on porous poly(ethylene oxide) (PEO) scaffold by freeze drying from aqueous solution. To characterize the product, a multi-shell model was applied to fit the experimental SAXS curves and extract the following morphological information: distribution of HNPs between the surface and interior of the polymer, thickness of the polymer layers lining the outer and the inner surface of HNPs, and the densities of the outer and inner polymer layers. The work demonstrates the versatility of SAXS in obtaining key information on dissolved and on polymer-supported HNPs in applications such as drug delivery and catalysis.

KEYWORDS: Small-Angle X-ray Scattering, Hollow Triple Shell-Sphere Model, Freeze Drying Technique, Polymer-Embedded Hollow Nanoparticles, Morphology.

*Chen, Z. H., Hwang, S. H., Zeng, X., Roh, J., Jang, J. & Ungar, G. *J. Appl. Cryst.* 2013, **46**, 1654-1664.

4.1 Introduction

Hollow nanoparticles (HNPs) have been widely studied for their applications as drug delivery vehicles and as catalyst supports. In this chapter we describe the use of SAXS to achieve two objectives: (i) to characterize the morphology of the HNPs, and (ii) to characterize HNP distribution in porous polymer gels. The latter (ii) is of interest in its own right due to the applications of polymer-supported HNP catalysts and drug release agents, but also because HNPs can be used as SAXS markers in *in-situ* monitoring of solvent diffusion to and into a polymer gel.

Freeze dried gels are another type of important drug delivery vehicles and they have attracted much attention over the years. In acidic fluids, *e.g.* gastric fluid, they can swell to tens of times their original weight and release the drug efficiently.^[169] Freeze dried hydrogels can release the drug much more efficiently than an ordinary air dried hydrogel.^[170] Swelling speed and swelling ratio of the hydrogel in different fluids, affected by ionic strength, pH etc., have been found to be a key determinant of drug delivery performance.^[169, 171] However, measurements of hydrogel swelling have only been done *ex-situ*. Developing an *in-situ* method is therefore desirable.

Here, we describe the use of SAXS to characterize the morphology of HNPs, including outer and inner diameter, and polydispersity. To understand the interaction between the fluid and the freeze dried hydrogel, we specially prepare several freeze dried HNP-poly(ethylene oxide) (PEO) systems as models for testing our SAXS analysis of heterogeneous supported HNPs, and to prepare the ground for developing an *in-situ* method for monitoring fluid diffusion. Furthermore, we propose to use ceramic HNPs as indicators for the diffusion of fluid into freeze-dried polymer scaffold. As the HNPs are not only deposited at the surface, but are also embedded within the interior of the polymer, they can serve as SAXS markers in *in-situ* studies of solvent diffusion both to the polymer and through the polymer in the porous gel. In this work, the morphology and the distribution of HNPs after freeze drying in PEO are characterized by using a new realistic SAXS model.

4.2 Experimental Section

4.2.1 Materials

The sample preparation method for HNPs and PEO-embedded HNPs has been described in Section 2.1 of Chapter 2, and no more details are explained here.

In this chapter, three different HNPs were prepared, and they were labeled as HNP25, HNP50B and HNP100B according to their nominal outer diameter, i.e. 25 nm, 50 nm, and 100 nm, respectively. The letter “B” was used here to indicate the samples were from different batches compared to those used in Chapter 3.

Samples of HNP25, HNP50B and HNP100B freeze dried in PEO are labelled HNP25-PEO, HNP50B-PEO and HNP100B-PEO, respectively.

4.2.2 Methods

SAXS experiments were performed on beamline I22, Diamond Light Source, UK. To characterize the morphology of HNPs, the particles were dispersed in water in an ultrasonic bath. SAXS curves were recorded from dilute suspensions of the HNPs held in 1.0 mm X-ray capillaries. SAXS data were also collected from HNPs embedded in freeze-dried polymer as prepared in capillaries. Prior to data analysis, background was subtracted arising from the capillary and the porous polymer (in the case of freeze dried samples). For this purpose a capillary with freeze dried PEO was prepared containing no nanoparticles. Background subtraction was carried out after appropriate scaling. Absolute SAXS intensity was not measured because of the inaccuracy in determining the mass (volume) of the highly porous and inhomogeneous irradiated material. Other details of the SAXS experiments and raw data reduction can be found in Section 2.2.1.2 and Section 2.3.1 of Chapter 2, respectively.

TEM images were obtained with the same machine and the same sample preparation method as those used in Chapter 3. A JEOL 6700 SEM, working at 10 kV, was used for imaging the freeze-dried samples. The TEM and SEM images were supplied by Sun Hye Hwang and Jongmin Roh.

4.3 Theoretical Model for Small Angle X-ray Scattering

To simulate the SAXS intensity function, the decoupling approximation (DA) ^[51] is used again. SAXS intensity within DA can be expressed by

$$I(q) = \langle |F(q)|^2 \rangle + \langle |F(q)| \rangle^2 \cdot [S(q) - 1] \quad (4.1)$$

where q is the scattering vector $q = 4\pi \sin\theta/\lambda$ ($2\theta =$ scattering angle, $\lambda =$ X-ray wavelength), $\langle |F(q)|^2 \rangle$ is the form factor, and $S(q)$ is the structure factor.

In this chapter, we propose the hollow triple-shell sphere (HTSS) model with constant electron density in each region. The HTSS model can be used not only for hollow nanoparticles, but also for core-shell nanoparticles. Figure 4.1 shows the electron density profile of the HTSS model. R_1 , R_2 , R_3 and R_4 are, respectively, the inner radii of the first, second and third shell, and the outer radius of the third shell. ρ_0 , ρ_1 , ρ_2 , and ρ_3 are, respectively, the electron densities of the surrounding medium, and of the first, second and third shell. In this model, each parameter can be changed independently, which means that the model can be used for different kinds of nano- and colloidal particles. For example, if we force $R_1 = R_2$ and $R_3 = R_4$, the HTSS model will become a hollow single-shell sphere model and can be used directly for hollow nanoparticles. Additionally, if we kept the parameters of the middle shell constant, it would be possible to apply the hollow nanoparticle model to situation such as HNPs covered by an outer and an inner layer of another material.

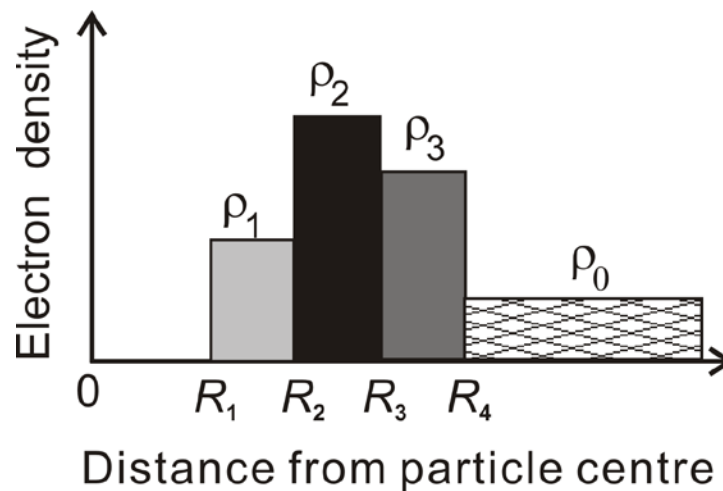


Figure 4.1 Illustration of the hollow triple-shell sphere model used in this study.

$F(q)$ for the HTSS is expressed by

$$\begin{aligned}
 F(q) = \frac{4\pi}{q^3} [& (\rho_3 - \rho_0)(\sin qR_4 - qR_4 \cos qR_4) \\
 & + (\rho_2 - \rho_3)(\sin qR_3 - qR_3 \cos qR_3) \\
 & + (\rho_1 - \rho_2)(\sin qR_2 - qR_2 \cos qR_2) \\
 & - \rho_1(\sin qR_1 - qR_1 \cos qR_1)]
 \end{aligned} \tag{4.2}$$

When the nanoparticles are polydisperse, the size distribution needs to be taken into account for the form factor. The form factor averaged over the size distribution of particles is presented again and expressed as

$$\langle |F(q)|^2 \rangle = \int_0^\infty |F(q)|^2 h(R) dR \tag{4.3}$$

$$\langle F(q) \rangle^2 = \left| \int_0^\infty F(q) h(R) dR \right|^2 \tag{4.4}$$

where $h(R)$ is the size distribution function of radius R . Here, R could be R_1 , R_2 , R_3 or R_4 . To simplify the calculation, the size distributions of R_1 , R_2 , R_3 and R_4 are all assumed to be the same. Schulz distribution function is used here again as the size distribution function. Details about Schulz distribution function can be found in the theory part of Chapter 3 (i.e. Section 3.3.1). In the following sections, we select R to be the outer radius of the nanoparticles, *i.e.* R_4 in Figure 4.1, and hence R_0 is the averaged outer radius of the nanoparticles. As is seen from Equation 4.2, $F(q)$ is a function of many trigonometric functions. Therefore, the form factor is an integral of trigonometric functions and it can be further expressed as the sum of integrals over each trigonometric function. Analytical expressions for the integral over different kinds of trigonometric functions have been summarized in a study by Förster and co-workers.^[165] Therefore, the analytical expression for the form factor can be derived without complex calculation.

The Percus and Yevick (PY) approximation is again used to calculate the structure factor $S(q)$ for a randomly disordered hard sphere system. Details of the expression of $S(q)$ within PY approximation can be found in the theory part of Chapter 3 (i.e. Section 3.3.1).

In the case when HNPs are not strictly spherical, the anisotropy of nanoparticles has to be taken into account. A hollow ellipsoid model is built based on the core-shell ellipsoid model proposed elsewhere.^[62, 172-174] The geometry of a hollow ellipsoid with respect to the X-ray beam is shown in Figure 4.2.

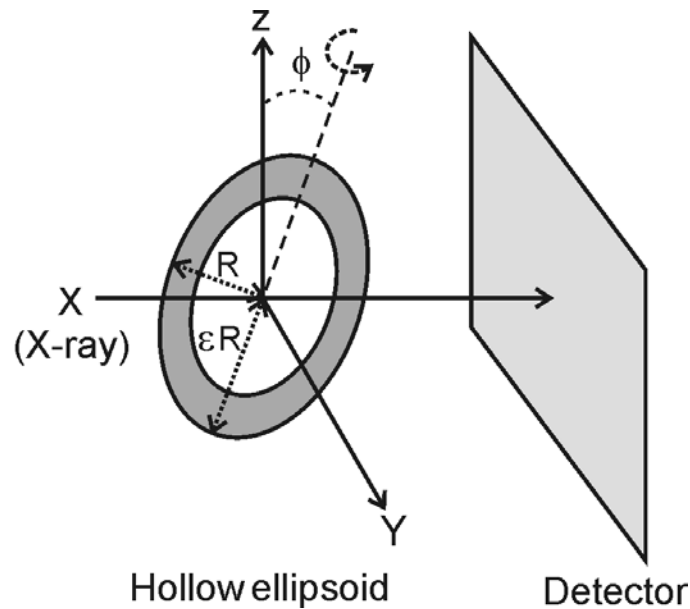


Figure 4.2 Geometry definition for scattering from a hollow ellipsoid

We consider only ellipsoids with uniaxial (C_{∞}) symmetry. In Figure 4.2, such a hollow ellipsoid with outer semi-axes R and εR , inner semi-axes βR and $\varepsilon \beta R$, and orientation angle ϕ is defined. Here, ε and β are the axial ratio of an ellipsoid, and the ratio between the inner and outer radii, respectively. ϕ is the angle between the symmetry axis of the hollow ellipsoid and the Z axis. For simplicity, some assumptions are made for the hollow ellipsoid model. Firstly, the inner axial ratio ε is assumed to be the same as the outer one. For a system with majority of HNPs nearly spherical, the assumption is acceptable since the difference between the inner axial ratio and the outer axial ratio could be very small. Secondly, the ratio between the equatorial axes of the inner and outer ellipsoid, β , is assumed to be constant for all hollow ellipsoids. Thus the polydispersity of the hollow ellipsoids will be defined by only one parameter, σ , i.e. the fluctuation in outer semi-axis R . Thirdly, the orientation of the hollow ellipsoids is assumed to be random, since there is only weak interaction between the nanoparticles.

Based on the core-shell ellipsoid model given in literature ^[172-174] and in a program by Kline ^[62], the analytical expression for the scattering amplitude factor $F(q)$ of a hollow ellipsoid with a given orientation ϕ can be written as

$$F(q) = \frac{\Delta\rho \cdot 4\pi\varepsilon}{(qy)^3} \cdot [\sin(qRy) - qRy \cdot \cos(qRy) - \sin(q\beta Ry) + q\beta Ry \cdot \cos(q\beta Ry)] \quad (4.5)$$

where $\Delta\rho$ is the difference between the electron density of the shell and of the surrounding medium, ε is the axial ratio of the ellipsoid defined above, and $y = (\sin^2\phi + \varepsilon^2 \cos^2\phi)^{1/2}$ is a term related to the orientation.

For a nanoparticle system with random orientations, integration has to be performed over all orientation angles, ^[172] giving

$$\langle F^n(q) \rangle_{angle} = \int_0^{\pi/2} F^n(q) \cdot \sin\phi d\phi \quad (4.6)$$

where $n = 1$ or 2 according to the decoupling approximation and the angular brackets mean the average over all the orientation angles. When the polydispersity of hollow nanoparticles is further considered, the expression for scattering intensity can be written as

$$I(q) = \int_0^\infty h(R) \langle F^2(q) \rangle_{angle} dR + \left(\int_0^\infty h(R) \langle F(q) \rangle_{angle} dR \right)^2 \cdot (S(q) - 1) \quad (4.7)$$

Here we still use the decoupling approximation for hollow ellipsoids since the size distribution of nanoparticles is narrow. ^[172, 175] The hard sphere structure factor with PY approximation is used for the ellipsoids, assuming that the interparticle interaction of ellipsoids obeys the same hard body interaction as for the spheres, and that the interaction radius of the ellipsoids takes the same as that for hard spheres with the same volume.

Based on the DA and PY approximations, SAXS intensity functions for HNPs and freeze dried HNPs in PEO were calculated, and morphological parameters were extracted by fitting to experimental data. C programs were written for the fit. The best fit was determined by searching the minimum value of the reduced χ^2 , which indicates the degree of disagreement between the experimental and calculated intensity.

4.4 Results and Discussion

In Section 4.4.1, the SAXS study of the dimensions of HNP25, HNP50B, and HNP100B is described, since the HNP50B and HNP100B were prepared from batches different from those used in Chapter 3. In Section 4.4.2, the analysis of HNPs freeze dried in PEO as model system is described. A complex model was proposed for the analysis of SAXS intensity. Using this model, the morphology of the HNP-PEO composites obtained by freeze drying is determined. Finally, morphological details of the HNP25-PEO, HNP50B-PEO, and HNP100B-PEO systems are compared and discussed.

4.4.1 Sizes of Hollow Nanoparticles

The TEM image of HNPs is shown again by taking HNP50B as an example, since the samples were from a new batch. As can be seen in Figure 4.3 for TEM image of HNPs, majority of HNPs are nearly spherical in shape, with a spherical central cavity, while relatively few HNPs are ellipsoidal.

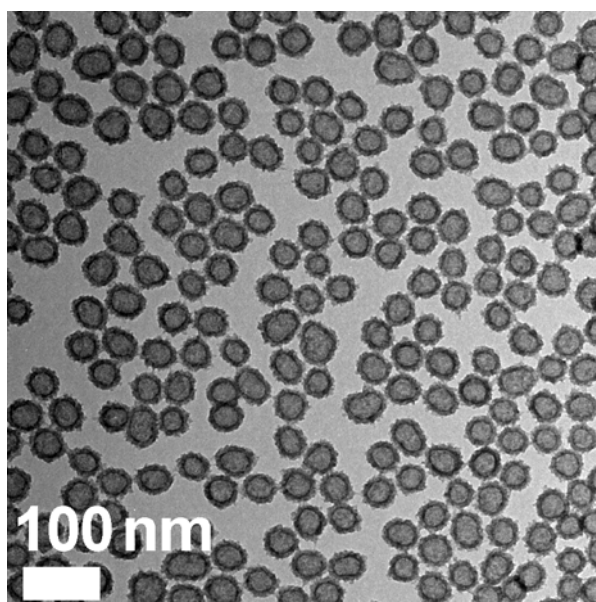


Figure 4.3 TEM image of as prepared HNPs. TEM image was supplied by Sun Hye Hwang and Jongmin Roh.

HNPs with well defined geometry, dispersed in water, were further studied by SAXS to characterize their sizes. As is mentioned in the SAXS theory section, the HTSS model can be applied to hollow nanoparticles if the thicknesses of the first and third shells are both 0. The theoretical SAXS intensity of HNPs was then calculated for this simple hollow sphere model. For comparison, a complex hollow ellipsoid model was also used to determine both polydispersity and anisotropy of the HNPs. The calculated SAXS intensity curves from both the hollow sphere and hollow ellipsoid model were fitted to the experimental ones. The experimental and fitted SAXS curves are shown in Figure 4.4 for all three kinds of HNP.

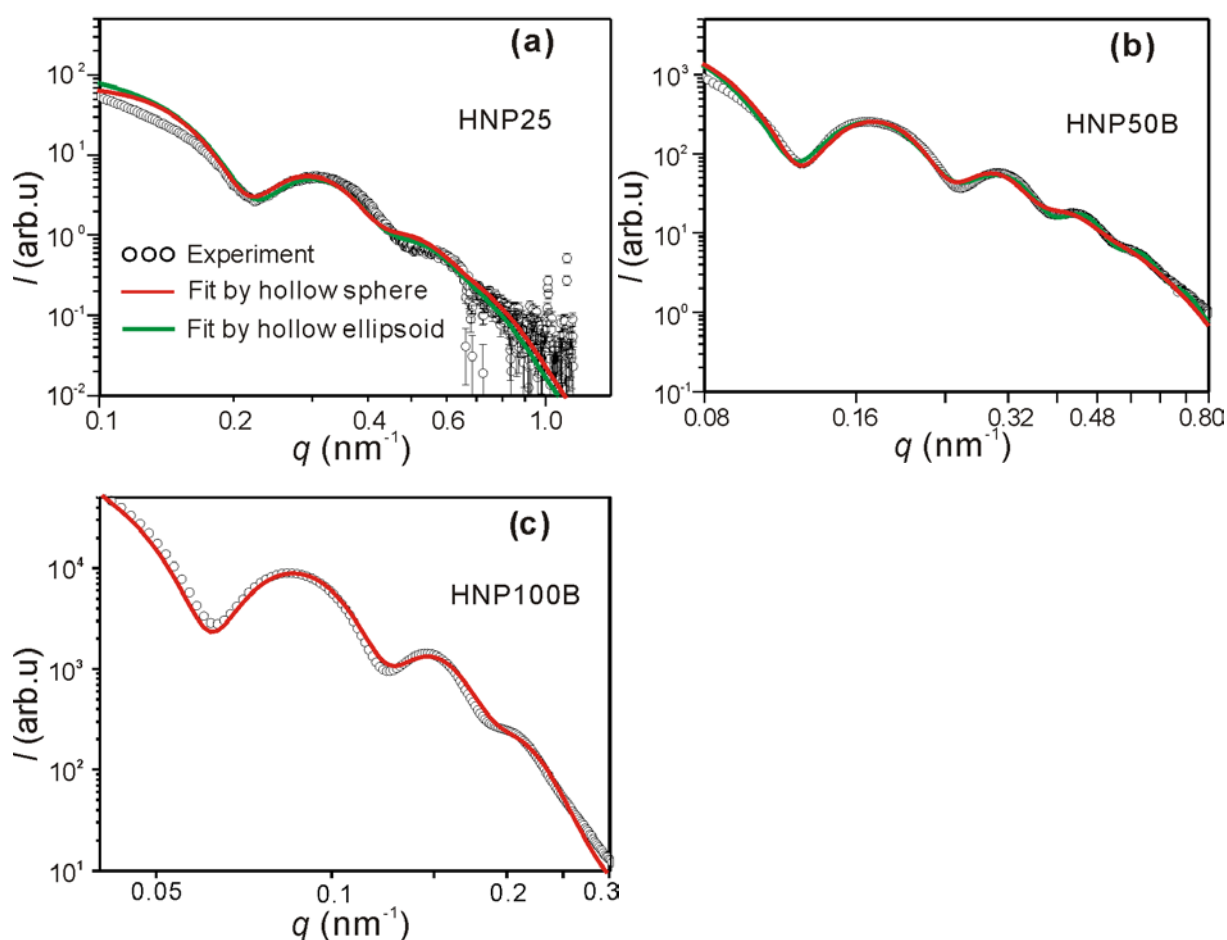


Figure 4.4 Experimental and fitted SAXS curves using hollow sphere (red line) and hollow ellipsoid (green line) models for water dispersions of (a) HNP25 (5 wt%), (b) HNP50B (5 wt%), and (c) HNP100B (2 wt%). In (b) the two lines are barely distinguishable, and in (c) completely indistinguishable.

In all cases using the hollow sphere model, the fit results are reasonable, showing that the hollow sphere model is applicable for inorganic hollow nanoparticles. The hollow ellipsoid model generally gives a similar fit quality. Only for HNP50B, the hollow ellipsoid model gives a somewhat better fit at high q , i.e. at the 2nd and 3rd peaks. For both hollow sphere and ellipsoid models there is some discrepancy between the calculated and experimental curves at low q . This may be due to incomplete particle separation during sonication. However, since we are more interested in the middle q range which contains the morphological information, the deviation at low q is less important. We also tried other structure factors, i.e. the sticky hard sphere model of Baxter and others,^[109, 110, 176] to tackle the deviation in the low q range. However, the sticky hard sphere model did not result in a significant improvement.

Table 4.1 SAXS fitting results for HNPs using the hollow sphere model and hollow ellipsoid model

Sample	Model	Outer diameter (nm) (± 0.5)	Inner diameter (nm) (± 0.5)	Axial ratio ε (± 0.01)	Stand. dev. of outer diameter (σ) ($\pm 2\%$)*	Packing density (± 0.02)	χ^2
HNP25	Ellipsoid	30.0	20.8	1.04	15%	0.01	25.14
	Sphere	30.0	20.8	-	15%	0.05	24.98
HNP50B	Ellipsoid	51.0	40.3	1.39	5%	0	8.21
	Sphere	54.0	42.2	-	11%	0.05	18.35
HNP100B	Ellipsoid	115.8	75.8	1.00	10%	0.03	40.05
	Sphere	115.8	75.8	-	10%	0.03	40.05

* Here the standard deviation of outer diameter refers to polydispersity of outer diameter. The indicated error is the fitting error.

Size parameters extracted from the best fit, *i.e.* the outer diameter, inner diameter, axial ratio and distribution of outer diameters are summarized in Table 4.1. It can be seen that the width of the size distribution is small, *i.e.* 10%-15%, which justifies the applicability of the decoupling approximation. However, from the larger relative width of the size distribution for HNP25, it may be concluded that controlling the size uniformity of smaller HNPs is more difficult than that for larger ones. The hollow ellipsoid model gives outer and inner radii very similar to those from the hollow sphere model for all three samples. For HNP25 and

HNP100B the best fit axial ratio is close to 1, meaning that the sphere model is the one best suited. On the other hand, for HNP50B the axial ratio is significantly larger than unity, suggesting a highly ellipsoidal shape. However, the polydispersity of this sample derived using the hollow ellipsoid model is much lower than that from the hollow sphere model. This result for HNP50B suggests that polydispersity and anisotropy of HNPs can compensate for each other in the hollow ellipsoid model. In other words, one cannot always distinguish between polydispersity and anisotropy. In fact, as was concluded in Chapter 3, the polydispersity of HNPs using the hollow sphere model agrees well with the results from other methods, i.e. TEM, dynamic light scattering and nitrogen adsorption-desorption isotherms. Therefore, in the analysis that follows, we decided to use the hollow sphere form factor and the hard sphere structure factor.

4.4.2 Morphology of Poly(ethylene oxide)-Embedded Hollow Nanoparticles

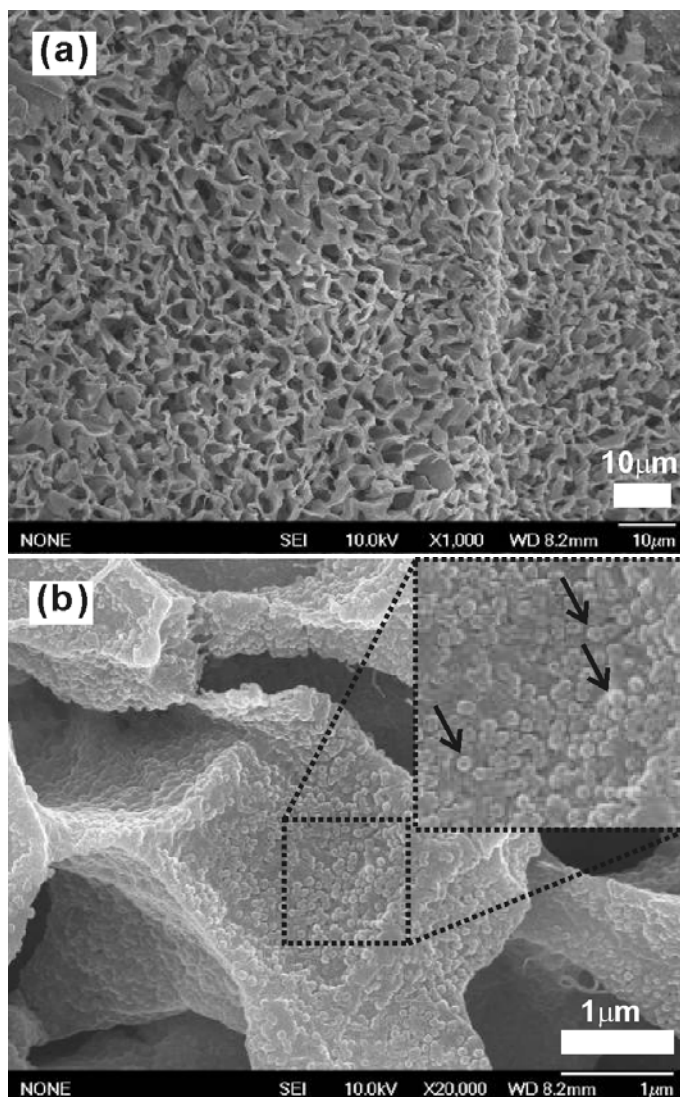


Figure 4.5 SEM images of freeze dried HNP50B-PEO. (a) low magnification, (b) higher magnification, with the inset in (b) showing details at still higher magnification. Arrows in the inset in (b) point to a few selected particles as examples. SEM images were supplied by Sun Hye Hwang and Jongmin Roh.

A SEM micrograph of the freeze dried sample of HNP50B-PEO is shown in Figure 4.5 as an example of the morphology of polymer-embedded nanoparticles. Pores with diameter of several micrometers can be seen in the prepared sample. This open pore structure can offer large surface area and enable rapid establishment of efficient contact between fluid and the polymer. HNPs loosely distributed over the surface of the matrix are clearly seen in Figure 4.5b. However, SEM does not reveal the internal structure of the polymer, *e.g.* the fraction of

HNPs buried inside the polymer matrix, the distribution of the buried HNPs in the polymer, and the extent of possible coverage of the HNPs by the polymer, either on the outside surface or on the internal cavity walls.

Regarding characterization of the morphology by SAXS, the SEM images suggest that a model more complex than that for water-dispersed particles should be applied to describe the HNP-PEO systems. The new model proposed in this study is shown in Figure 4.6. The new model treats the HNPs on the surface of the polymer matrix differently from those embedded within it. The surface HNPs are considered to be coated both inside and outside by a layer of PEO. The electron density of the polymer within the central void of the HNP and that of the polymer on the outer surface are treated as adjustable parameters. Therefore, HNPs on the surface are treated as having a hollow triple-shell structure (HTSS). For HNPs buried inside the PEO matrix, an inner layer of PEO is assumed to line on the wall of the central cavity; hence these particles are modelled as having a hollow double-shell structure (HDSS) with the surrounding PEO matrix as the medium. In HDSS, the surrounding PEO matrix was considered to provide the electron density baseline. This effectively reduces the model to a “core-shell” structure with a “negative” core. The form factor for the above two kinds of HNPs can be derived according to Equation 4.2. PY approximation for the structure factor is also used for both the surface and the embedded HNPs. The contribution to the total SAXS intensity by HNPs of the two kinds is considered to be linear in their volume fractions.

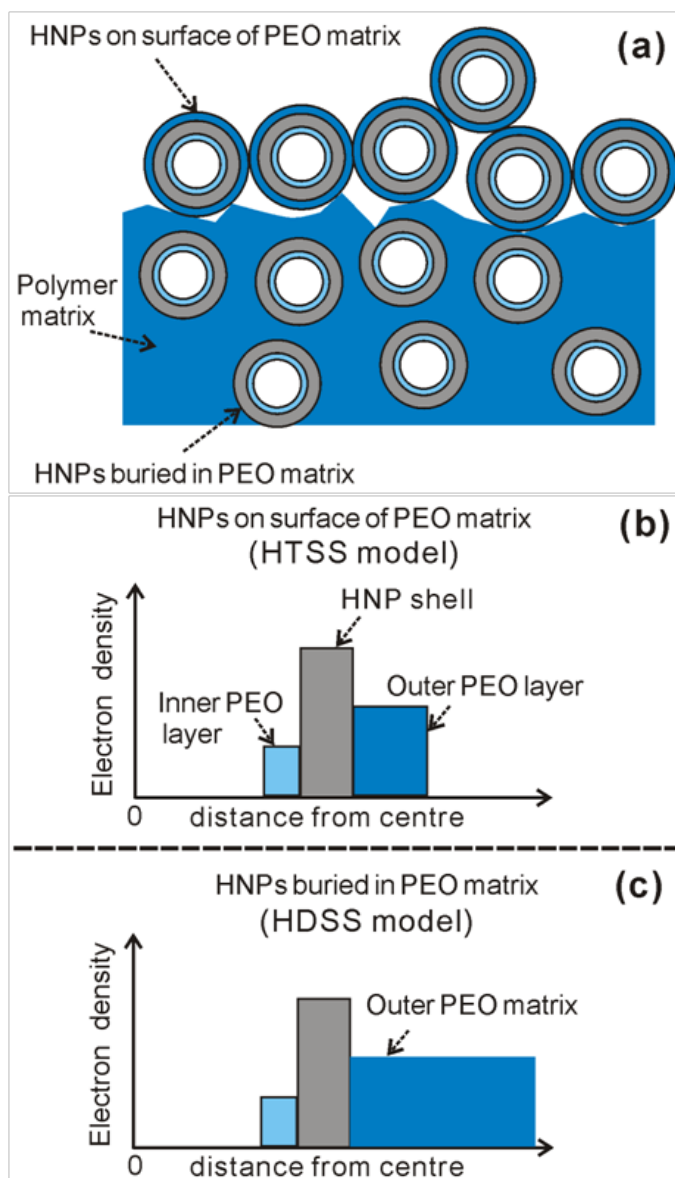


Figure 4.6 (a) Illustration of the model used to analyze SAXS data of polymer-embedded HNPs, and (b,c) their corresponding radial electron density profiles for HNPs on the surface (b) and buried within the polymer matrix (c).

Since the dimensions of the inorganic part of the HNPs, *i.e.* the outer, the inner diameter and the outer diameter distribution, remained unchanged during freeze drying, the previously obtained dimensions of HNPs listed in Table 4.1 were used and fixed in the fit for freeze dried samples. Figure 4.7 shows the experimental and fitted SAXS curves. Among other differences relative to the water-dispersed HNPs, here the first minimum and maximum of the SAXS curves of freeze dried samples are obviously shifted to lower q - see the comparison in Figure 4.7b. Further, the first minimum of the SAXS curves for freeze dried samples, *e.g.* around $q =$

0.1 nm^{-1} for HNP50B-PEO, has become significantly shallower. These changes in the SAXS curves indicate significant differences in the HNP form factor. With the new SAXS model proposed above, we obtain a rather good match between the experimental and fitted curves. However, some deviation exists in the fit for HNP100B-PEO, notably the oscillations in the low q range. It can be seen from Figure 4.7c that the fitted curve for HNP100B-PEO is the superimposition of the calculated curves from the surface HNPs and the buried HNPs. The oscillations at low q are primarily the result of the superposition of two distinct models. In reality, however, interface between surface HNPs and buried HNPs is not sharp, and intermediate states have the effect of smoothing the oscillations in the experimental scattering curve.

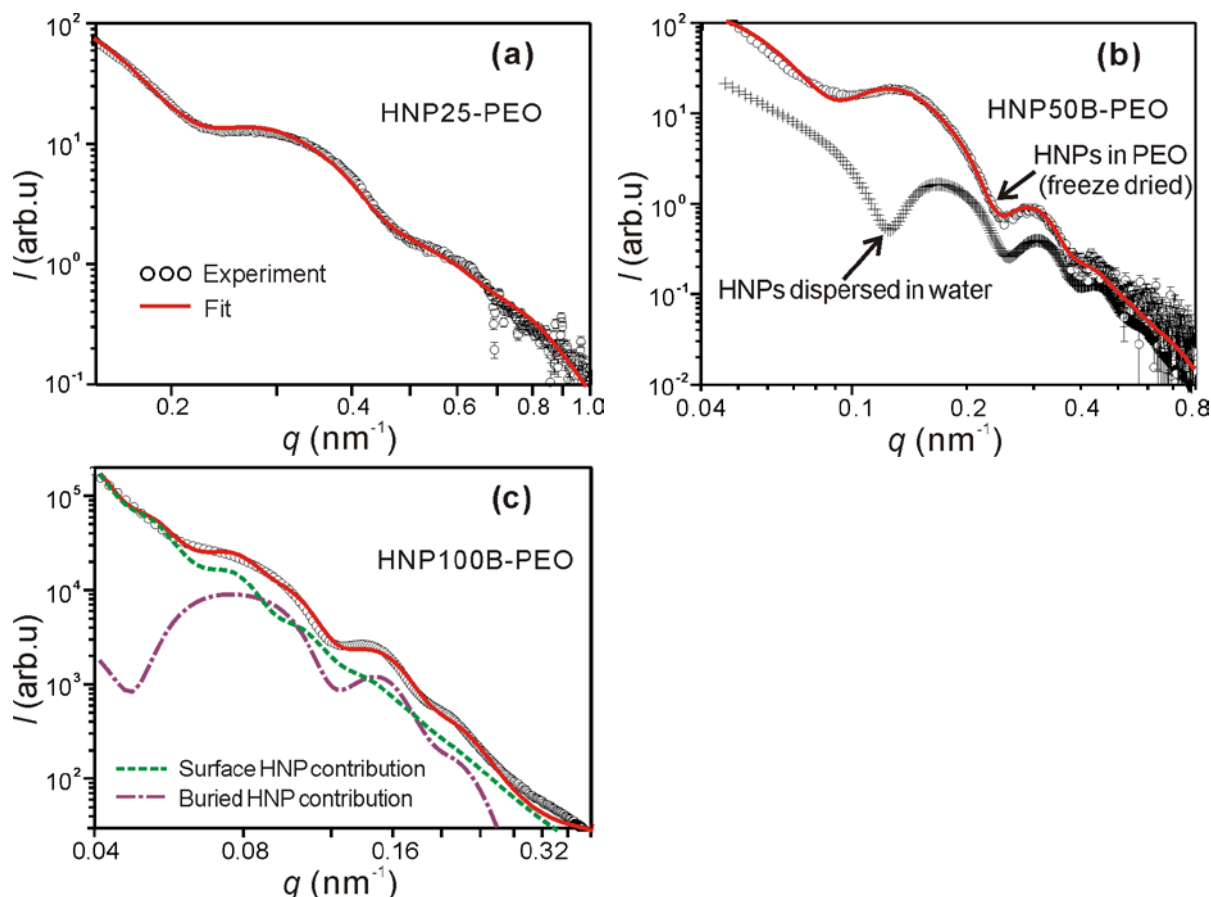


Figure 4.7 Experimental (open circle) and fitted (solid line) SAXS curves for freeze dried samples HNP25-PEO (a), HNP50B-PEO (b), and HNP100B-PEO (c). The experimental SAXS curve for water-dispersed HNPs, already shown in Figure 4.4b, is shown in Figure 4.7b only for comparison using the “+” symbols. The contribution to the calculated SAXS curve of HNP100B-PEO from HNPs on surface of matrix and from HNPs buried in matrix is shown with dashed line and dash-dot line in Figure 4.7c, respectively. All the experimental curves are shown after subtracting the scattering background from capillary and the polymer matrix.

The fitting results are summarized in Tables 4.2 and 4.3. In Table 4.2, the fraction of HNPs buried in PEO matrix of sample HNP100B-PEO is 0.85, a value much lower than that for HNP25-PEO and HNP50B-PEO, both giving a value of 0.96. This suggests that smaller HNPs are more easily embedded in the matrix. Regarding the inner PEO layer in the buried HNPs, it is evident that its thickness is larger in HNP100B-PEO than in HNP25-PEO and HNP50B-PEO. This could be attributed to the large inner cavities in HNP100B-PEO, and a larger amount of PEO depositing from a larger internal volume of solution. The derived packing densities of buried HNPs for all three samples are within the expected range. If we assume that all particles are buried in the matrix and that PEO is absent within the HNPs, the

estimated packing densities for HNP25-PEO, HNP50B-PEO, and HNP100B-PEO, according to the material weight fractions during sample preparation, are 0.25, 0.25, and 0.39, respectively. The surface density of surface HNPs may be underestimated to some extent since a three-dimensional structure factor is used to describe the distribution of surface HNPs. Therefore, the surface density of surface HNPs is less reliable compared to the packing density of buried HNPs. The roughly constant surface density and packing density for different samples is most likely due to the fact that the particle and polymer concentration in the initial solution before freeze drying was roughly the same in all cases. We chose this concentration in order to reach a balance between maximizing the scattering intensity while minimizing aggregation. Considering the thickness of the polymer layer within the HNP central void, this seems to be rather similar for embedded and surface particles. Further, it can be seen that the inner PEO layer is much thinner than the outer layer of the same particles. For HNP50B-PEO, the average outer diameter of the surface HNPs measured from the SEM image is 81 nm (Figure 4.5), a value in very good agreement with the best-fit SAXS diameter of 80.6 nm. For HNP25-PEO and HNP100B-PEO, the thickness of the outer PEO layer reaches 1.5 times that of the outer diameter of HNPs. It can be noticed that the outer PEO layer for HNP100B is considerably thicker than that of HNP50B-PEO and HNP25-PEO. This may be due to the slightly different sample preparation for HNP100B-PEO, i.e. injection of solvent-dispersed HNPs into a previously prepared freeze dried PEO matrix, followed by a second freeze drying.

Table 4.2 Fitting results giving morphological parameters of HNPs buried in the PEO matrix and HNPs on matrix surface by the newly proposed SAXS model

Samples	HNPs buried in PEO matrix			HNPs on surface of PEO matrix			
	Fraction of all HNPs (± 0.01)	Thickness of inner PEO (nm) (± 0.5)	Particle packing density (± 0.05)	Fraction of all HNPs (± 0.01)	Thickness of inner PEO (nm) (± 0.5)	Thickness of outer PEO (nm) (± 0.5)	Particle surface density (± 0.02)
HNP25-PEO	0.96	6.7	0.21	0.04	4.1	42.7	0.02
HNP50B-PEO	0.96	6.3	0.17	0.04	7.8	13.3	0.02
HNP100B-PEO	0.85	30.3	0.26	0.15	28.4	173.7	0.04

In Table 4.3, the electron densities derived are fairly reasonable. The fitted electron densities of the shell for HNP25-PEO, HNP50B-PEO, and HNP100B-PEO are all smaller than 883 e nm^{-3} , the electron density of amorphous $\text{SiO}_2/\text{TiO}_2$ without pores. The derived electron densities of the shell enable us to estimate the shell porosity again, giving values of 0.27, 0.39, and 0.25 for HNP25-PEO, HNP50B-PEO, and HNP100B-PEO, respectively. Overall, the shell porosities estimated here are consistent with those estimated by the combination of SAXS and nitrogen adsorption method which is shown in Table 3.2 of section 3.4.2 in Chapter 3. The fitted electron densities of the outer PEO for all three samples are very close to 370 e nm^{-3} , of the value for bulk PEO calculated using a density of 1.13 g/cm^3 . This indicates that the outer PEO after freeze drying is compact and without voids. However, it can be seen that the electron density of the inner PEO layer is lower than that of the bulk polymer. This may indicate that the PEO layer on the inner wall of HNPs is far from uniform.

Table 4.3 Best-fit electron densities of the inner and outer PEO layer and of the HNP shell, obtained with the new SAXS model proposed

Samples	Electron density of inner PEO (e nm^{-3})	Electron density of HNP shell (e nm^{-3})	Electron density of outer PEO (e nm^{-3})	χ^2
HNP25-PEO	270 ± 10	640 ± 10	340 ± 10	5.35
HNP50B-PEO	170 ± 10	570 ± 10	370 ± 10	2.99
HNP100B-PEO	70 ± 10	660 ± 10	360 ± 10	28.08

4.5 Conclusions

HNPs with well defined geometry were investigated in this chapter. The size parameters of HNPs, *i.e.* outer diameter, inner diameter, and size distribution, were determined by SAXS of water-suspended HNPs using a spherical hollow particle model and a structure factor based on hard sphere interaction. Application of an alternative form factor based on hollow ellipsoids and of a sticky hard sphere structure factor was tested but were found not to offer a significant advantage. HNPs supported on porous polymer scaffold were then prepared by freeze-drying. A new electron density model was developed to describe the morphology of such systems. In order to reproduce the experiment accurately it was necessary to consider separately the HNPs on the surface of the PEO matrix and HNPs buried within it. The SAXS analysis revealed that the majority of HNPs were buried in the PEO matrix. As the size of HNPs decreases, a higher fraction of HNPs, up to 96%, was found to be buried in the polymer matrix. This important information on distribution of HNPs is hard to obtain by other methods. The inner PEO layer deposited on the inner wall of the HNPs tends to be unaffected by the position of HNPs, *i.e.* whether at the surface or buried in the polymer matrix. However, the HNPs on the surface were found to be covered by a relatively thick layer of PEO. While the density of the outer PEO layer is similar to that of the bulk, that of the inner layer is significantly lower, indicating its porous or irregular morphology. For the largest HNPs investigated in this study (100 nm), the density of inner PEO is about 1/7 that of the outer PEO. The SAXS model proposed in this study has shown to successfully describe the morphology of HNPs on porous polymer scaffolds.

CHAPTER 5 Diffusion of Solvent in Poly(ethylene oxide)-Embedded Hollow Nanoparticles

Abstract

In this chapter, poly(ethylene oxide) (PEO)-embedded SiO₂/TiO₂ hollow nanoparticles (HNPs) (HNP-PEO) were prepared by the freeze drying technique. The characterization results for the morphology of the HNP-PEO composite shows that 96% of HNPs were buried uniformly in the PEO matrix, indicating HNPs can be used as markers for the diffusion of solvent into PEO matrix. The solvent diffusion experiments were carried out by using low molecular PEO in liquid state as the model solvent and *in-situ* small angle X-ray scattering (SAXS) as the time-resolved method. New complex SAXS models were built to analyze the diffusion process. In the new SAXS models, the original dry HNPs, both those at the surface and those buried inside the matrix, were found to be partially filled by the solvent before they were completely filled. The experimental SAXS curves were fitted by those from the new SAXS models. The time dependence of the fraction of the surface and the buried HNPs at different diffusion stage was extracted from the best fit. The fit results show that the diffusion process consisted of three stages, i.e. induction stage, steady state stage and depletion stage. The first-order consecutive reaction was applied to analyze the rate of diffusion at each stage. According to the reaction half lives determined, it was found that the rate of reaction in the steady state stage was about 3 times faster than that in the induction stage and about 90 times faster than that in the depletion stage. These results confirm that SAXS could be used as an *in-situ* monitoring method for the transport of small molecules into polymer gel, which is essential for the application of polymer gels as drug delivery vehicles.

KEYWORDS: Freeze drying technique, Porous polymer, Solvent diffusion, Core-shell SAXS model, First-order reaction.

*Chen, Z. H., Hwang, S. H., Zeng, X., Roh, J., Jang, J. & Ungar, G. *J. Phys. Chem. Letters*, 2013, in preparation.

5.1 Introduction

HNPs and freeze dried polymer gels are important drug delivery vehicles and they have attracted much attention over the years.^[147, 148, 169-171] However, the drug loading and release from HNPs and freeze dried gels have only been monitored by *ex-situ* methods, e.g. by measuring UV-vis spectra^[152] and swelling ratio^[171], respectively. Developing an *in-situ* method to monitor the transport of small molecules into or out of the drug delivery vehicles is therefore desirable. In Chapter 4, a polymer-embedded HNP system was prepared by freeze dry technique, and the morphology of the polymer-embedded HNP structure was characterized. The results shows that the polymer-embedded HNP system is suitable to test our proposal for using SAXS as the *in-situ* method with HNPs as the markers for the transport of solvent molecules. In this chapter, new batch of poly(ethylene oxide)-embedded HNPs (HNP-PEO) were prepared. The morphology of the HNP-PEO structure was determined by the SAXS model proposed in Chapter 4. Then, low molecular PEO in liquid state, hereafter named PEG, was selected as the model solvent for the diffusion of molecules into the freeze dried HNP-PEO structure. The diffusion of PEG was characterized by *in-situ* SAXS recorded using a remotely controlled syringe device. New complex SAXS models were derived to analyze the scattering curves and their time evolution during the diffusion of PEG. Kinetic analysis was finally carried out for the solvent diffusion based on the SAXS results. The current research is of importance because it can give the answer whether an *in-situ* monitoring method based on SAXS can be built for diffusion of solvent molecules in the delivery vehicles.

5.2 Experimental Section

5.2.1 Materials

The sample preparation method for HNPs and PEO-embedded HNPs has been described in Section 2.1 of Chapter 2.

HNP50B was selected as the model HNP, and the newly prepared freeze dried HNP50B in PEO was labeled HNP50B-PEO-B. The letter “B” indicates that the sample was from a new batch.

PEG with $M_w=200$ was selected as the model solvent for the diffusion experiments and the diffusion behavior of PEG was analyzed in this chapter, because PEG was the only solvent, among all the solvents tested in our experiments, that showed a measurable delay between solvent reaching the particle and filling it.

5.2.2 Methods

SAXS experiments were performed at beamline I22, Diamond Light Source, UK. Details of the SAXS experiments can be found in Section 2.2.1.2 of Chapter 2. The morphology of PEO-embedded HNPs was studied by recording SAXS curve of the as-prepared samples in capillaries. To study the diffusion of solvent into PEO-embedded HNPs, the home-made setup which has already been introduced in Section 2.2.1.2 of Chapter 2 was used. The length of a run in the diffusion experiment was set to be 150 s in total with data recorded every second in the first 30 s, every 3 seconds in the next 60 s, and finally a long exposure of 60 s. The time-resolved diffusion experiments were repeated on 17 different capillaries prepared in the same batch to confirm the reproducibility of the data. During the analysis of the SAXS data for solvent diffusion, a background arising from the undissolved porous polymer matrix was subtracted, after appropriate scaling, assuming that it maintained the same profile as that in the dry state; the latter was used to determine the morphology of freeze-dried PEO-embedded HNPs in Chapter 4. The background was subtracted. The background normalization constant was included as a parameter in the model and fitted during the simulation.

SEM images of freeze dried HNP in PEO were recorded by Sun Hye Hwang and Jongmin Roh.

5.3 Theoretical Model for Small Angle X-ray Scattering

Decoupling approximation (DA) and Percus-Yevick (PY) approximation are used to calculate the theoretical SAXS function. The hollow triple-shell sphere model (HTSS) shown in Section 4.3 of Chapter 4 is used again to calculate the form factor. PY approximation involving both 3-D and 2-D arrangement of hard spheres was used to calculate the structure factor. The formulae for the 3-D structure factor within PY approximation have already been presented in Section 3.3.1 of Chapter 3. Here, to more realistically describe the interaction among nanoparticles packing in 2D, e.g. on the surface of polymer matrix, 2-D structure factor within PY approximation is employed, and the formulae of the 2-D structure factor within PY approximation are shown as follows.

In a randomly disordered hard sphere system, as there are only short range interactions, the total correlation within the system can be described by direct correlation between two neighboring particles and by indirect correlation between all the other neighboring particles via a convolution.^[97] PY approximation is a successful approximation for the direct correlation function.^[96] However, within PY approximation, in contrast to the 3-D direct correlation function, there is no analytical solution for the 2-D direct correlation function and hence no analytical solution for 2-D structure factor. In order to reduce numerical computation, many studies have been carried out to find appropriate semi-empirical functions^[177] or approximated analytical functions^[105, 106, 178] to describe the 2-D direct correlation function. In the following we describe an approximation for the analytical solution of direct correlation function for hard sphere packing in 2D, as was recently proposed by Guo and Riebel.^[105] We chose to use it in this project due to its simplicity and accuracy of the solution.

The structure factor $S(q)$ for hard sphere packing in 2D can be expressed by

$$S(q) = \frac{\pi R_0^2}{\pi R_0^2 - \eta C(q)} \quad (5.1)$$

where η is the surface coverage of particles, and $C(q)$ is the direct structure factor for particles packing in 2D. The direct structure factor $C(q)$ is given by

$$C(q) = 2\pi \int_0^{\infty} C(r) \cdot J_0(qr) r dr \quad (5.2)$$

where $C(r)$ is the direct correlation function for particles packing in 2D, and $J_0(q)$ is Bessel function of the first kind of zeroth order. The direct correlation function $C(r)$ proposed by Guo and Riebel^[105] can be written as

$$C(r) = \begin{cases} \frac{b\eta^2 - 1}{(1 - 2\eta + b\eta^2)^2} \{1 - a^2\eta \\ + a^2\eta \cdot \frac{2}{\pi} \cdot [\arccos(\frac{r}{2aR_0}) \\ - \frac{r}{2aR_0} \cdot (1 - \frac{r^2}{4a^2R_0^2})^{1/2}] \}, & r < 2R_0 \\ 0 & , \quad r \geq 2R_0 \end{cases} \quad (5.3)$$

where a and b are simplified parameters with $a = 0.3699\eta^4 - 1.2511\eta^3 + 2.0199\eta^2 - 2.2373\eta + 2.1$ and $b = (6.9282\pi - 12)/\pi^2$. It should be noted that even though an approximation for the expression for the direct correlation function is available, calculation of the 2-D structure factor $S(q)$ has to be done numerically since $S(q)$ involves an integral over the Bessel function of first kind of zeroth order shown in Equation 5.2.

In this chapter, 2-D structure factor is only used in the calculation of the scattering intensity of the HNPs on the surface of the polymer matrix in our polymer-embedded HNP systems.

5.4 Results and Discussion

In Section 5.4.1, the morphology of freeze dried sample HNP50B-PEO-B is characterized. In Section 5.4.2, diffusion of PEG in HNP50B-PEO-B is studied by *in-situ* SAXS. New complex

SAXS models are proposed to investigate the filling of HNPs during diffusion. Finally, the kinetics of diffusion is discussed based on the fit results from SAXS.

5.4.1 Morphology of Poly(ethylene oxide)-Embedded Hollow Nanoparticles

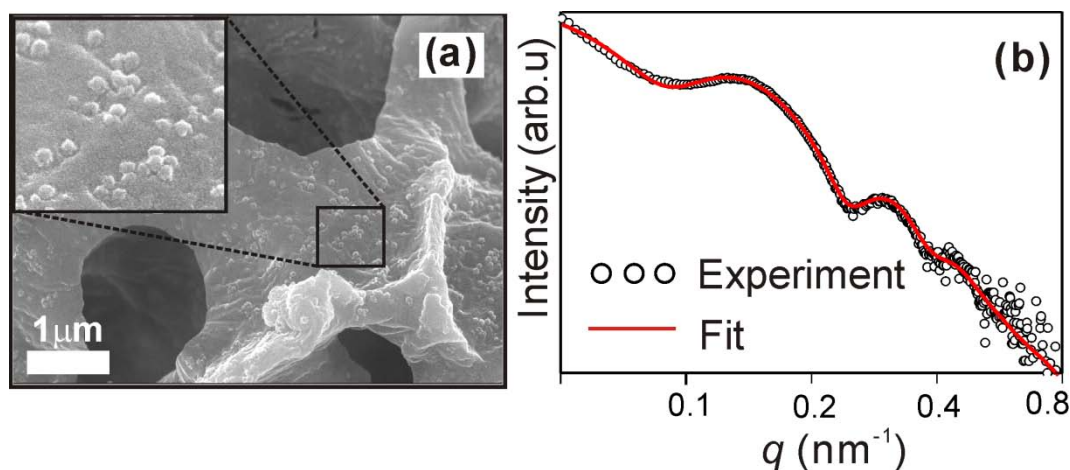


Figure 5.1. (a) SEM image of PEO-embedded HNPs, and (b) experimental and fitted SAXS curves for PEO-embedded HNPs. SEM image was supplied by Sun Hye Hwang and Jongmin Roh.

Since the freeze dried sample used in this chapter, i.e. HNP50B-PEO-B, was prepared from different batches compared to that used in Chapter 4, its morphology has to be determined before the study for solvent diffusion. From the SEM image shown in Figure 5.1a for HNP50B-PEO-B, it can be seen that the PEO-embedded HNP structure consists of porous polymer scaffold with pores of several micrometers in diameter and HNPs distributed loosely over the surface of the polymer matrix. The internal structure of the polymer was further revealed by the SAXS models proposed in Chapter 4. The fit results are shown in Figure 5.1b. It can be seen from Figure 5.1b that the fitted curve matches the experimental curve properly in all q range. Parameters extracted from the fit were summarized in Table 5.1 and 5.2. The fitted parameters show that 96% of HNPs are buried inside the matrix. A thin layer of PEO is deposited on the wall of inner cavities of both surface HNPs and buried HNPs, while a thick layer of PEO is deposited on the outer surface of surface HNPs. If assuming PEO did not escape from the inner cavity during freeze drying and the freeze dried PEO had a porosity of 0.5, the estimated thickness of inner PEO in both surface HNPs and buried HNPs according to

the original concentration of PEO is 1.4 nm, a value comparable to that derived from the fit. It is interesting to find that the electron density of the inner PEO layer is lower than that of bulk PEO, indicating a porous structure or inhomogeneous distribution of PEO on the wall of inner cavities. It is also interesting to find that the electron density of the outer PEO is the same as that of bulk PEO, indicating the outer PEO is compact and without void after freeze drying. The electron density of the inorganic HNP shell determined here enable us to estimate the shell porosity of HNPs, giving a value of 0.38 which is comparable to the result of 0.33 obtained by the combination of SAXS and nitrogen adsorption-desorption isotherm reported in Chapter 3.^[71]

Table 5.1 Fitting results giving morphological parameters of PEO-embedded HNPs, i.e. HNPs buried in the PEO matrix and HNPs on matrix surface

Sample	HNPs buried in PEO matrix			HNPs on surface of PEO matrix			
	Fraction of all HNPs (± 0.01)	Thickness of inner PEO (nm) (± 0.5)	Particle packing density (± 0.02)	Fraction of all HNPs (± 0.01)	Thickness of inner PEO (nm) (± 0.5)	Thickness of outer PEO (nm) (± 0.5)	Particle surface density (± 0.02)
HNP50B-PEO-B	0.96	5.4	0.14	0.04	1.9	12.7	0.02

Table 5.2 Fitting results for electron densities of the inner and outer PEO layer and of the HNP shell

Sample	Inner PEO ($e \text{ nm}^{-3}$)	HNP shell ($e \text{ nm}^{-3}$)	Outer PEO ($e \text{ nm}^{-3}$)	Bulk $\text{TiO}_2/\text{SiO}_2$ ($e \text{ nm}^{-3}$)*	Bulk PEO ($e \text{ nm}^{-3}$)*
HNP50B-PEO-B	180 ± 10	550 ± 10	370 ± 10	880	370

* The electron densities of bulk $\text{TiO}_2/\text{SiO}_2$ and of bulk PEO are put in the table as comparison.

5.4.2 Diffusion of Solvent in Poly(ethylene oxide)-Embedded Hollow Nanoparticles

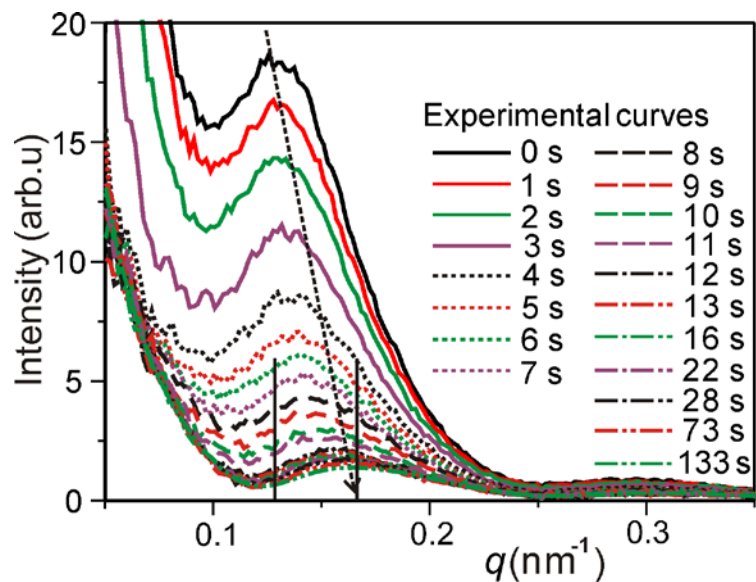


Figure 5.2 Experimental SAXS curves for the diffusion of PEG in PEO-embedded HNPs, i.e. the sample HNP50B-PEO-B. The curves have been scaled according to their exposure time, and the background arising from porous polymer matrix has been subtracted. The dashed arrow shows the shift of the scattering peaks, and the two vertical black lines show the distance of the shift.

The experimental SAXS curves for the diffusion of PEG in HNP50B-PEO-B are shown in Figure 5.2. The scattering background due to capillary and the porous polymer matrix after freeze drying has been subtracted. In the following, starting with Figure 5.2, $t = 0$ is defined as the time of the solvent reaching the irradiated volume in the capillary, as judged by the onset of the decrease in transmitted and scattered intensity. In Figure 5.2, it can be seen that the intensity of curves decreases dramatically in the first 5 s, indicating large change in the system, i.e. filling of the surface HNPs by PEG, and possible dissolving of PEO matrix by PEG, followed by the dissolution of shallowly buried HNPs. After the first several seconds, the decrease of intensity slows down. It is notable that, with the increase of diffusion time, the first peak of the scattering curve gradually shifts to higher q , i.e. roughly from $q = 0.12 \text{ nm}^{-1}$ to 0.17 nm^{-1} , as is shown by the black dashed arrow in Figure 5.2. This high- q shift of the peak indicates that the weighted electron density distribution corresponding to an average HNPs decreases gradually. This, in turn, means that the HNPs are being filled. Therefore, new

SAXS models are necessary to describe the filling of HNPs during PEG diffusion. Together with the surface HNP model and buried HNP model proposed in Chapter 4^[76], two further model electron density distributions are proposed here, namely those corresponding to partially filled and completely filled HNPs. As will be shown below, both are required to fit the scattering curves adequately and describe accurately the state of HNPs during the diffusion of solvent.

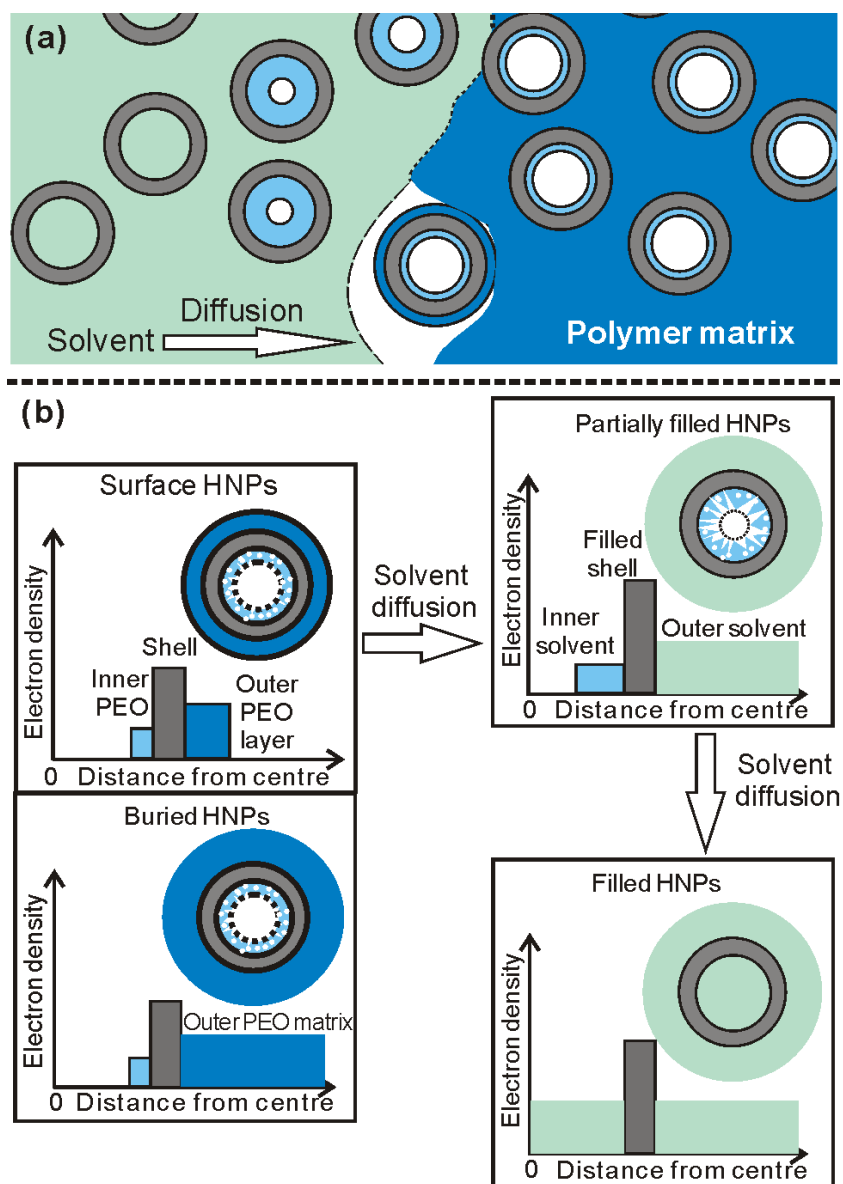


Figure 5.3 SAXS models proposed for solvent diffusion. (a) Illustration of the diffusion direction. (b) Filling of HNPs and the change of corresponding electron density profiles from surface HNPs and buried HNPs to partially filled HNPs and then to filled HNPs.

The SAXS models proposed are shown in Figure 5.3, including the overall diffusion process shown in Figure 5.3a and the transition of electron density profiles of HNPs shown in Figure 5.3b. As is shown in Figure 5.3a, after the solvent comes in contact with the freeze dried sample, surface and buried HNPs will be gradually dissolved and filled, alongside the dissolution of the polymer matrix. Then, partially filled HNPs and filled HNPs appear as a result of the filling of the inner cavities of surface HNPs and buried HNPs. With the advance of the liquid-solid interface during solvent diffusion, more and more HNPs enters the solvent, and hence the fractions of the above four kinds of HNPs vary, which gives us a chance to characterize the diffusion process. From electron density profiles of HNPs shown in Figure 5.3b, surface HNPs are considered by a hollow triple-shell sphere model while the buried HNPs are considered by a hollow double-shell sphere model. The electron density model of surface HNPs and buried HNPs has been explained in Chapter 4, and hence there is no need to explain again. The partially filled HNPs are considered to consist of a filled inorganic shell and a layer of solvent lining on the inner wall. This is reasonable since the diffusion of solvent in the porous inorganic shell can occur instantly. For filled HNPs, since the inner cavity of this kind of HNPs is totally filled by solvent, the electron density profile of them is effectively the same as that of as prepared HNPs.

The form factors of the above four kinds of HNPs can be calculated according to their electron density profile, while PY approximation for hard sphere^[60, 96, 105, 106] is used to calculate the structure factor. It should be mentioned here that the 3-D structure factor within PY approximation is used for both buried HNPs and filled HNPs, while the 2-D structure factor within PY approximation is used for surface HNPs. Additionally, the interaction among partially filled HNPs is neglected since the freeze-dried sample was originally prepared from dilute solution of HNPs and the concentration of partially filled HNP can be very low. Details of the SAXS theory on the calculation for the SAXS models can be found in Section 5.3 of this chapter.

The theoretical SAXS intensity from the combination of the above four models, i.e. surface HNPs, buried HNPs, partially filled HNPs, and filled HNPs, is calculated and fitted to the experimental curves. It is noticed that the morphology of surface HNPs and buried HNPs determined in Section 5.4.1 are used and fixed during the fit for SAXS results of solvent diffusion. The only change for surface HNPs and buried HNPs in the fit for solvent diffusion

is their volume fractions. An illustration of such a fit is shown in Figure 5.4 by taking the fit results of the 5th second of the diffusion process as an example. It can be seen from Figure 5.4 that the calculated SAXS curve matches the experimental curve fairly well, indicating our models are successful ones. Regarding the calculated curves of each kind of HNPs, it is obvious that the profile of curves is different from each other. The first peak of the partially filled HNPs, i.e. at around $q = 0.15 \text{ nm}^{-1}$, locates between that of buried HNPs and filled HNPs. The location of the first peak of the partially filled HNPs is understandable since this kind of HNPs originates from buried HNPs and finally evolves into filled HNPs. The profile of the calculated curve for surface HNPs is largely different from those of buried HNPs and partially filled HNPs but is relatively similar to that of filled HNPs; this phenomenon is also understandable since the surface HNPs having a hollow triple shell sphere structure is effectively similar to the filled HNPs having a hollow single shell sphere structure when considering all the shells as a whole.

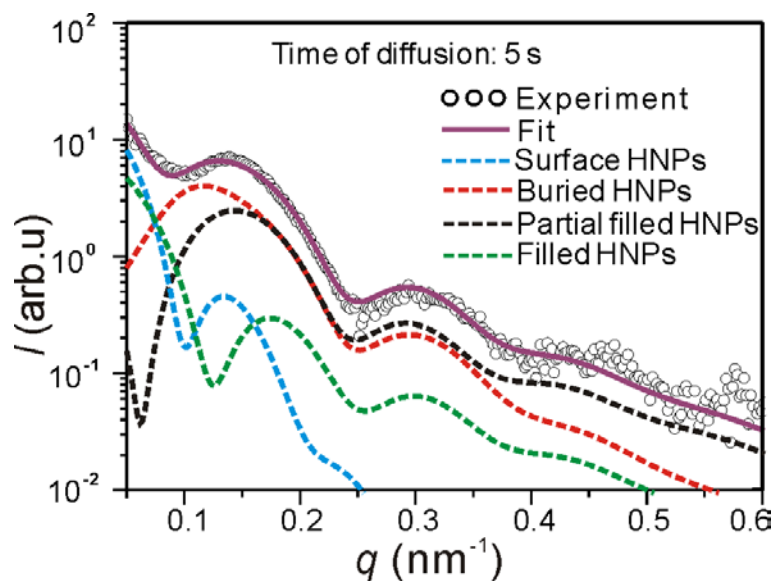


Figure 5.4 Illustration of the experimental (open circles) and fitted SAXS (purple-solid line) curves for PEG diffusion by taking the result at 5th s in the diffusion as an example. The fitted curve contains contributions from the four SAXS models shown in **Figure 5.3b**, i.e. surface HNPs (blue-dashed line), buried HNPs (red-dashed line), partially filled HNPs (black-dashed line), and filled HNPs (green-dashed line).

The above fit routine was then applied to all the SAXS curves recorded for solvent diffusion. The fit results for PEG diffusion are shown in Figure 5.5. In Figure 5.5, for clarity, only some of the experimental and fitted curves are shown to illustrate the overall tendency of the change

during solvent diffusion. Details of the fit for each curve in PEG diffusion can be found in Section A2 of the Appendix of the thesis. From Figure 5.5, it can be seen that the fit quality of all curves is acceptable in the whole q range, indicating the SAXS models proposed in this chapter are successful.

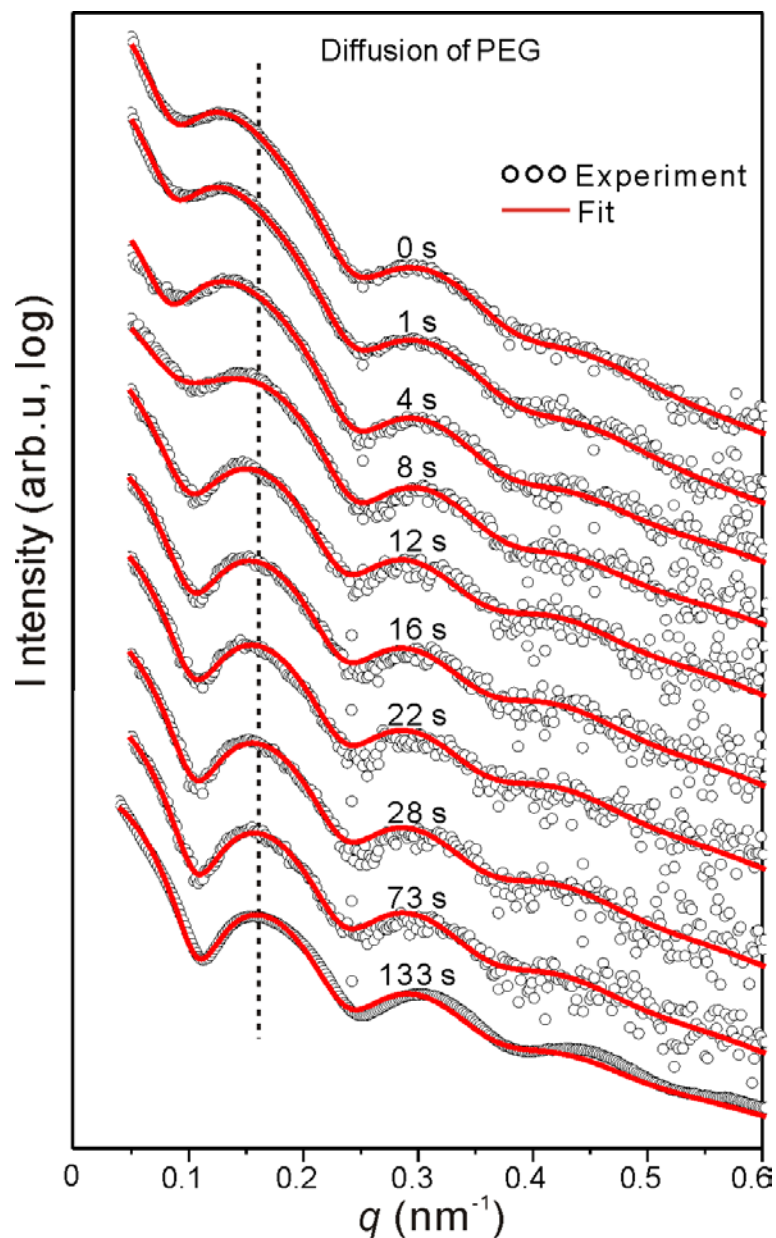


Figure 5.5 Experimental (open circles) and fitted (red solid line) SAXS curves for PEG diffusion in HNP50B-PEO-B. For clarity, only a few curves are shown here. The vertical dotted line indicates the shift of the position of first peak during solvent diffusion. The curves are vertically shifted for clarity.

The parameters extracted from the above fit are summarized in Table 5.3 and plotted in Figure 5.6. Details on the change of each parameter can be found in Table 5.3, while the overall tendency of change can be seen in Figure 5.6.

It is interesting to analyze the details on the change of each parameter first, i.e. the data in Table 5.3. As is seen the fraction of surface HNPs decreases gradually and this kind of HNPs

disappeared at 7 s. The reason why surface HNPs were not filled instantly may be that parts of surface HNPs were surrounded by air bubbles, which prevents quick vanishing of surface HNPs. The change in the fraction of buried HNPs is much larger than that in surface HNPs, e.g. the fraction of buried HNPs in all HNPs changed from 0.96 to 0.82 within the first 3 s. The rate of the disappear of buried HNPs was even faster afterward. The above tendency can be explained by the fast dissolution of PEO in PEG when they come into contact and by the further increase in the contact area when the polymer scaffold breaks down. The buried HNPs disappear at 12 s. The partially filled HNPs started to appear immediately after the solvent contacted the polymer matrix, and they continued existing the entire diffusion time recorded. The fraction of partially filled HNPs in all HNPs quickly increases to 0.32 within 4 s, and then it remains fairly stable until 8 s. After reaching the highest value of 0.39 at 12 s, the fraction of partially filled HNPs decreases back to the level around 0.32, followed by further slower decrease within the recording time. The leveling off of the decrease in the fraction of partially filled HNPs after 12 s may be due to the difficulty in the removal of the air bubbles trapped inside the inner cavity of the partially filled HNPs. The thickness of the inner solvent layer in the partially filled HNPs increases from 0 nm to 7.4 nm quickly, indicating the inner PEO layer of the buried HNPs swells rapidly. After that, the thickness of inner solvent keeps roughly at around 9.6 nm until the depletion of the buried HNPs. Then, the thickness of the inner solvent layer starts to increase again until the inner space of the cavity is completely filled, i.e. when it reaches a value of 21.1 nm. The change of the electron density of the inner solvent of partially filled HNPs is similar to the change in thickness of the inner solvent. However, the electron density of the inner solvent did not reach the electron density of bulk solvent, i.e. 370 e nm^{-3} . This may be explained by some retention of air bubbles trapped inside the inner cavity, which gave an average lower electron density of the inner solvent than that of the bulk PEG. The filled HNPs start to appear 5 s after the beginning of diffusion. It can be seen that the fraction of filled HNPs increases fast at first and slower thereafter. Limited by the persistence of partially filled HNPs, the fraction of filled HNPs did not reach 1 within the recording time. The packing density of filled HNPs is very low even at the final stage of the diffusion, which is reasonable, considering the low concentration of HNPs used in the preparation of the freeze dried sample.

Table 5.3 Fit results for the time dependence of the fraction of surface HNPs, buried HNPs, partially filled HNPs, and filled HNPs, and of the thickness and electron density of the inner solvent layer in the partially filled HNPs.

Time	Surface HNPs	Buried HNPs	Partially Filled HNPs			Filled HNPs	
	Fraction (± 0.01)	Fraction (± 0.01)	Fraction (± 0.01)	Thickness of Inner solvent (nm) (± 0.5)	Electron density of inner solvent ($e \text{ nm}^{-3}$) (± 5)	Fraction (± 0.01)	Packing density (± 0.02)
0 s	0.04	0.96	0	-	-	0	0
1 s	0.04	0.93	0.03	7.4	129	0	0
2 s	0.03	0.89	0.08	9.7	99	0	0
3 s	0.02	0.82	0.16	10.1	143	0	0
4 s	0.02	0.66	0.32	9.7	130	0	0
5 s	0.01	0.53	0.32	9.9	106	0.14	0
6 s	0.01	0.48	0.33	9.9	119	0.18	0
7 s	0.01	0.45	0.31	10.3	159	0.23	0
8 s	0	0.32	0.31	9.2	114	0.37	0
9 s	0	0.24	0.33	9.5	133	0.43	0
10 s	0	0.11	0.37	9.2	110	0.52	0
11 s	0	0.05	0.36	8.8	118	0.59	0
12 s	0	0	0.39	12.6	137	0.61	0
13 s	0	0	0.37	13.4	150	0.63	0.04
16 s	0	0	0.36	14	164	0.64	0.04
22 s	0	0	0.33	14.7	170	0.67	0.04
28 s	0	0	0.32	14.9	181	0.68	0.04
73 s	0	0	0.31	18	190	0.69	0.04
133 s	0	0	0.29	21.1	198	0.71	0.05

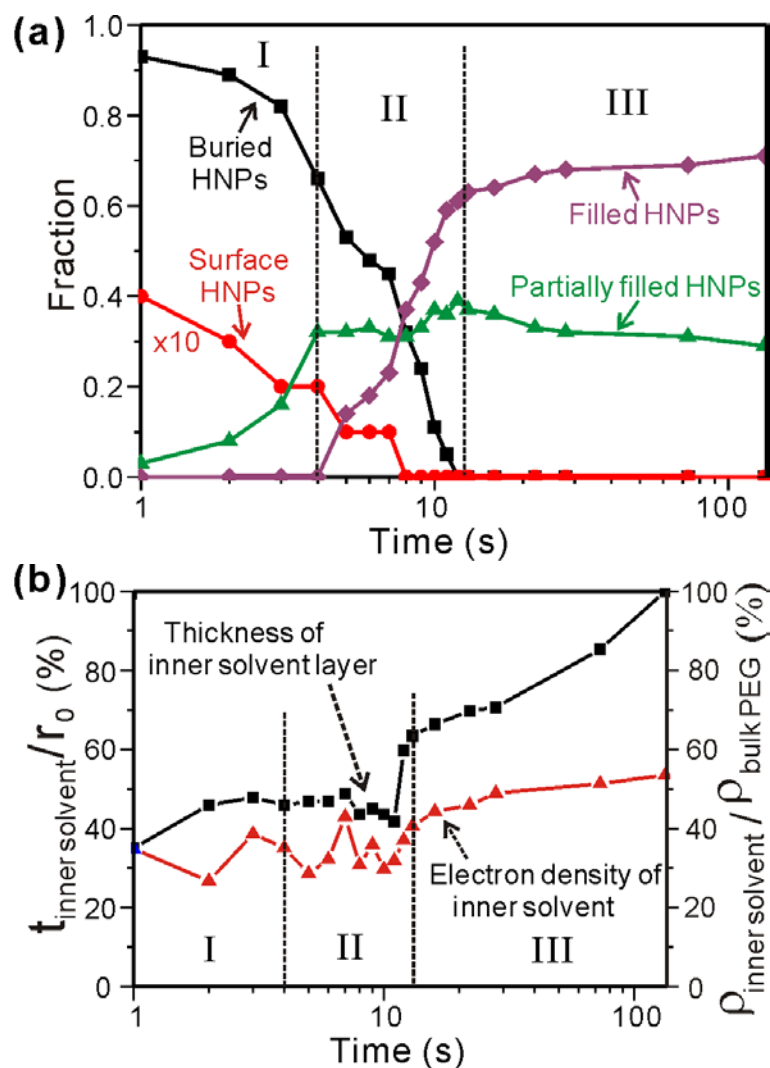


Figure 5.6 (a) Change of the fraction of different kinds of HNPs during PEG diffusion. The fraction of surface HNPs was multiplied by a factor of 10 for clarity. (b) Change of the thickness and the electron density of the solvent penetrating into the inner cavities of HNPs in the case of partially filled HNPs. In axes of (b), $t_{\text{inner solvent}}$ is the thickness of the penetrating solvent, r_0 is the inner radius of HNPs, $\rho_{\text{inner solvent}}$ is the electron density of the penetrating solvent, and $\rho_{\text{bulk solvent}}$ is the electron density of bulk PEG solvent.

The above fit results for the change of the fraction of the four kinds of HNPs are plotted in Figure 5.6a. It can be seen from Figure 5.6a that the diffusion process can be divided into three stages. In stage I (within the first 4 s) the only transformation observed is that of surface HNPs and buried HNPs to partially filled HNPs. In stage II (from 4th to 12th s) four kinds of HNPs coexist. Ignoring the low fraction of surface HNPs, it is interesting to see that the

fraction of partially filled HNPs stays nearly constant, and the decrease in the fraction of buried HNPs matches the increase in the fraction of filled HNPs. This means that the filling of the HNPs reaches steady state kinetics during stage II. At stage III, i.e. after 12th s, the buried HNPs disappear, and detectable transformation only occurs from partially filled to filled HNPs. Figure 5.6b shows the change in thickness of the inner solvent layer and of its electron density in partially filled HNPs. It is interesting to note that the change of the above two parameters shows similar trend. During stage II, these two parameters keep approximately constant, indicating again a steady state in the transformation of the HNPs. As is mentioned above, the lower electron density of the inner solvent than that of bulk solvent may be due to some air bubbles trapped inside the inner cavity.

5.4.3 Analysis of Diffusion Kinetics

In order to analyze the diffusion kinetics of the solvent, the general consecutive first order reaction model was employed. In a general consecutive chemical reaction, the reaction scheme can be expressed by



where A, B and C are the initial reactant, the intermediate reactant and the final product, respectively, while k_1 and k_2 are the rate constants of the A to B reaction and of the B to C reaction, respectively. In the above consecutive reaction, the dependence of the concentration of A, B and C on the time t can be expressed by ^[179]

$$[A] = [A]_0 e^{-k_1 t} \quad (5.5)$$

$$[B] = \frac{k_1}{k_2 - k_1} \cdot (e^{-k_1 t} - e^{-k_2 t}) \cdot [A]_0 \quad (5.6)$$

$$[C] = \left(1 + \frac{k_1 e^{-k_2 t} - k_2 e^{-k_1 t}}{k_2 - k_1}\right) \cdot [A]_0 \quad (5.7)$$

where $[A]_0$, $[A]$, $[B]$ and $[C]$ are the initial concentrations of A, the concentration of A at time t , the concentration of B at time t and the concentration of C at time t , respectively. It is noted that at any time of reaction $[A] + [B] + [C] = [A]_0$.

According to the time dependence of the fraction of the four kinds of HNPs, the diffusion process can be divided into three stages as shown above in Figure 5.6a. In the language of kinetics of consecutive chemical reactions, stage I can be considered as the induction stage, stage II as the steady state stage (propagation) and stage III as the depletion stage. Since there is only a small fraction of surface HNPs in the system and its change is negligible compared to the change in the fractions of the other three kinds of HNPs, the surface HNPs are not taken into account in the following analysis. Therefore, the induction stage I can be described as the build-up of partially filled HNPs through transformation from the buried empty ones. The steady state stage, i.e. stage II, is the conversion of buried HNPs into filled HNPs, with partially filled HNPs as the intermediate state. During the depletion stage III the concentration of partially filled HNPs decreases again as the feedstock of empty HNPs is depleted. It is obvious that stage I, II and III are all able to be described by the consecutive reaction scheme shown in Equation 5.4, with A, B and C the fractions of the total initial number of buried HNPs of, respectively, buried HNPs, partially filled HNPs and filled HNPs.

The theoretical fractions of various HNPs are calculated with Equations 5.5-5.7 according to first-order reaction kinetics. The calculated fraction is then fitted to the results derived from our SAXS models. The best fits are plotted in Figure 5.7. From Figure 5.7, it can be seen that the fit results for fraction of HNPs in stage I, II and III are acceptable, indicating that the transition of HNPs from buried HNPs to partially filled HNPs and then to filled HNPs can be appropriately described by a first-order consecutive reaction model. The rate constant k_1 derived for stage I is 0.07 s^{-1} . The reactant half life corresponding to k_1 is about 10 s. In stage II, the rate constant k_1 and k_2 are 0.22 s^{-1} and infinite large, respectively. The reactant half life corresponding to k_1 is about 3 s, a value much lower than that in stage I. In stage III, the rate constant k_2 is 0.0025 s^{-1} . The reactant half life in stage III corresponding to k_2 is about 277 s, a value much larger than those in stage I and stage II. From the half lives of reactions determined, it can be seen that the transition of HNPs in stage II is about 3 times faster than that in stage I and about 90 times faster than that in stage III. The long half life of reaction in stage III indicates the transition of HNPs may take far more time to finish. However, it should

be mentioned that the analysis for the diffusion kinetics was based on simplified reaction mechanism. Improvement to the analysis will be done in the future.

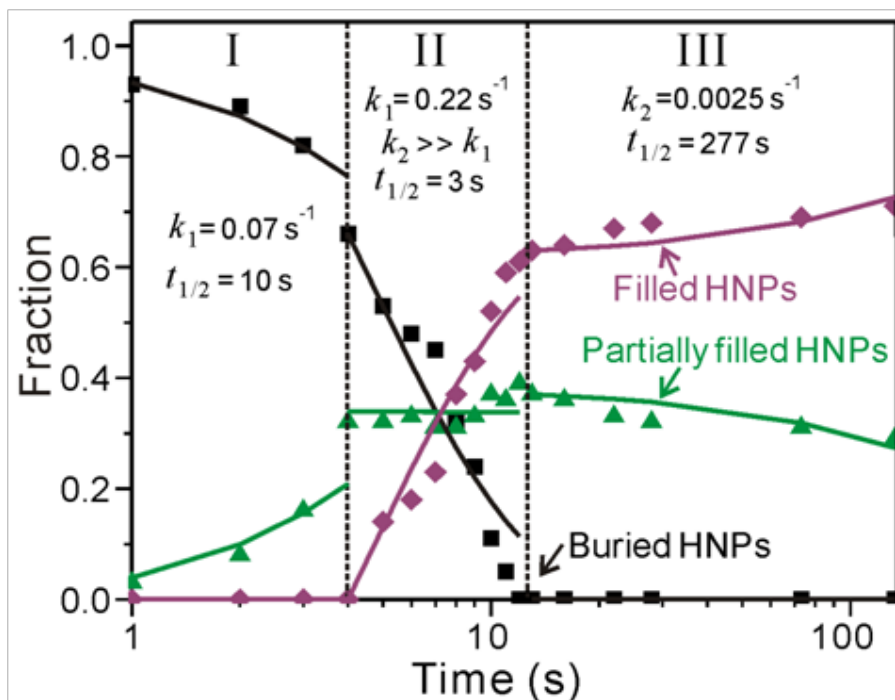


Figure 5.7 Rate constant determination for transition of buried HNPs, partially filled HNPs and filled HNPs during the diffusion process in stage I (a), stage II (b), and stage III (c). Symbols (square, triangle and diamond) are the fractions of different kinds of HNPs shown in **Table 5.3**, while solid lines are the calculated fractions of HNPs with first-order consecutive reaction model.

5.5 Conclusions

In this chapter, polymer-embedded HNPs were prepared by the freeze drying method, and their morphology was characterized by SAXS and electron microscopy. Since 96% of HNPs were buried uniformly inside the polymer matrix, the polymer-embedded HNP system proves to be a suitable system to test our method to develop SAXS as the *in-situ* method for monitoring solvent diffusion in polymer gel by using HNPs as markers. Diffusion of PEG into PEO-embedded HNPs was used as a model system to test the *in-situ* method. New complex electron density models were proposed to describe the status of HNPs during the filling of HNPs in solvent diffusion, including the surface HNP model, buried HNP model, partially filled HNP model and filled HNP model. Successful fitting of the experimental SAXS curves by the theoretical SAXS curves confirmed the viability of our models. Analysis of the fitting parameters gave the information that the diffusion process consists of three stages, i.e. the induction stage, the steady stage, and the depletion stage. Further, the rates of reactions at each stage were analyzed by a first-order consecutive reaction model. It is found that the filling rate of HNPs in the steady stage is about 3 times faster than that in the induction stage and about 90 times faster than that in the depletion stage. Our work on diffusion of PEG into PEO-embedded HNPs by *in-situ* SAXS confirm that our method can be used to monitor the transport of fluid into polymer gels for their application as drug delivery vehicles.

CHAPTER 6 Diffusion of Solvents in Poly(methyl methacrylate)- and Polyethylene-embedded Hollow Nanoparticles

Abstract

In order to test the applicability of our SAXS models to various cases of solvent diffusion in polymer-embedded HNPs, poly(methyl methacrylate) (PMMA)-embedded HNPs and polyethylene(PE)-embedded HNPs were prepared by freeze drying technique. The diffusion of different solvents in the above two kinds of polymer-embedded HNPs was monitored by *in-situ* SAXS, including the diffusion of water into PMMA-embedded HNPs and the diffusion of water, oleyl alcohol and tetrafluorobenzene into PE-embedded HNPs. The investigation to the morphology of the as-prepared PMMA-embedded HNPs and PE-embedded HNPs shows that HNPs aggregated on the surface of polymer matrix. Further, the aggregation of HNPs hinders the application of our SAXS models to analyze the internal morphology of the polymer matrix. The recorded SAXS curves for solvent diffusion indicate that in all cases, except the diffusion of water in PE-embedded HNPs, the diffusion procedure consisted of two diffusion processes, i.e. a fast process and a slow process. The fast process was due to the fast filling of outer empty space of the sample and possible fast filling of the surface HNPs by solvent, while the slow process arose from the slow filling of the buried HNPs or small gaps in the polymer matrix. By testing the diffusion of various solvents into PMMA- and PE-embedded HNP systems, the results in this chapter indicate that *in-situ* SAXS is a valid method to monitor the solvent diffusion process. However, to obtain quantitative results for solvent diffusion, the SAXS models and sample preparation methods need to be considered carefully, especially for freeze dried samples with aggregated HNPs.

KEYWORDS: Freeze drying technique, Solvent diffusion, Water, Oleyl alcohol, Tetrafluorobenzene, Poly(methyl methacrylate), Polyethylene.

6.1 Introduction

It has been concluded in Chapter 5 that the diffusion of solvent in polymer-embedded HNPs can be monitored by *in-situ* SAXS. However, only the diffusion of solvent in poly(ethylene oxide)-embedded HNPs was investigated there. It would be interesting to test our method for other polymer-embedded HNP systems as well. In this chapter, polymers which have different polarity compared to poly(ethylene oxide), i.e. poly(methyl methacrylate) (PMMA) and polyethylene (PE), were chosen to prepare polymer-embedded HNPs by freeze drying method. The SAXS models used in previous chapters were applied to the two systems (PMMA- and PE-embedded HNPs) to obtain their morphological information. Solvents with different polarity, i.e. water, oleyl alcohol and tetrafluorobenzene, were selected to investigate the diffusion of solvents into them. The main objectives of this work are to test the applicability of our SAXS models for different polymer-embedded HNPs, and to investigate the diffusion kinetics of various solvents into polymer-embedded HNP systems.

6.2 Experimental Section

6.2.1 Materials

In this study, HNP50C was used. The letter “C” means that the HNPs were from a new batch. The HNP preparation method has been described in Section 2.1 of Chapter 2.

PMMA and PE were selected as the polymer matrix to prepare polymer-embedded HNPs. The preparation method for PMMA-embedded HNPs and PE-embedded HNPs can be found in Section 2.1 of Chapter 2.

To study the diffusion of solvents in polymer-embedded HNPs, water was used as the model solvent for the diffusion of solvent in PMMA-embedded HNPs; while water, oleyl alcohol and tetrafluorobenzene were used for the diffusion of solvents in PE-embedded HNPs. The contact angles between the solvents and the polymers are shown in Table 6.1.

Table 6.1 Samples used in the solvent diffusion experiments in this study, and the contact angle between the solvents and polymers.

Sample code	Hollow nanoparticle	Polymer matrix	Solvent	Contact angle for solvent and polymers only
HNP50C-PMMA	HNP50C	PMMA	Water	68°-74° [180, 181]
HNP50C-PE	HNP50C	PE	Water	96°-104° [181, 182]
	HNP50C	PE	Oleyl Alcohol	10°-15° *
	HNP50C	PE	Tetrafluorobenzene	Spread*

* The contact angle was measured by Sun Hye Hwang at Seoul National University.

6.2.2 Methods

The setup for the *in-situ* SAXS experiments was the same as that used in Chapter 5. The length of a run for the diffusion experiment was set to be 1530 s in total with data recorded every 1 s in the first 30 s, every 10 s in the next 300 s, and every 60 s in the last 1200 s. The data analysis for the SAXS data was similar to that used in Chapter 5.

Contact angle data was obtained with a drop shape analysis system (Krüss DSA10). To prepare the polymer film for the measurement of contact angle, the polymers, i.e. PMMA and PE, were melted on a hot plate at first. Then, the polymer film was obtained by spreading the melted polymer on a glass slide. The contact angle data was supplied by Sun Hye Hwang at Seoul National University.

SEM images of PMMA-embedded HNPs and PE-embedded HNPs were recorded by Sun Hye Hwang and Jongmin Roh, Seoul National University.

6.3 Theoretical Model for Small Angle X-ray Scattering

The same SAXS theory as that used in Chapter 5, i.e. decoupling approximation, hollow triple-shell sphere model for form factor, and 3-D and 2-D structure factor within Percus-Yevick approximation, was applied to analyze the morphology of PMMA- and PE-embedded HNPs. Details about the theoretical SAXS models can be found in Section 5.3 of Chapter 5.

6.4 Results and Discussion

In Section 6.4.1, the morphology of PMMA-embedded HNPs was studied first, and then the diffusion of water in PMMA-embedded HNPs was analyzed. In Section 6.4.2, the morphology of PE-embedded HNPs was investigated, followed by the analysis of the diffusion of water, oleyl alcohol and tetrafluorobenzene in PE-embedded HNPs.

6.4.1 Solvent Diffusion in Poly(methyl methacrylate)-Embedded Hollow Nanoparticles

6.4.1.1 Morphology of Poly(methyl methacrylate)-Embedded Hollow Nanoparticles

The SEM images of PMMA-embedded HNPs, i.e. HNP50C-PMMA, are shown in Figure 6.1. It can be seen that there is no porous structure in the polymer matrix, *i.e.* the polymer compacted after freeze drying. Rough surface of the polymer matrix can be observed, with small island-like features on the surface. In the high magnification SEM image (Figure 6.1b), such islands can be clearly identified as aggregated HNPs on the surface of the PMMA matrix.

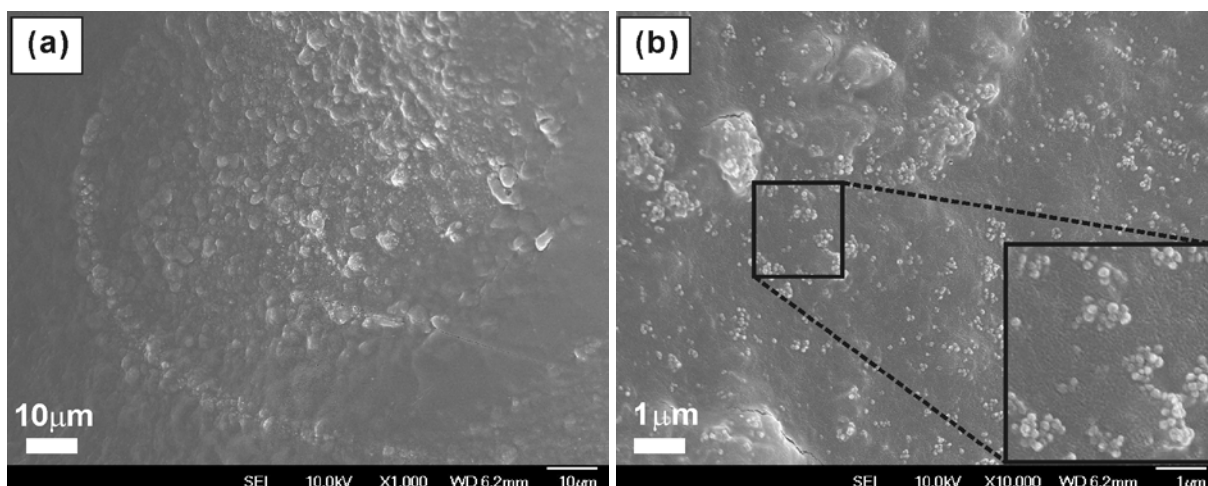


Figure 6.1 SEM images of PMMA-embedded HNP50C. (a) low magnification, (b) higher magnification. The inset in (b) shows the distribution of surface HNP50C. SEM images were supplied by Sun Hye Hwang and Jongmin Roh, SNU.

In order to probe the internal structure of HNP50C-PMMA, the SAXS data of the sample was collected. The same SAXS models as those used in previous chapters are used here: HNP50C distribute not only on the surface of polymer matrix but also in the polymer matrix. For HNP50C distributed on the surface of polymer matrix, an outer polymer layer and an inner polymer layer are assumed to cover the outer surface and inner surface of HNP50C, respectively. For buried HNP50C a polymer layer is assumed to line on the inner surface of HNP50C. The Percus-Yevick approximation for disorder nanoparticles is still used for the structure factor, i.e. 3-D structure factor used for buried HNP50C and 2-D structure factor used for surface HNP50C.

Table 6.2 Size parameters of HNP50C used in this chapter, i.e. HNP50C.

Sample	Outer diameter (nm) (± 0.5)	Inner diameter (nm) (± 0.5)	Shell thickness (nm)	Stand. dev. of outer diameter (σ) ($\pm 2\%$)
HNP50C	57.4	38.2	9.6	11%

Similar fit routine as that used in previous chapters was applied to the experimental SAXS curve of HNP50C-PMMA. Prior to the fit for SAXS curve of HNP50C-PMMA, the size parameters of HNP50C were determined with HNP50C well dispersed in solution and are shown in Table 6.2. These parameters were then fixed during the fit to the SAXS curve of HNP50C-PMMA. The fit result for HNP50C-PMMA is illustrated in Figure 6.2. It can be seen from

Figure 6.2 that the fitted curve overall matches the experimental curve in the q range after the first peak of the experimental curve, i.e. in the range $q > 0.15 \text{ nm}^{-1}$. However, mismatch between the fitted curve and the experimental curve is obviously observed in the q range before the first peak of experimental curve, i.e. in the range $q < 0.15 \text{ nm}^{-1}$. The mismatch between the experimental and the fitted curves in the low q range can be attributed to the fact that the current model is unsuitable to described aggregated HNPs, the sizes of which are bigger.

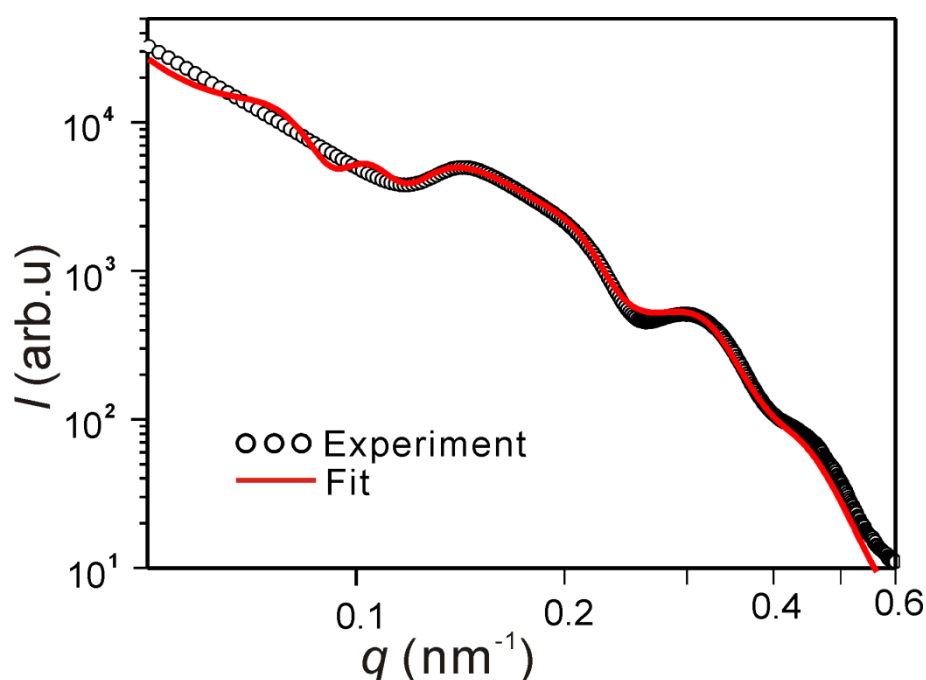


Figure 6.2 Experimental and fitted curves for as prepared PMMA-embedded HNPs.

The fitted parameters for HNP50C-PMMA are summarized in Table 6.3 and Table 6.4. There are several unexpected points in the fitted parameters. Firstly, the packing density of buried HNPs and the surface density of surface HNPs are unexpectedly high. In the case of surface HNPs, the surface density reaches 0.44, a very high surface density which is in conflict with what is observed from SEM images. Secondly, from the fitted electron densities shown in Table 6.4, it can be seen that the electron density of HNP shell is as high as 750 e nm^{-3} , a value very close to the electron density of bulk $\text{TiO}_2/\text{SiO}_2$ which gives a value of 880 e nm^{-3} . The porosity of the HNP shell derived from the fitted electron density is 0.15, much lower

than the more reliable porosity of 0.33 which is the porosity determined in Chapter 3 by the combination of SAXS and nitrogen adsorption-desorption isotherms.

Table 6.3 Fitting results giving morphological parameters of PMMA-embedded HNPs, i.e. HNPs buried in the PMMA matrix and HNPs on matrix surface

Sample	HNPs buried in PMMA matrix			HNPs on surface of PMMA matrix			
	Fraction of all HNPs (± 0.01)	Thickness of inner PMMA (nm) (± 0.5)	Particle packing density (± 0.02)	Fraction of all HNPs (± 0.01)	Thickness of inner PMMA (nm) (± 0.5)	Thickness of outer PMMA (nm) (± 0.5)	Particle surface density (± 0.02)
HNP50C-PMMA	0.85	0.8	0.28	0.15	0.2	53.3	0.44

Table 6.4 Fitting results for electron densities of the inner and outer PMMA layer and of the HNP shell

Sample	Electron density of inner PMMA ($e \text{ nm}^{-3}$) (± 10)	Electron density of HNP shell ($e \text{ nm}^{-3}$) (± 10)	Electron density of outer PMMA ($e \text{ nm}^{-3}$) (± 10)
HNP50C-PMMA	310	750	310*

* This electron density is the same as that of bulk PMMA.

From the fitting results shown above, it is obvious that current SAXS models are inadequate to describe the morphology of PMMA-embedded HNPs, possibly due to the aggregation of HNPs after freeze drying.

6.4.1.2 Diffusion of Water in Poly(methyl methacrylate)-Embedded Hollow Nanoparticles

Since the morphological parameters derived by current SAXS models are unreliable, it is then not possible to carry out further fitting of SAXS curves for the diffusion of solvent in

HNP50C-PMMA. Therefore, in this section, only qualitative analysis is given for the diffusion of solvent in HNP50C-PMMA.

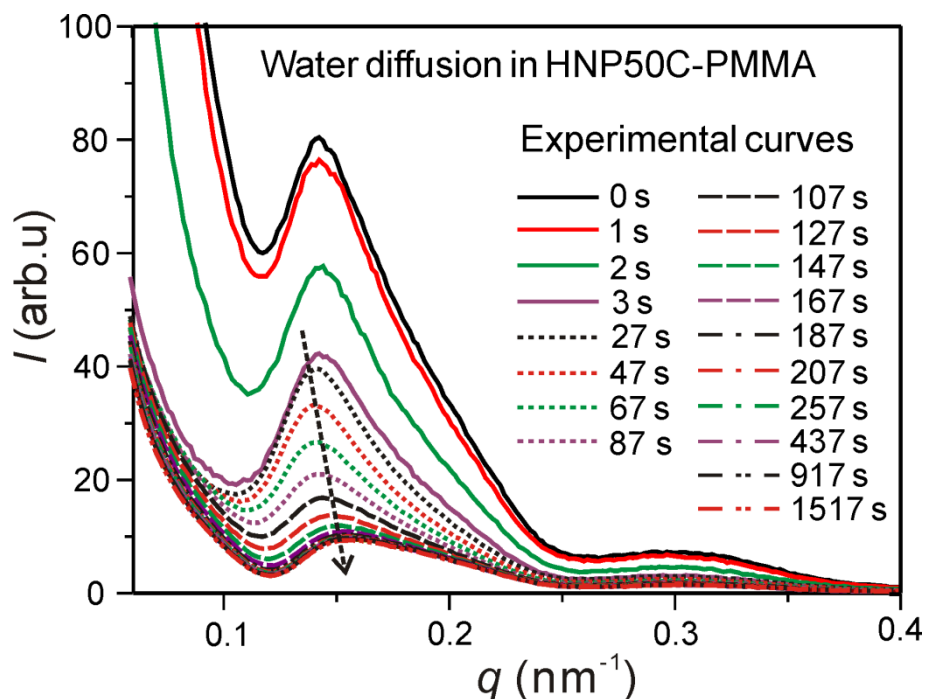


Figure 6.3 Raw experimental SAXS curves for the diffusion of water in PMMA-embedded HNPs, i.e. the sample HNP50C-PMMA. The curves have been scaled according to their exposure time. The arrow with dashed line shows the shift of the scattering peaks.

The experimental SAXS curves for diffusion of water in HNP50C-PMMA are shown in Figure 6.3. In Figure 6.3, it can be seen that the diffusion of water consists of two processes, i.e. a fast process in the first 3 s and a slow process after 3 s. In the fast process, the intensity of curves decreases dramatically, indicating large change in the system. The rapid decrease of the scattering intensity can be attributed to the decrease of the scattering background during the filling of the empty space of the sample and by the filling of surface HNPs with water. The fast change in the scattering intensity also indicates that it is relatively easy for water to wet the PMMA matrix, which is roughly consistent with the contact angle between water and PMMA, i.e. around 70° as is shown in Table 6.1. In the slow process, in the low q range, i.e. $q < 0.1 \text{ nm}^{-1}$, there is very little change in the scattering background. Consequently, changes in the sample would mostly be attributed to the filling of HNPs, and it is possible to discuss the change of the HNPs during solvent diffusion. It is interesting to note that, with the increase of time, the first peak of the scattering curve gradually shifts to high q , i.e. roughly from $q = 0.13$

nm^{-1} to 0.16 nm^{-1} , as is shown by the black dashed arrow in Figure 6.3. The shift of the peak to high q indicates that the overall size of HNPs decreases gradually, which suggests the buried HNPs are being filled. However, due to the aggregation of the HNPs in the system, it is difficult to carry out quantitative analysis of the scattering curves. The sample preparation method must be improved to make this possible.

6.4.2 Solvents Diffusion in Polyethylene-Embedded Hollow Nanoparticles

6.4.2.1 Morphology of Polyethylene-Embedded Hollow Nanoparticles

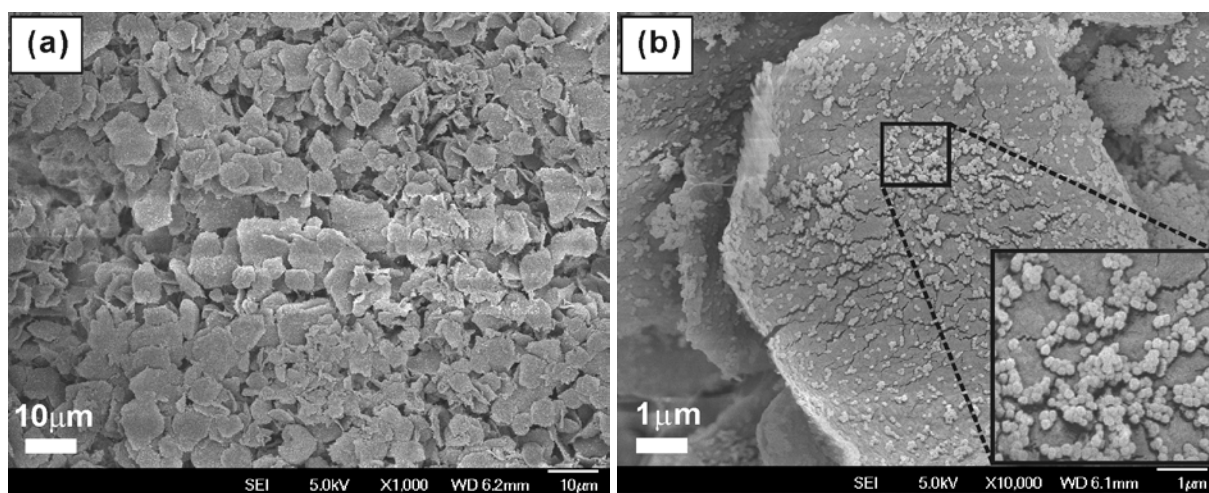


Figure 6.4 SEM images of PE-embedded HNPs. (a) Low magnification, (b) higher magnification with inset showing the distribution of HNPs on the matrix surface. SEM images were supplied by Sun Hye Hwang and Jongmin Roh.

The SEM images of freeze dried HNPs in PE are shown in Figure 6.4. It can be seen that, after freeze drying, the polymer matrix broke down into small pieces of width around $10 \mu\text{m}$. In Figure 6.4b, small cracks in the PE matrix and aggregation of HNPs on the surface of PE matrix are observed.

To obtain information about the internal structure of the PE matrix, similar to the analysis for PMMA-embedded HNPs, we also carried out the fit routine for PE-embedded HNPs. The explanation of the SAXS models for the fit can be found in Section 6.3. The fit result is shown in Figure 6.5. It can be seen from Figure 6.5 that the fit result before the second peak

of the curves, i.e. in the range $q < 0.3 \text{ nm}^{-1}$, is acceptable. However, large mismatch between the experimental and fitted SAXS curves is observed in the range $q > 0.3 \text{ nm}^{-1}$. The mismatch may be due to the aggregation of HNPs in the system, as well as inappropriate form factor models used for HNPs. The discrepancy in the experimental and fitted SAXS curves indicates that the current SAXS model is not suitable to describe the morphology of HNPs freeze dried in PE.

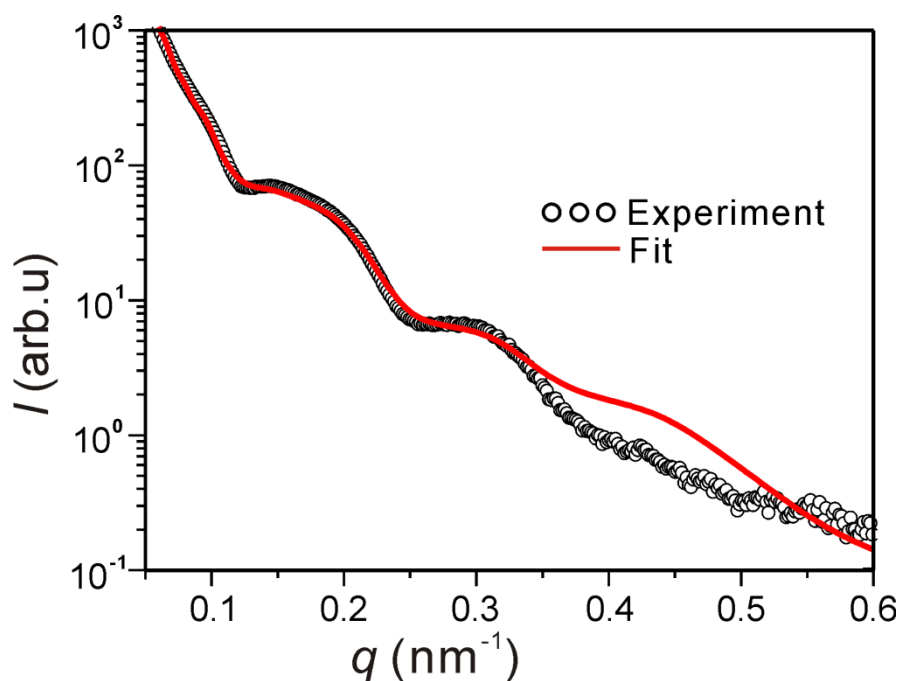


Figure 6.5 Experimental and fitted SAXS curves for as-prepared PE-embedded HNPs.

The fitted parameters for PE-embedded HNPs are summarized in Table 6.5 and 6.6. Since the aggregation of HNPs embedded in PE causes difficulties in analyzing their morphology, the reliability of the fitted parameters is doubtful. Therefore, no further discussion on the fitted parameters is carried out.

Table 6.5 Fitting results giving morphological parameters of PE-embedded HNPs, i.e. HNPs buried in the PE matrix and HNPs on matrix surface

Sample	HNPs buried in PE matrix			HNPs on surface of PE matrix			
	Fraction of all HNPs (± 0.01)	Thickness of inner PE (nm) (± 0.5)	Particle packing density (± 0.02)	Fraction of all HNPs (± 0.01)	Thickness of inner PE (nm) (± 0.5)	Thickness of outer PE (nm) (± 0.5)	Particle surface density (± 0.02)
HNP50C-PE	0.98	13.0	0.28	0.02	11.8	130.7	0.37

Table 6.6 Fitting results for electron densities of the inner and outer PE layer and of the HNP shell

Sample	Electron density of inner PE ($e \text{ nm}^{-3}$) (± 10)	Electron density of HNP shell ($e \text{ nm}^{-3}$) (± 10)	Electron density of outer PE ($e \text{ nm}^{-3}$) (± 10)
HNP50C-PE	250	540	330*

* This electron density is the same as that of bulk PE.

6.4.2.2 Diffusion of Water in Polyethylene-Embedded Hollow Nanoparticles

Since it is difficult to determine the morphological parameters of HNPs freeze dried in PE, only qualitative analysis is given in the following for the diffusion of solvents in PE-embedded HNPs.

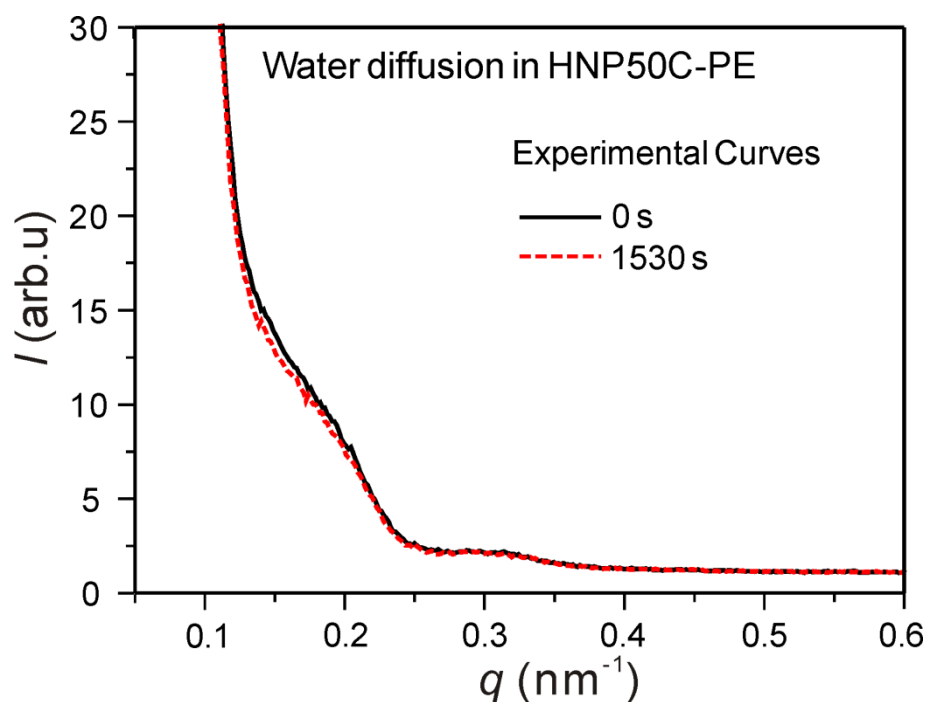


Figure 6.6 Experimental SAXS curves for the diffusion of water in PE-embedded HNPs, i.e. the sample HNP50C-PE. The curves have been scaled according to their exposure time.

From Figure 6.6 for the diffusion of water in PE-embedded HNPs, i.e. HNP50C-PE, it can be seen that there is nearly no change in the scattering curves during diffusion. Since the contact angle between water and PE can be as high as 104° , the invariance of the scattering curves may indicate that water was not able to wet the PE matrix at all.

6.4.2.3 Diffusion of Oleyl Alcohol in Polyethylene-Embedded Hollow Nanoparticles

In the second test for the diffusion of solvent in PE-embedded HNPs, oleyl alcohol was chosen as the model solvent. The reason for choosing oleyl alcohol was that this unsaturated alcohol can give a lower contact angle than that of water. From the measured contact angle shown in Table 6.1, the contact angle between oleyl alcohol and PE is roughly 15° , while that between water and PE can reach 104° . Hence, different diffusion phenomenon may be observed for the diffusion of oleyl alcohol in PE-embedded HNPs.

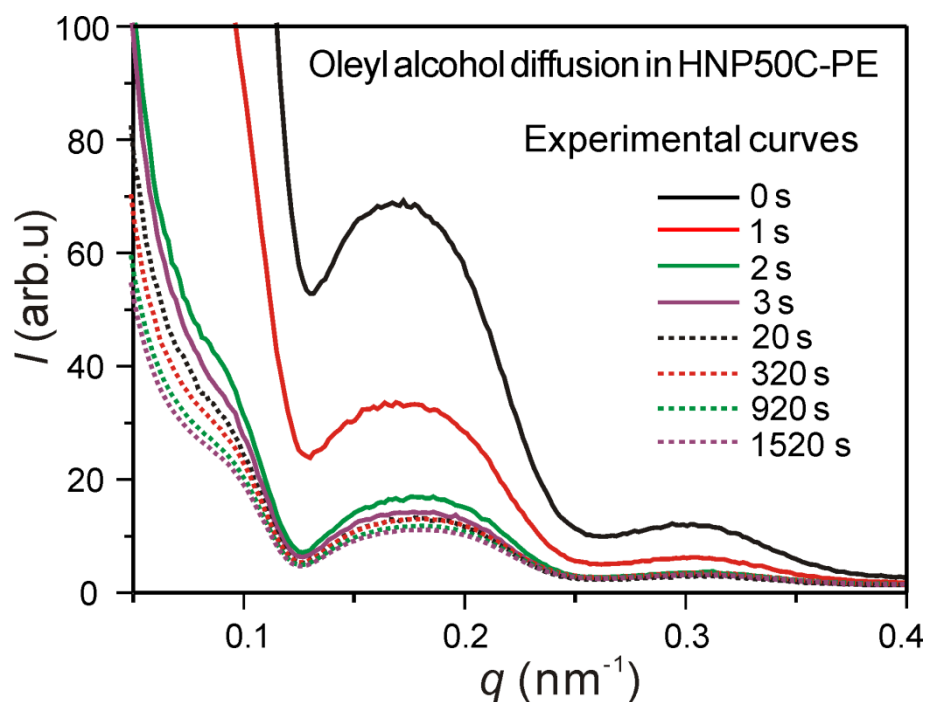


Figure 6.7 Experimental SAXS curves for the diffusion of oleyl alcohol in PE-embedded HNPs. The curves have been scaled according to their exposure time.

The experimental SAXS curves for the diffusion of oleyl alcohol in HNP50C-PE are shown in Figure 6.7. In Figure 6.7, it can be seen that the diffusion of oleyl alcohol also consists of two processes, i.e. a fast process in the first 2 s and a slow process after 2 s. In the fast process, the intensity of curves decreases rapidly, indicating large change in the system. The rapid decrease of the intensity is due to the filling of the empty space in the sample and the filling of surface HNPs. The fast change in the scattering intensity is understandable since it is very easy for oleyl alcohol to wet the PE matrix. In the slow process, the decrease in the scattering intensity carries on slowly. The slow decrease of the intensity in low q range may arise from the possible dissolving of PE in oleyl alcohol and hence decrease of the scattering background. Also, the gradual decrease of the scattering intensity indicates the scattering contrast of the whole system is decreasing, which may be caused by possible filling of small gaps or voids in the PE matrix. It is noted that a shoulder at around $q = 0.1 \text{ nm}^{-1}$ in the scattering curves is observed, which indicates a strong interaction between HNPs in this sample hence the structure factor could be very complex.

6.4.2.4 Diffusion of Tetrafluorobenzene in Polyethylene-Embedded Hollow Nanoparticles

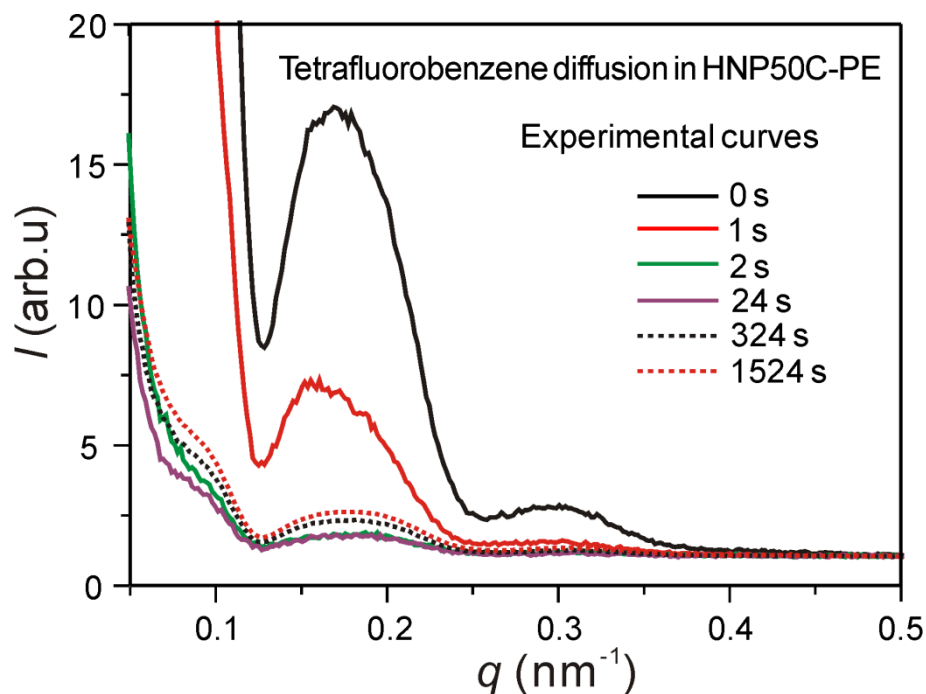


Figure 6.8 Experimental SAXS curves for the diffusion of tetrafluorobenzene in PE-embedded HNPs. The curves have been scaled according to their exposure time.

In the third test for the diffusion of solvent in PE-embedded HNPs, tetrafluorobenzene was chosen as the model solvent. The reason for choosing tetrafluorobenzene was that this non-polar solvent can wet the PE matrix very easily and it may give new diffusion phenomenon.

The experimental SAXS curves for the diffusion of tetrafluorobenzene in HNP50C-PE are shown in Figure 6.8. It can be seen that the diffusion of tetrafluorobenzene also consists of two processes, i.e. a fast process in the first 2 s and a slow process after 2 s. In the fast process, the intensity of curves decreases rapidly. This is attributed to the fast filling of the empty space in the sample and the filling of surface HNPs, since it is very easy for tetrafluorobenzene to wet the PE matrix. In the slow process, the intensity of the scattering curves decreases at first, but increases slightly later. The gradual decrease of the scattering intensity may be due to gradual filling of small gaps or voids in the PE matrix by tetrafluorobenzene and hence gradual decrease of the scattering contrast, while the slight

increase of the intensity may be due to the possible evaporation of solvent causing increase of scattering contrast after long exposure of the solvent to X-ray beam.

6.5 Conclusions

In this study, different solvent diffusion cases were investigated by *in-situ* SAXS, i.e. diffusion of water into PMMA-embedded HNP system and diffusion of water, oleyl alcohol and tetrafluorobenzene into PE-embedded HNP system, respectively. In the direct observation by SEM of the morphology of as prepared PMMA-embedded HNPs and PE-embedded HNP, HNPs are found to aggregate on the surface of polymer matrix after freeze drying. This aggregation of HNPs in the freeze dried samples hinders the applicability of our SAXS models since it introduces complex interaction among HNPs and hence complex structure factor. The failure of our SAXS models for the analysis to the morphology of PMMA-embedded HNPs and PE-embedded HNPs indicates the sample preparation method needs to be improved to avoid aggregation of HNPs before more quantitative analyse by SAXS is made. In all cases, except the diffusion of water in PE-embedded HNPs, two diffusion processes were observed, i.e. a fast process arising from the fast filling of outer empty space of the sample and the surface HNPs by solvent and a slow process due to the slow filling of buried HNPs or small gaps in the polymer matrix. The results in this chapter indicate that *in-situ* SAXS is a valid method to monitor the diffusion of solvents into different polymer-embedded HNP systems. However, to obtain quantitative results for solvent diffusion, the SAXS models and sample preparation methods need to be considered carefully, especially for freeze dried samples with aggregated HNPs.

Future Work

In this project, we were able to determine the morphology of and diffusion of solvents in polymer-embedded HNP systems mainly by small angle scattering methods.

However, even though the SAXS models including both surface HNP model and buried HNP model were successfully applied to determine the morphology of PEO-embedded HNPs, their application to study the morphology of PMMA- and PE-embedded HNP systems was hindered due to the aggregation of HNPs. Therefore, in the future, two aspects of work can be done to solve this problem. Firstly, the SAXS models have to be improved by including an intermediate model between the surface HNP model and buried HNP model. This would allow more realistic description of the polymer-embedded HNP systems. Secondly, the sample preparation method has to be improved to avoid aggregation of HNPs. This may be done by improving the compatibility of the polymer and HNPs in the same solvent.

For the PEO-embedded HNP systems, it would be interesting to study how their morphology changes if the sample preparation condition is changed, e.g. using different experimental parameters during freeze drying. The change of morphology may result in different diffusion behaviour of the same solvent. Moreover, the diffusion of solvents with different molecular weight and polarity can be studied for the PEO-embedded HNP system. Further, it is worth investigating the drug loading and release efficiency of the PEO-embedded HNP gel, since only pure polymer gel without inclusion of nanoparticles was tested in the literature.

Besides drug delivery, other applications of HNPs and their polymer composites can be studied, e.g. fluid filter, gas sensor and membrane for sea water desalination. For example, the adsorption kinetics of gas in HNPs is important for their application in gas sensors. Also, compared to traditional polymer membrane, the mechanism for the enhancement of sea water desalination in the porous nanoparticles/polymer composite membrane is not clear. Those applications are all related to the diffusion of fluid into the porous structure of HNP and their polymer composites. Therefore, for those future studies, *in-situ* small angle scattering can be used again to determine the diffusion kinetics of fluids in HNPs and their polymer composites.

Publications and Conferences

Publications List

- [1] **Zhi Hong Chen**, Chanhoi Kim, Xiang-bing Zeng, Sun Hye Hwang, Jyongsik Jang and Goran Ungar, *Characterizing size and porosity of hollow nanoparticles: SAXS, SANS, TEM, DLS, and adsorption isotherms compared*, Langmuir, 2012, 28, 15350-15361.
- This paper was highlighted in the annual review of Diamond Light Source, UK. See: *Ceramic hollow nanoparticles - hollow spheres or nano-baskets?*, Diamond light source 2012/2013 Annual Review, Page 58-59.
- [2] **Zhi Hong Chen**, Sun Hye Hwang, Xiang-bing Zeng, Jongmin Roh, Jyongsik Jang and Goran Ungar, *SAXS characterization of polymer-embedded hollow nanoparticles and of their shell porosity*, Journal of Applied Crystallography, 2013,46,1654-1664.
- [3] **Zhi Hong Chen**, Sun Hye Hwang, Xiang-bing Zeng, Jongmin Roh, Jyongsik Jang and Goran Ungar, *In-situ small angle X-ray scattering study of solvent diffusion in polymer-embedded hollow nanoparticles*, to be submitted to Journal of Physical Chemistry Letters, 2013.

Conferences List

- [1] **Zhi Hong Chen**, Xiangbing Zeng, Goran Ungar, Sun Hye Hwang, Chanhoi Kim, Jyongsik Jang, Gemma Newby, *Morphology Characterization and In-Situ Small Angle X-ray Scattering Study of Materials Transport through Hollow Nanoparticles for Drug Delivery*, International Conference on Nanotechnology in Medicine, 2012, University of College London, London.
- [2] **Zhi Hong Chen**, Xiangbing Zeng, Goran Ungar, Chanhoi Kim, Sun Hye Hwang, Jyongsik Jang, *In-situ small angle X-ray scattering study of solvent diffusion through*

hollow nanoparticles for drug delivery, 15th International Small Angle Scattering Conference, 2012, Sydney.

[3] **Zhi Hong Chen**, Xiangbing Zeng, Goran Ungar, Sun Hye Hwang, Jongmin Roh, Jyongsik Jang, *Morphology of and solvent diffusion in polymer-embedded hollow nanoparticles by in-situ small angle X-ray scattering*, 2nd S4SAS User meeting and Workshop organized by Diamond light source, 2013, Sheffield.

Appendix

A1. Analytic Expression for SAXS Intensity of Hollow Nanoparticles

Within the decoupling approximation, the scattering intensity is expressed by

$$I(q) = \langle |F(q)|^2 \rangle + \langle |F(q)|^2 \rangle \cdot [S(q) - 1] \quad (\text{A.1})$$

Here we give the analytical expression of each term in the above equation for the scattering intensity of hollow spheres with weak interaction.

$$\begin{aligned} \langle |F(q)|^2 \rangle = & g1 \cdot (1 - h1 \cdot k3 - h2 \cdot k4 - h3 \cdot k5 + h4 \cdot k6 \\ & - h5 \cdot k15 - h5 \cdot k16 + h6 + h6 \cdot k13 \\ & + h7 + h7 \cdot k14 - k7 - k8 - k11 + k12) \end{aligned} \quad (\text{A.2})$$

$$\langle |F(q)| \rangle^2 = g1 \cdot (h1 \cdot k9 - h2 \cdot k10 - k1 + k2)^2 \quad (\text{A.3})$$

$$S(q) = \frac{4\pi R_0^3}{4\pi R_0^3 - 3\eta \cdot C(q)} = \frac{1}{1 - (\alpha \cdot s1 + \beta \cdot s2 + \delta \cdot s3)} \quad (\text{A.4})$$

where

$$g1 = \frac{16\pi^2 \Delta\rho^2}{q^6}$$

$$h1 = qr_0$$

$$h2 = qR_0$$

$$h3 = (R_0 - r_0)q$$

$$h4 = (R_0 + r_0)q$$

$$h5 = q^2 r_0 R_0 \frac{z+2}{z+1}$$

$$h6 = \frac{q^2 r_0^2}{2} \cdot \frac{z+2}{z+1}$$

$$h7 = \frac{q^2 R_0^2}{2} \cdot \frac{z+2}{z+1}$$

$$k1 = \frac{\sin[(z+1) \arctan(qr_0 / (z+1))]}{(1 + q^2 r_0^2 / (z+1)^2)^{(z+1)/2}}$$

$$k2 = \frac{\sin[(z+1) \arctan(qR_0 / (z+1))]}{(1 + q^2 R_0^2 / (z+1)^2)^{(z+1)/2}}$$

$$k3 = \frac{\sin[(z+2) \arctan(2qr_0 / (z+1))]}{(1 + 4q^2 r_0^2 / (z+1)^2)^{(z+2)/2}}$$

$$k4 = \frac{\sin[(z+2) \arctan(2qR_0 / (z+1))]}{(1 + 4q^2 R_0^2 / (z+1)^2)^{(z+2)/2}}$$

$$k5 = \frac{\sin[(z+2) \arctan(q(R_0 - r_0) / (z+1))]}{(1 + q^2 (R_0 - r_0)^2 / (z+1)^2)^{(z+2)/2}}$$

$$k6 = \frac{\sin[(z+2) \arctan(q(R_0 + r_0) / (z+1))]}{(1 + q^2 (R_0 + r_0)^2 / (z+1)^2)^{(z+2)/2}}$$

$$k7 = \frac{1}{2} \cdot \frac{\cos[(z+1) \arctan(2qr_0 / (z+1))]}{(1 + 4q^2 r_0^2 / (z+1)^2)^{(z+1)/2}}$$

$$k8 = \frac{1}{2} \cdot \frac{\cos[(z+1) \arctan(2qR_0 / (z+1))]}{(1 + 4q^2 R_0^2 / (z+1)^2)^{(z+1)/2}}$$

$$k9 = \frac{\cos[(z+2) \arctan(qr_0 / (z+1))]}{(1 + q^2 r_0^2 / (z+1)^2)^{(z+2)/2}}$$

$$k10 = \frac{\cos[(z+2) \arctan(qR_0 / (z+1))]}{(1+q^2 R_0^2 / (z+1)^2)^{(z+2)/2}}$$

$$k11 = \frac{\cos[(z+1) \arctan(q(R_0 - r_0) / (z+1))]}{(1+q^2 (R_0 - r_0)^2 / (z+1)^2)^{(z+1)/2}}$$

$$k12 = \frac{\cos[(z+1) \arctan(q(R_0 + r_0) / (z+1))]}{(1+q^2 (R_0 + r_0)^2 / (z+1)^2)^{(z+1)/2}}$$

$$k13 = \frac{\cos[(z+3) \arctan(2qr_0 / (z+1))]}{(1+4q^2 r_0^2 / (z+1)^2)^{(z+3)/2}}$$

$$k14 = \frac{\cos[(z+3) \arctan(2qR_0 / (z+1))]}{(1+4q^2 R_0^2 / (z+1)^2)^{(z+3)/2}}$$

$$k15 = \frac{\cos[(z+3) \arctan(q(R_0 - r_0) / (z+1))]}{(1+q^2 (R_0 - r_0)^2 / (z+1)^2)^{(z+3)/2}}$$

$$k16 = \frac{\cos[(z+3) \arctan(q(R_0 + r_0) / (z+1))]}{(1+q^2 (R_0 + r_0)^2 / (z+1)^2)^{(z+3)/2}}$$

$$\alpha = -(1+2\eta)^2 / (1-\eta)^4$$

$$\beta = 6\eta(1+0.5\eta)^2 / (1-\eta)^4$$

$$\delta = -0.5\eta(1+2\eta)^2 / (1-\eta)^4$$

$$s1 = \frac{3\eta}{q^3 R_0^3} \cdot (\sin 2qR_0 - 2qR_0 \cos 2qR_0)$$

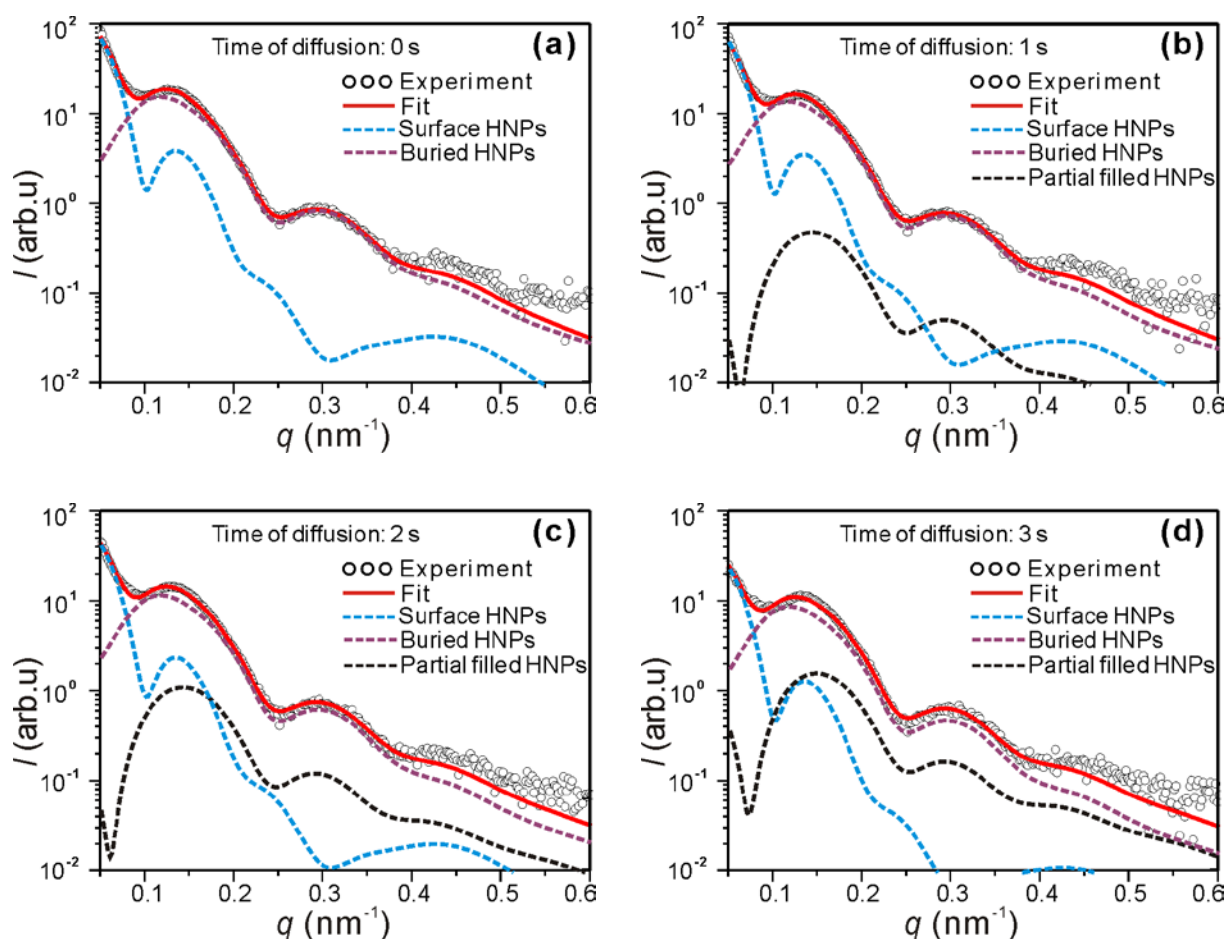
$$s2 = \frac{3\eta}{2q^4 R_0^4} \cdot (4qR_0 \sin 2qR_0 - 4q^2 R_0^2 \cos 2qR_0 + 2 \cos 2qR_0 - 2)$$

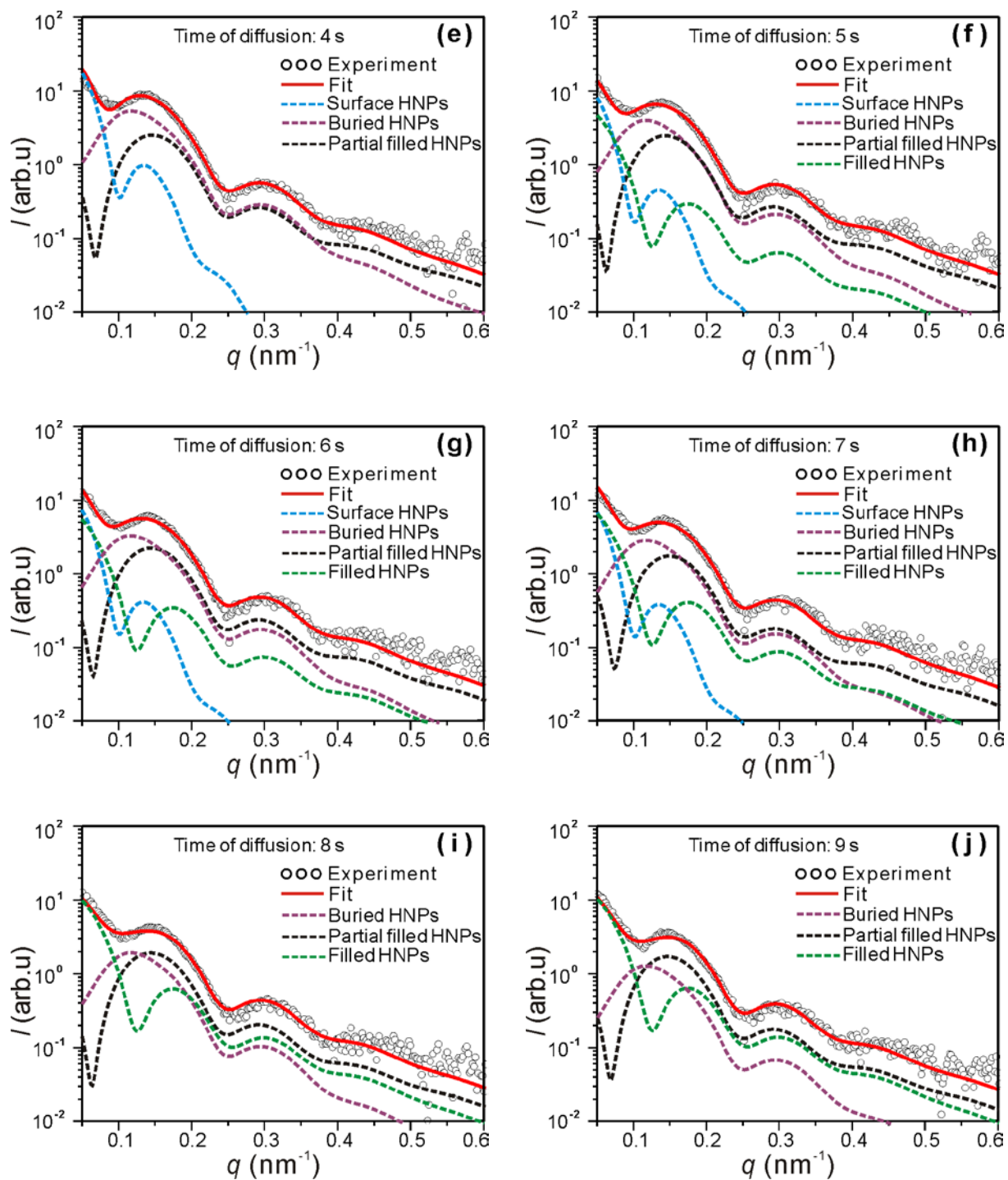
$$s3 = \frac{3\eta}{8q^6 R_0^6} \cdot (32q^3 R_0^3 \sin 2qR_0 - 16q^4 R_0^4 \cos 2qR_0 - 48qR_0 \sin 2qR_0 + 48q^2 R_0^2 \cos 2qR_0 - 24 \cos 2qR_0 + 24)$$

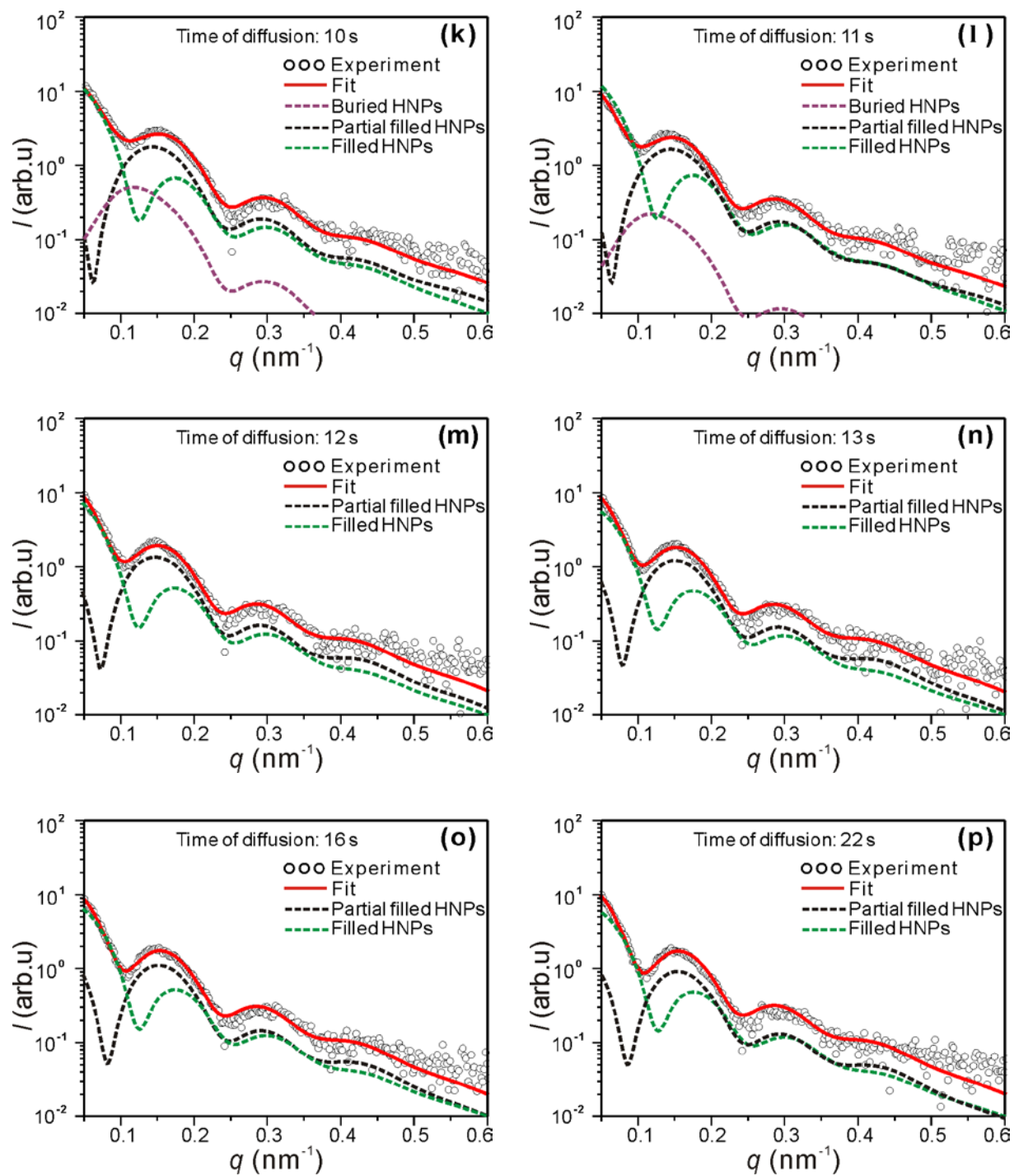
In the above equations, r_0 and R_0 is the inner and outer radii of hollow nanoparticles, respectively, z is a parameter in Schulz distribution, η is the volume fraction of the particles, and q is the scattering vector.

A2. Fit Details for diffusion of solvent in PEO-Embedded Hollow Nanoparticles

Figure A.1 illustrates the experimental and fitted curves for the diffusion of liquid low molecular PEO in PEO-embedded HNPs, together with the calculated curves from each model. Due to undistinguishable of experimental curves in the finishing stage of diffusion, some of the experimental curves in the later stage are neglected and not shown here.







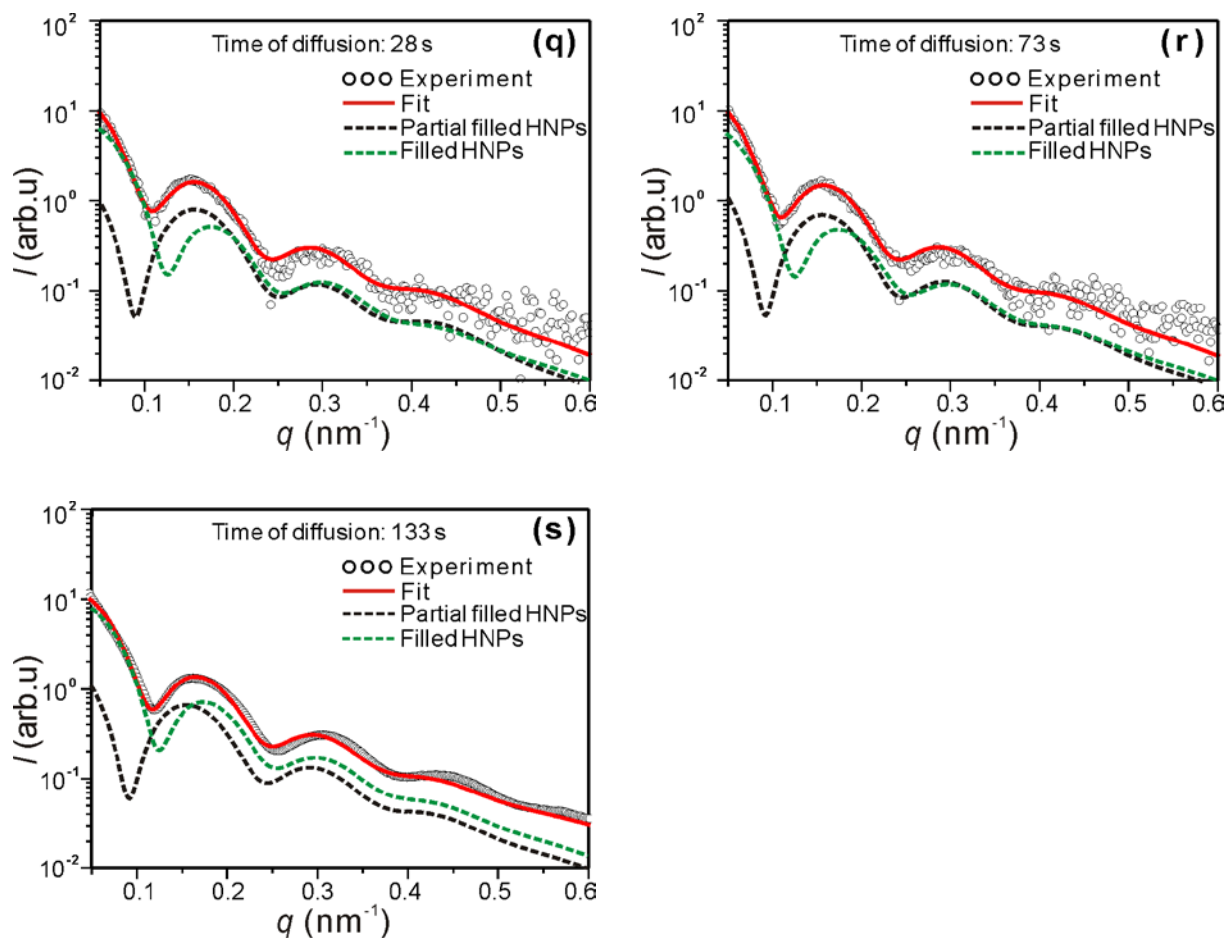


Figure A.1 Illustration of the experimental (open circles) and fitted (red solid line) SAXS curves for solvent diffusion. The fitted curve is the combination of the curves from the four SAXS models, i.e. surface HNPs (blue dashed line), buried HNPs (purple dashed line), partially filled HNPs (black dashed line), and filled HNPs (green dashed line).

A3. Solvent diffusion experiments with small angle neutron scattering

In this project, we also tested the diffusion of solvent in and out of hollow nanoparticles (HNPs) by small angle neutron scattering. We investigated the diffusion behaviour of different solvents with various molecular size and polarity. We used the stopped flow cell at the LOQ station, ISIS, for immediate mixing of the sample with the surrounding solvent. In those experiments, it was not possible to distinguish the timescale for the outer solvent

reaching the HNPs and diffusing into the HNPs. It was found that the diffusion speed of all the tested solvents into HNPs was too fast to be observed by SANS.

Table A.1 List of experiments for solvent diffusion tested by SANS

Number	Release system	Surrounding solvent	Result
1	9wt%HNP50 + D ₂ O	H ₂ O	Release too fast
2	17wt%HNP50 + D ₂ O	H ₂ O	Release too fast
3	30wt%HNP50 + D ₂ O	H ₂ O	Release too fast; Sample too viscous
4	20wt%HNP50 + H ₂ O	D ₂ O	Release too fast
5	30wt%HNP50 + H ₂ O	D ₂ O	Release too fast; Sample too viscous
6	17wt%HNP50 + D ₂ O	Dimethyl sulfoxide	Release too fast
7	30wt%HNP50 + D ₂ O	Ethylene glycol	Release too fast
8	30wt%HNP50 + D ₂ O	Glycerol	Glycerol too viscous

*Here, 9wt%HNP50 + D₂O means 9wt% of HNP50 was dissolved in D₂O, which was then used as the solvent loaded sample. Others have the same meaning.

References

- [1] X. W. Lou, L. A. Archer and Z. Yang, *Adv. Mater.* **2008**, *20*, 3987-4019.
- [2] K. An and T. Hyeon, *Nano Today* **2009**, *4*, 359-373.
- [3] G. D. Fu, G. L. Li, K. G. Neoh and E. T. Kang, *Prog. Polym. Sci.* **2011**, *36*, 127-167.
- [4] E. O. Kirkendall, *Trans. AIME* **1942**, *147*, 104-110.
- [5] Y. D. Yin, R. M. Rioux, C. K. Erdonmez, S. Hughes, G. A. Somorjai and A. P. Alivisatos, *Science* **2004**, *304*, 711-714.
- [6] S. Peng and S. H. Sun, *Angew. Chem. Int. Edit.* **2007**, *46*, 4155-4158.
- [7] A. Cabot, V. F. Puentes, E. Shevchenko, Y. Yin, L. Balcells, M. A. Marcus, S. M. Hughes and A. P. Alivisatos, *J. Am. Chem. Soc.* **2007**, *129*, 10358-10360.
- [8] A. Cabot, R. K. Smith, Y. D. Yin, H. M. Zheng, B. M. Reinhard, H. T. Liu and A. P. Alivisatos, *ACS NANO* **2008**, *2*, 1452-1458.
- [9] X. Liang, X. Wang, Y. Zhuang, B. Xu, S. M. Kuang and Y. D. Li, *J. Am. Chem. Soc.* **2008**, *130*, 2736-2737.
- [10] E. V. Shevchenko, M. I. Bodnarchuk, M. V. Kovalenko, D. V. Talapin, R. K. Smith, S. Aloni, W. Heiss and A. P. Alivisatos, *Adv. Mater.* **2008**, *20*, 4323-4329.
- [11] Y. G. Sun, B. T. Mayers and Y. N. Xia, *Nano Lett.* **2002**, *2*, 481-485.
- [12] Y. G. Sun and Y. N. Xia, *Science* **2002**, *298*, 2176-2179.
- [13] H. P. Liang, H. M. Zhang, J.S.Hu, Y. G. Guo, L. J. Wan and C.L.Bai, *Angew. Chem. Int. Edit.* **2004** *43* 1540-1543.
- [14] H. P. Liang, L. J. Wan, C. L. Bai and L. Jiang, *J. Phys. Chem. B* **2005**, *109*, 7795-7800.
- [15] H. P. Liang, Y. G. Guo, H. M. Zhang, J. S. Hu, L. J. Wan and C. L. Bai, *Chem. Commun.* **2004**, 1496-1497.
- [16] W. Ostwald, *Z. Phys. Chem.* **1897**, *22*, 289-302.
- [17] X. W. Lou, Y. Wang, C. L. Yuan, J. Y. Lee and L. A. Archer, *Adv. Mater.* **2006**, *18*, 2325-2329.
- [18] H. X. Li, Z. F. Bian, J. Zhu, D. Q. Zhang, G. S. Li, Y. N. Huo, H. Li and Y. F. Lu, *J. Am. Chem. Soc.* **2007**, *129*, 8406-8407.
- [19] J. J. Teo, Y. Chang and H. C. Zeng, *Langmuir* **2006**, *22*, 7369-7377.
- [20] J. Li and H. C. Zeng, *J. Am. Chem. Soc.* **2007**, *129*, 15839-15847.

- [21] C. Luo and D. F. Xue, *Langmuir* **2006**, *22*, 9914-9918.
- [22] Y. Wang, Q. S. Zhu and H. G. Zhang, *Chem. Commun.* **2005**, 5231-5233.
- [23] J. G. Yu, H. G. Yu, H. T. Guo, M. Li and S. Mann, *Small* **2008**, *4*, 87-91.
- [24] Y. Piao, A. Burns, J. Kim, U. Wiesner and T. Hyeon, *Adv. Funct. Mater.* **2008**, *18*, 3745-3758.
- [25] J. Kim, Y. Piao and T. Hyeon, *Chem. Soc. Rev.* **2009**, *38*, 372-390.
- [26] J. Lu, M. Liong, J. I. Zink and F. Tamanoi, *Small* **2007**, *3*, 1341-1346.
- [27] Z. Z. Li, L. X. Wen, L. Shao and J. F. Chen, *J. Control. Release* **2004**, *98*, 245-254.
- [28] J. Yang, J. Lee, J. Kang, K. Lee, J. S. Suh, H. G. Yoon, Y. M. Huh and S. Haam, *Langmuir* **2008**, *24*, 3417-3421.
- [29] H. B. Na, I. C. Song and T. Hyeon, *Adv. Mater.* **2009**, *21*, 2133-2148.
- [30] S. H. Hu, S. Y. Chen, D. M. Liu and C. S. Hsiao, *Adv. Mater.* **2008**, *20*, 2690-2695.
- [31] Y. Zhao, L. N. Lin, Y. Lu, S. F. Chen, L. A. Dong and S. H. Yu, *Adv. Mater.* **2010**, *22*, 5255-5259.
- [32] J. Chen, F. Saeki, B. J. Wiley, H. Cang, M. J. Cobb, Z. Y. Li, L. Au, H. Zhang, M. B. Kimmey, X. D. Li and Y. Xia, *Nano Lett.* **2005**, *5*, 473-477.
- [33] J. Y. Chen, B. Wiley, Z. Y. Li, D. Campbell, F. Saeki, H. Cang, L. Au, J. Lee, X. D. Li and Y. N. Xia, *Adv. Mater.* **2005**, *17*, 2255-2261.
- [34] S. W. Kim, M. Kim, W. Y. Lee and T. Hyeon, *J. Am. Chem. Soc.* **2002**, *124*, 7642-7643.
- [35] Y. G. Li, P. Zhou, Z. H. Dai, Z. X. Hu, P. P. Sun and J. C. Bao, *New J. Chem.* **2006**, *30*, 832-837.
- [36] Z. Y. Bai, L. Yang, J. Zhang, L. Li, J. Lv, C. G. Hu and J. G. Zhou, *Catal. Commun.* **2010**, *11*, 919-922.
- [37] C. J. Martinez, B. Hockey, C. B. Montgomery and S. Semancik, *Langmuir* **2005**, *21*, 7937-7944.
- [38] B. X. Li, Y. Xie, M. Jing, G. X. Rong, Y. C. Tang and G. Z. Zhang, *Langmuir* **2006**, *22*, 9380-9385.
- [39] H. G. Zhang, Q. S. Zhu, Y. Zhang, Y. Wang, L. Zhao and B. Yu, *Adv. Funct. Mater.* **2007**, *17*, 2766-2771.
- [40] H.-J. Kim, K.-I. Choi, A. Pan, I.-D. Kim, H.-R. Kim, K.-M. Kim, C. W. Na, G. Cao and J.-H. Lee, *J. Mater. Chem.* **2011**, *21*, 6549-6555.

- [41] S.-J. Kim, I.-S. Hwang, C. W. Na, I.-D. Kim, Y. C. Kang and J.-H. Lee, *J. Mater. Chem.* **2011**, *21*, 18560-18567.
- [42] H. R. Kim, K. I. Choi, K. M. Kim, I. D. Kim, G. Z. Cao and J. H. Lee, *Chem. Commun.* **2010**, *46*, 5061-5063.
- [43] X. W. Lou, C. M. Li and L. A. Archer, *Adv. Mater.* **2009**, *21*, 2536-2539.
- [44] H. Ma, F. Cheng, J. Y. Chen, J. Z. Zhao, C. S. Li, Z. L. Tao and J. Liang, *Adv. Mater.* **2007**, *19*, 4067-4070.
- [45] H. Kim and J. Cho, *Chem. Mater.* **2008**, *20*, 1679-1681.
- [46] B. Li, G. Rong, Y. Xie, L. Huang and C. Feng, *Inorg. Chem.* **2006**, *45*, 6404-6410.
- [47] R.-J. Roe, *Methods of x-ray and neutron scattering in polymer science*. Oxford University Press: Oxford, **2000**.
- [48] A. Vrij, *J. Chem. Phys.* **1979**, *71*, 3267-3270.
- [49] L. Blum and G. Stell, *J. Chem. Phys.* **1979**, *71*, 42-46.
- [50] J. J. Salacuse and G. Stell, *J. Chem. Phys.* **1982**, *77*, 3714-3725.
- [51] M. Kotlarchyk and S. H. Chen, *J. Chem. Phys.* **1983**, *79*, 2461-2469.
- [52] J. S. Pedersen, *J. Appl. Cryst.* **1994**, *27*, 595-608.
- [53] C. Revenant, F. Leroy, R. Lazzari, G. Renaud and C. R. Henry, *Phys. Rev. B* **2004**, *69*, 1-17.
- [54] J. S. Pedersen, *Phys. Rev. B* **1993**, *47*, 657-665.
- [55] D. Babonneau, F. Pailloux, J. P. Eymery, M. F. Denanot, P. Guerin, E. Fonda and O. Lyon, *Phys. Rev. B* **2005**, *71*, 1-12.
- [56] F. Leroy, R. Lazzari and G. Renaud, *Acta Crystallogr. Sec. A* **2004**, *60*, 565-581.
- [57] R. Lazzari, F. Leroy and G. Renaud, *Phys. Rev. B* **2007**, *76* 1-14.
- [58] C. Revenant, F. Leroy, G. Renaud, R. Lazzari, A. Letoublon and T. Madey, *Surf. Sci.* **2007**, *601*, 3431-3449.
- [59] D. Babonneau, *J. Appl. Cryst.* **2010**, *43*, 929-936.
- [60] J. S. Pedersen, *Adv. Colloid Interface Sci.* **1997**, *70*, 171-210.
- [61] R. Lazzari, *J. Appl. Cryst.* **2002**, *35*, 406-421.
- [62] S. R. Kline, *J. Appl. Cryst.* **2006**, *39*, 895-900.
- [63] I. Livsey and R. H. Ottewill, *Adv. Colloid. Interfac.* **1991**, *36*, 173-184.
- [64] R. Pons, M. Valiente and G. Montalvo, *Langmuir* **2010**, *26*, 2256-2262.

- [65] R. T. Zhang, P. A. Marone, P. Thiyagarajan and D. M. Tiede, *Langmuir* **1999**, *15*, 7510-7519.
- [66] M. Reufer, H. Dietsch, U. Gasser, A. Hirt, A. Menzel and P. Schurtenberger, *J. Phys. Chem. B* **2010**, *114*, 4763-4769.
- [67] G. Bryant, T. Mortensen, S. Henderson, S. Williams and W. van Meegen, *J. Colloid Interf. Sci.* **1999**, *216*, 401-408.
- [68] J. S. Pedersen and C. Svaneborg, *Curr. Opin. Colloid Interface Sci.* **2002**, *7*, 158-166.
- [69] J. Kohlbrecher, J. Buitenhuis, G. Meier and M. P. Lettinga, *J. Chem. Phys.* **2006**, *125*, 1-9.
- [70] X. B. Zeng, Y. S. Liu and M. Imperor-Clerc, *J. Phys. Chem. B* **2007**, *111*, 5174-5179.
- [71] Z. H. Chen, C. Kim, X.-b. Zeng, S. H. Hwang, J. Jang and G. Ungar, *Langmuir* **2012**, *28*, 15350-15361.
- [72] C. B. He, A. M. Donald, M. F. Butler and O. Diat, *Polymer* **1998**, *39*, 659-667.
- [73] V. Degiorgio and M. Corti, *In physics of amphiphiles: micelles, vesicles and microemulsions*. North Holland Physics Publishing Company: Amsterdam, **1985**.
- [74] M. Nayeri, M. Zackrisson and J. Bergenholtz, *J. Phys. Chem. B* **2009**, *113*, 8296-8302.
- [75] S. Förster and C. Burger, *Macromolecules* **1998**, *31*, 879-891.
- [76] Z. H. Chen, S. H. Hwang, X.-b. Zeng, J. Roh, J. Jang and G. Ungar, *J. Appl. Cryst.* **2013**, *46*, 1654-1664.
- [77] X. Li, K.-H. Liu, B. Wu, L. E. Sanchez-Diaz, G. S. Smith and W.-R. Chen, *J. Appl. Cryst* **2013**, *46*, 1551-1557.
- [78] A. Halperin, *Macromolecules* **1987**, *20*, 2943-2946.
- [79] J. S. Pedersen and M. C. Gerstenberg, *Macromolecules* **1996**, *29*, 1363-1365.
- [80] J. S. Pedersen, *J. Chem. Phys.* **2001**, *114*, 2839-2846.
- [81] I. Berndt, J. S. Pedersen and W. Richtering, *J. Am. Chem. Soc.* **2005**, *127*.
- [82] I. Berndt, J. S. Pedersen, P. Lindner and W. Richtering, *Langmuir* **2006**, *22*.
- [83] I. Berndt, J. S. Pedersen and W. Richtering, *Angew. Chem. Int. Edit.* **2006**, *45*, 1737-1741.
- [84] M. Keerl, J. S. Pedersen and W. Richtering, *J. Am. Chem. Soc.* **2009**, *131*, 3093-3097.
- [85] G. V. Schulz, *Z. Phys. Chem. B-Chem. Elem. Aufbau. Mater.* **1939**, *43*, 25-46.
- [86] D. O. Tinker, *Chem. Phys. Lipids* **1972**, *8*, 230-257.
- [87] S. R. Aragón and R. Pecora, *J. Chem. Phys.* **1976**, *64*, 2395-2404.

- [88] J. Wagner, *J. Appl. Cryst.* **2004**, *37*, 750-756.
- [89] D. S. Thompson, *J. Phys. Chem.* **1971**, *75*, 789-791.
- [90] D. S. Thompson, *J. Chem. Phys.* **1971**, *54*, 1411-1412.
- [91] D. W. Hukins, *X-ray diffraction by disordered and ordered systems*. Pergamon Press: Oxford, **1981**.
- [92] P. Debye, *Phys. Z.* **1927**, *28*, 135-141.
- [93] G. Fournet, *Acta Cryst.* **1951**, *4*, 293-301
- [94] P. W. Zhu and J. W. White, *J. Chem. Phys.* **1996**, *104*, 9169-9173.
- [95] J. A. Venables, *Philos. Mag.* **1973**, *27*, 697-738.
- [96] J. K. Percus and G. J. Yevick, *Phys. Rev.* **1958**, *110*, 1-13.
- [97] L. S. Ornstein and F. Zernike, *Proc. K. Akad. Wetensch. Amsterdam* **1914**, *17*, 793-806.
- [98] R. J. Baxter, *J. Chem. Phys.* **1970**, *52*, 4599-4607.
- [99] D. J. Kinning and E. L. Thomas, *Macromolecules* **1984**, *17*, 1712-1718.
- [100] S. Hansen, *J. Appl. Cryst.* **2011**, *44*, 265-271.
- [101] P. Bartlett and R. H. Ottewill, *J. Chem. Phys.* **1992**, *96*, 3306-3318.
- [102] E. R. Soule and G. E. Elicabe, *Part. Part. Syst. Char.* **2008**, *25*, 84-91.
- [103] A. Y. Terekhov, B. J. Heuser, M. A. Okuniewski, R. S. Averbach, S. Seifert and P. R. Jemian, *J. Appl. Cryst.* **2006**, *39*, 647-651.
- [104] J. Jansson, K. Schillen, M. Nilsson, O. Soderman, G. Fritz, A. Bergmann and O. Glatter, *J. Phys. Chem. B* **2005**, *109*, 7073-7083.
- [105] X. A. Guo and U. Riebel, *J. Chem. Phys.* **2006**, *125*.
- [106] M. Baus and J. L. Colot, *Phys. Rev. A* **1987**, *36*, 3912-3925.
- [107] A. Santos, M. L. Deharo and S. B. Yuste, *J. Chem. Phys.* **1995**, *103*, 4622-4625.
- [108] R. J. Baxter, *J. Chem. Phys.* **1968**, *49*, 2770-2774.
- [109] C. Regnaut and J. C. Ravey, *J. Chem. Phys.* **1989**, *91*, 1211-1221.
- [110] S. V. G. Menon, C. Manohar and K. S. Rao, *J. Chem. Phys.* **1991**, *95*, 9186-9190.
- [111] C. G. Dekruif, P. W. Rouw, W. J. Briels, M. H. G. Duits, A. Vrij and R. P. May, *Langmuir* **1989**, *5*, 422-428.
- [112] M. H. G. Duits, C. G. Dekruif and A. Vrij, *Colloid Polym. Sci.* **1992**, *270*, 154-164.
- [113] Y. H. Wen, P. C. Lin, C. Y. Lee, C. C. Hua and T. C. Lee, *J. Colloid Interf. Sci.* **2010**, *349*, 134-141.

- [114] A. J. Chinchalikar, V. K. Aswal, J. Kohlbrecher and A. G. Wagh, *Chem. Phys. Lett.* **2012**, *542*, 74-80.
- [115] R. Joksimovic, S. Prevost, R. Schweins, M. S. Appavou and M. Gradzielski, *J. Colloid Interf. Sci.* **2013**, *394*, 85-93.
- [116] W. Stöber, A. Fink and E. Bohn, *J. Colloid Interface Sci.* **1968**, *26*, 62-69.
- [117] M. Choi, C. Kim, S. O. Jeon, K. S. Yook, J. Y. Lee and J. Jang, *Chem. Commun.* **2011**, *47*, 7092-7094.
- [118] S. Hansen, *J. Appl. Cryst.* **2013**, *46*, 1008-1016.
- [119] U.W.Arndt, *International tables for crystallography volume C:mathematical, physical and chemical tables*. Kluwer Academic Publishers: Dordrecht, **1992**.
- [120] J. Daillant and A. Gibaud, *X-ray and neutron reflectivity : principle and applications*. Springer: Heidelberg, **1999**.
- [121] G. Renaud, R. Lazzari, C. Revenant, A. Barbier, M. Noblet, O. Ulrich, F. Leroy, J. Jupille, Y. Borensztein, C. R. Henry, J. P. Deville, F. Scheurer, J. Mane-Mane and O. Fruchart, *Science* **2003**, *300*, 1416-1419.
- [122] S. Jin, T. Hirai, B. Ahn, Y. Rho, K. W. Kim, M. Kakimoto, P. Gopalan, T. Hayakawa and M. Ree, *J. Phys. Chem. B* **2010**, *114*, 8033-8042.
- [123] S. K. Sinha, E. B. Sirota, S. Garoff and H. B. Stanley, *Phys. Rev. B* **1988**, *38*, 2297-2311.
- [124] S. Dietrich and A. Haase, *Phys. Rep.* **1995**, *260*, 1-138.
- [125] M. Rauscher, R. Paniago, H. Metzger, Z. Kovats, J. Domke, J. Peisl, H. D. Pfannes, J. Schulze and I. Eisele, *J. Appl. Phys.* **1999**, *86*, 6763-6769.
- [126] B. Lee, I. Park, J. Yoon, S. Park, J. Kim, K. W. Kim, T. Chang and M. Ree, *Macromolecules* **2005**, *38*, 4311-4323.
- [127] P. Muller-Buschbaum, *Anal. Bioanal. Chem.* **2003**, *376*, 3-10.
- [128] S. Hansen and J. S. Pedersen, *J. Appl. Cryst.* **1991**, *24*, 541-548.
- [129] J. S. Pedersen, *J. Phys. IV* **1993**, *3*, 491-498.
- [130] J. S. Pedersen, D. Posselt and K. Mortensen, *J. Appl. Cryst.* **1990**, *23*, 321-333.
- [131] R. K. Heenan Q resolution on LOQ at ISIS (revised 28/3/02). <http://www.isis.stfc.ac.uk/instruments/loq/documents/information-about-the-loq-resolution-function7465.pdf>.

- [132] R. Valiullin, S. Naumov, P. Galvosas, J. Karger, H. J. Woo, F. Porcheron and P. A. Monson, *Nature* **2006**, *443*, 965-968.
- [133] B. J. C. and J. H. De Boer, *J. Catal.* **1968**, *10*, 153-165.
- [134] M. Thommes, B. Smarsly, M. Groenewolt, P. I. Ravikovitch and A. V. Neimark, *Langmuir* **2006**, *22*, 756-764.
- [135] P. I. Ravikovitch and A. V. Neimark, *Langmuir* **2002**, *18*, 9830-9837.
- [136] E. P. Barrett, L. G. Joyner and P. P. Halenda, *J. Am. Chem. Soc.* **1951**, *73*, 373-380.
- [137] J. Villarroel Rocha, D. Barrera and K. Sapag, *Top. Catal.* **2011**, *54*, 121-134.
- [138] S. Brunauer, P. H. Emmett and E. Teller, *J. Am. Chem. Soc.* **1938**, *60*, 309-319.
- [139] J. H. Deboer, B. C. Lippens, B. G. Linsen, Broekhof. J. C, Vandenne. A and T. J. Osinga, *J. Colloid Interf. Sci.* **1966**, *21*, 405-414.
- [140] P. Voogd, J. J. F. Scholten and H. van Bekkum, *Colloid. Surface* **1991**, *55*, 163-171.
- [141] B. Tokay, O. Karvan and A. Erdem-Senatalar, *Micropor. Mesopor. Mat.* **2010**, *131*, 230-237.
- [142] W. D. Harkins and G. Jura, *J. Am. Chem. Soc.* **1944**, *66*, 1366-1373.
- [143] P. I. Ravikovitch and A. V. Neimark, *Langmuir* **2002**, *18*, 1550-1560.
- [144] K. S. W. Sing, D. H. Everett, R. A. W. Haul, L. Moscou, R. A. Pierotti, J. Rouquérol and T. Siemieniewska, *Pure Appl. Chem.* **1985**, *57*, 603-619.
- [145] B. Chu, *Laser Light Scattering: Basic Principles and Practice*. Academic Press: Boston, **1991**.
- [146] D. P. Wang and H. C. Zeng, *Chem. Mater.* **2011**, *23*, 4886-4899.
- [147] K. Cheng and S. H. Sun, *Nano Today* **2010**, *5*, 183-196.
- [148] X. W. Lou, L. A. Archer and Z. C. Yang, *Adv. Mater.* **2008**, *20*, 3987-4019.
- [149] W. K. Oh, H. Yoon and J. Jang, *Biomaterials* **2010**, *31*, 1342-1348.
- [150] W.-K. Oh, S. Kim, M. Choi, C. Kim, Y. S. Jeong, B.-R. Cho, J.-S. Hahn and J. Jang, *ACS NANO* **2010**, *4*, 5301-5313.
- [151] Z. Yan, G. T. Li, L. Mu and S. Y. Tao, *J. Mater. Chem.* **2006**, *16*, 1717-1725.
- [152] B. Yu, D. A. Wang, Q. Ye, F. Zhou and W. M. Liu, *Chem. Commun.* **2009**, *44*, 6789-6791.
- [153] Z. H. Xu, P. A. Ma, C. X. Li, Z. Y. Hou, X. F. Zhai, S. S. Huang and J. Lin, *Biomaterials* **2011**, *32*, 4161-4173.
- [154] C. Kim, S. Kim, W.-K. Oh, M. Choi and J. Jang, *Chem. Eur. J.* **2012**, *18*, 4902-4908.

- [155] S. Parambadath, V. K. Rana, D. Y. Zhao and C. S. Ha, *Micropor. Mesopor. Mat.* **2011**, *141*, 94-101.
- [156] S. Pabisch, B. Feichtenschlager, G. Kickelbick and H. Peterlik, *Chem. Phys. Lett.* **2012**, *521*, 91-97.
- [157] H. Borchert, E. V. Shevehenko, A. Robert, I. Mekis, A. Kornowski, G. Grubel and H. Weller, *Langmuir* **2005**, *21*, 1931-1936.
- [158] S. Pikus, E. B. Celer, M. Jaroniec, L. A. Solovyov and M. Kozak, *Appl. Surf. Sci.* **2010**, *256*, 5311-5315.
- [159] S. Mascotto, D. Wallacher, A. Brandt, T. Hauss, M. Thommes, G. A. Zickler, S. S. Funari, A. Timmann and B. M. Smarsly, *Langmuir* **2009**, *25*, 12670-12681.
- [160] S. Jähnert, D. Müter, J. Prass, G. A. Zickler, O. Paris and G. H. Findenegg, *J. Phys. Chem. C* **2009**, *113*, 15201-15210.
- [161] A. Guinier, *X-Ray Diffraction in Crystals, Imperfect Crystals and Amorphous Bodies*. Dover: New York, **1963**.
- [162] *J. Phys.: Conf. Ser.* **2010**, 247.
- [163] I. Berndt, J. S. Pedersen, P. Lindner and W. Richtering, *Langmuir* **2006**, *22*, 459-468.
- [164] O. Glatter and O. Kratky, *Small Angle X-Ray Scattering*. Academic Press: London, **1982**.
- [165] S. Förster, A. Timmann, M. Konrad, C. Schellbach, A. Meyer, S. S. Funari, P. Mulvaney and R. Knott, *J. Phys. Chem. B* **2005**, *109*, 1347-1360.
- [166] A. Vrij, *J. Chem. Phys.* **1979**, *71*, 3267-3270.
- [167] H. Blas, M. Save, P. Pasetto, C. Boissiere, C. Sanchez and B. Charleux, *Langmuir* **2008**, *24*, 13132-13137.
- [168] W. Song, R. E. Justice, C. A. Jones, V. H. Grassian and S. C. Larsen, *Langmuir* **2004**, *20*, 4696-4702.
- [169] V. R. Patel and M. M. Amiji, *Pharm. Res.* **1996**, *13*, 588-593.
- [170] W. S. W. Shalaby, G. E. Peck and K. Park, *J. Control. Release* **1991**, *16*, 355-364.
- [171] P. M. de la Torre, Y. Enobakhare, G. Torrado and S. Torrado, *Biomaterials* **2003**, *24*, 1499-1506.
- [172] L. Arleth and J. S. Pedersen, *Phys. Rev. E* **2001**, *63*.
- [173] G. R. Deen, C. L. P. Oliveira and J. S. Pedersen, *J. Phys. Chem. B* **2009**, *113*, 7138-7146.

- [174] F. M. Hamzeh and R. H. Bragg, *J. Appl. Phys.* **1974**, *45*, 3189-3195.
- [175] S. S. Berr, *J. Phys. Chem.* **1987**, *91*, 4760-4765.
- [176] R. J. Baxter, *Aust. J. Phys.* **1968**, *21*, 563-571.
- [177] E. Leutheusser, *J. Chem. Phys.* **1986**, *84*, 1050-1051.
- [178] M. S. Ripoll and C. F. Tejero, *Mol. Phys.* **1995**, *85*, 423-428.
- [179] P. W. Atkins, *Physical Chemistry*. Oxford University Press: Oxford, **1998**.
- [180] Y. Ma, X. Cao, X. Feng, Y. Ma and H. Zou, *Polymer* **2007**, *48*, 7455-7460.
- [181] B. Jańczuk, T. Białopiotrowicz and A. Zdziennicka, *J. Colloid Interf. Sci.* **1999**, *211*, 96-103.
- [182] K. Gotoh and S. Kikuchi, *Colloid Polym. Sci.* **2005**, *283*, 1356-1360.